EFFECT OF CARBON CONTENT IN CARBON STEELS ON FORMATION OF WELDING RESIDUAL STRESS

by

Fatih UZUN

Submitted to the Institute of Graduate Studies in
Science and Engineering in partial fulfillment of
the requirements for the degree of
Doctor of Philosophy
in
Chemical Engineering

Yeditepe University
2014

EFFECT OF CARBON CONTENT IN CARBON STEELS ON FORMATION OF WELDING RESIDUAL STRESS

APPROVED BY:

Assoc. Prof. Dr. Seyda Malta ...SEYDA...

Prof. Dr. Ali Nezihi Bilge ....

Prof. Dr. Mustafa Özilgen ....

Prof. Dr. Süheyla Uzman ....

Assist. Prof. Dr. Ali Fethi Okyar ....

DATE OF APPROVAL: 24 / 02 / 2014

ACKNOWLEDGEMENTS

Studying for a PhD degree is a mountainous task. Compulsory and elective courses, performing experiments, writing codes for computer simulations, and combining all these in a thesis occupies most of PhD student's time. During this period studying for PhD become easier by the help of my jury members, family and friends.

My studies for a PhD degree started under the guidance of Prof. Dr. Ali Nezihi Bilge. After he leaved from Yeditepe University, we continued to study on my PhD thesis as he is my supervisor. I would like to express my gratitude to Prof. Bilge for all of his wisdom, support, encouragement and expert advice during this period.

Experimental and numerical studies of my PhD thesis is performed through strong support of Assoc. Prof. Dr. Seyda Malta. I owe my deepest gratitude to my supervisor for the vision, encouragement, and advice provided necessary for me to proceed my PhD thesis.

The jury members and advisors Prof. Dr. Mustafa Özilgen and Prof. Dr. Süheyla Uzman are acknowledged for their smart ideas and technical support. Assist. Prof. Dr. Ali Fethi Okyar provided equipment owned by Mechanical Engineering Department of Yeditepe University for my metallography studies. I want to thank for his support.

Special thanks to my family members and friends for their support and patience during my study.

ABSTRACT

EFFECT OF CARBON CONTENT IN CARBON STEELS ON FORMATION OF WELDING RESIDUAL STRESS

Welding is a joining process that uses high amount of heat input. Thermal strains are formed around the weld beam during this process which is followed rapid cooling and remaining residual stresses. In this study, effect of carbon content of formation of welding residual stress is investigated within low alloy carbon steels. Residual stress within steel samples with different carbon content is measured using ultrasonic sound waves. Finite element method is used to perform three dimensional simulation of welding process of steel samples with different carbon content. Experimental and numerical results of residual stress distributions are investigated in terms of carbon content.

ÖZET

KAYNAK İŞLEMİ SONUCU KARBON ÇELİKLERDE KARBON ORANININ ARTIK GERİLME OLUŞUMUNA ETKİSİ

Kaynak işlemi yüksek ısı girdisiyle gerçekleştirilen birleştirme yöntemidir. Kaynak işlemi sonuncu malzemelerde yüksek ısı girdisi ve ani soğuma neticesinde bazı deformasyonlar olur ve malzemenin özellikle kaynak çevresinde artık gerilmeler oluşur. Bu çalışmada kaynak işlemi sonrası artık gerilme oluşumunun malzeme kompozisyonu tarafından nasıl etkilendiği incelenmiştir. Farklı karbon yoğunluğundaki çeliklerde oluşan artık gerilmeler ultrasonik ses dalgaları kullanılarak ölçülmüştür. Sonlu elemanlar yöntemi kullanılarak üç boyutlu stres simülasyonu gerçekleştirilmiştir. Deneysel sonuçlar ve sonlu elemanlar yönteminin verdiği sonuçların birbirleriyle uyumu karbon yoğunluğuna bağlı olarak incelenmiştir.

TABLE OF CONTENTS

LIST OF FIGURES

LIST OF TABLES

LIST OF SYMBOLS / ABBREVIATIONS

A1	lower critical temperature line
A3	upper critical temperature line
A	cross sectional area of the medium,
c	the harmonic contribution
C_p	the specific heat
d	the first inharmonic contribution
E	Young's modulus
F	the force of attraction
F_0	preliminary test force for *HBR* testing
$f_{x,y,z}$	the body forces acting in principal directions
G	shear modulus
I	current
I_1, I_2, I_3	stress invariants
k	the wave vector
k	the thermal conductivity
L	acoustoelastic constant
l, m, n	Murnaghan's third-order elastic constant
M	the linear modulus
M'	a nonlinear modulus
Q	the weld heat input
q	the charge on each ion
q'	the heat generation per unit volume
q''	the rate of themal energy emitted by the surface
q_x, q_y, q_y	x, y, and z are the components of heat transfer rate
r_0	the equilibrium atomic bond length
S	scale division for *HBR* testing
T	temperature
t	the time
U	energy

U_a	the attractive energy
U_r	the repulsive energy
u	the displacement
	displacements in the 1, 2, 3 directions respectively
V	the voltage
V	ultrasonic wave velocity
V_o	ultrasonic wave velocity in stress free medium
V_{11}, V_{12}, V_{13}	speed of waves propagating in the 1 direction with particle

α	thermal expansion coefficient
$\alpha_1, \alpha_2, \alpha_3$	components of the homogeneous triaxial principal strains in the 1,2,3 directions
γ	the shear strain
δ	the Stefan-Boltzman constant
ε_0	the permittivity of vacuum
ε^{th}	the thermal strain
ϵ	the emissivity of the surface
η	the weld efficiency
θ	$\alpha_1 + \ \alpha_2 + \alpha_3$
ρ	the density
ρ_0	the strain free density
σ	stress
v	Poisson’s ratio
τ	the shear stress
r	the separation of ions
ω	the angular frequency
λ, μ	Lame or second-order elastic constant

FEM	Finite Element Method
SAW	Submerged arc welding

1. INTRODUCTION

Residual stresses are stresses that remain after removal of the source of stress which affect the mechanical properties of a material. Manufacturing and operation processes introduce residual stress. Small increments in residual stress have a potential to cause failures without extreme loading conditions. Welding is a reason of residual stresses formed during the manufacturing processes. Aerospace, automotive and nuclear industries use welding for joining processes and takes welding residual stress into account.

Studies on residual stress often focus on analysis of residual stress distribution. Welding residual stress analysis was investigated by various authors. Different welding conditions were discussed using experimental, analytical and numerical methods. These studies dealt with welding type and welding conditions. However, material composition can have effect on formation of welding process as well, which has not been well investigated thus far.

Many elements are composed to form alloys which are then used as different types of engineering materials. These materials are designed according to the desired application as suggested by engineering problems. Composition of elements affects properties of these materials. Strength determines the stress limits that can be accomplished which is related to the composition of the materials.

Main element of steels is carbon which is related to the strength of the material. Depending on the carbon content and strength, low alloy steels have different behavior under stress. One of the main sources of stress is heat which affects steel materials during welding process. Stress formation during welding is expected to be effected by the carbon content of the materials and remaining stresses after the end of welding process is also affected by the carbon content of steels. Accordingly, it is necessary to investigate effect of carbon content on formation of residual stress. In this study, low alloy carbon steels of three different compositions are used to investigate this effect. Ultrasonic wave velocity measurements are carried out along with hardness and grain formation experiments. The residual stresses obtained from ultrasonic wave velocity measurements are then compared with numerical analyses performed using finite element method.

2. LITERATURE SURVEY

Stresses are formed during the fabrication and operation of solid materials. After the removal of the cause of stress some stress remains. The remaining stress in the solid material is called residual stress. Residual stresses affect the properties of a material. Brittle fractures, fatigue, or stress corrosion cracking may be expanded due to high amount of residual stress. Consequently, residual stress must be reduced and minimized. Remarkable destructive methods are available to reduce residual stress, such as heat treatment, preheating, vibration stress relieving, and weld sequencing. Several studies were focused on investigation of effect of heat treatment techniques on material properties, but these are mostly destructive methods.

Welding of steel butt joints has a wide range of applications in the fabrication of industrial products, including ships, offshore structures, steel bridges, aircrafts, and pressure vessels. There are many advantages of welded structures such as a high joint efficiency, water and air tightness and low fabrication cost. However, among the advantages of this joining method, residual stress can be formed as a consequence of heating followed by rapid cooling during the welding process.

Over the last few decades, various residual stress measurement techniques have been developed in order to observe effects of residual stress. In general, these techniques are classified as destructive and non-destructive techniques. Destructive methods measure by destroying the state of equilibrium of the residual stress and measure only the consequences of stress relaxation occurred by destruction. Most common destructive techniques are hole-drilling method, ring core technique, bending deflection method, and sectioning method. These methods are widely used in industry and they are sensitive to the macroscopic residual stress. Non-destructive methods are developed on the basis of the relationship between residual stress and the physical or crystallographic parameters. Different non-destructive techniques are developed such as the X-ray diffraction method, neutron diffraction method, ultrasonic method, and magnetic method. Experimental investigation of residual stress requires stress free materials which can be accomplished by a specific heat treatment technique, annealing.

Numerical analysis of residual stress allows cost effective and reliable studies. Improving computer technologies allow fast and accurate simulations. Most widely used numerical analysis method is finite element. This technique allows developing numerical models that mimic welding process. Many studies were performed for different type of welding processes. These studies mostly verified with destructive and non-destructive experiments.

Chemical composition of materials affects properties of materials. Iron is the main component of steels. Various types of steels are being produced with different chemical compositions. Addition of another element can increase durability of the steel. On the other hand, this element can affect strength of the product. Residual stresses are formed during production and operation of materials. This can also be affected by chemical composition of materials. Although how material properties change with chemical composition has been thoroughly investigated, its effect on the formation of residual stress is unexplored.

2.1. ANNEALING AND METALLOGRAPHY

Welding residual stress investigation requires stress free samples. Residual stresses in materials due to manufacturing process should be removed. Many heat treatment methods are applied to steel in order to obtain final products with desired material properties. Heat treatment is the application of heating and cooling sequences to materials. These sequences vary according to the requirements of heat treatment process. Annealing is one of the heat treatment types applied in order to relieve stress. During the heating period phase transformations occur, while structural changes occur in the cooling stage. These effects can vary depending on the carbon content and the other alloying elements of the steel.

Full annealing should be accomplished with precise temperature and time parameter in order to obtain stress free materials without damaging it. Full annealing temperature for steel is defined as austenizing temperature which is just above the phase boundary between austenitic and ferritic phases. Below this temperature complete transformation to austenitic phase does not occur. On the other hand, over that temperature material properties such as strength and hardness abruptly decrease. Therefore it is critical to determine the correct annealing temperature. This temperature is often determined by observing the hardness and grain size of the materials. Observing grain size and hardness of steels allow determination of correct temperature to perform full annealing process without losing the aforementioned material properties.

2.1.1. Annealing and Material Properties

Annealing process effects grain size, ductility, hardness and strength of materials. Several researches have been conducted to investigate behavior of material under different annealing conditions. In these studies, relation between annealing temperature and hardness of the materials were observed. Wang investigated annealing softening behavior of cold-rolled low-carbon steel with a dual-phase structure and the resulting tensile properties [1]. Annealing behavior and mechanical properties of severely deformed interstitial free steel was studied by Hazra [2]. Annealing behavior of martensitic steels was investigated by Kimura [3]. Mateo investigated the effect of annealing temperature on the mechanical properties, formability and corrosion resistance of hot-rolled duplex stainless steel [4]. Lee studied the effect of temperature on hardness improvement in a vanadium carbide (VC)/steel surface-alloyed material fabricated by high-energy electron-beam irradiation [5]. Khodabakhshi investigated the annealing responses after constrained groove pressing of low carbon steel sheets [6]. Irani studied the effect of forging temperature on homogeneity of microstructure and hardness of precision forged gears of low carbon steel [7]. Dual phase steels were tempered within different temperatures. Effect of this process on the microstructure and mechanical properties were investigated by Sayed and Kheirandish [8]. Effect of annealing temperature on properties of H_2/N_2 rf plasma-treated stainless steel was investigated by Negm [9]. Y. Liu studied the formation of oxides particles in the ferritic steel by using gas-atomized powder [10]. Hardness variations as a result of tempering were investigated in VC/steel composite fabricated by high-energy electron beam irradiation by Lee [11]. Lee investigated the effects of recrystallization annealing temperature on carbide precipitation microstructure, and mechanical properties in Fe-18Mn-0.6C-1.5Al twinning induced plasticity (TWIP) steel [12]. The influence of reversion annealing behavior on the formation of nano grained structure in AISI 201L austenitic stainless steel through martensite treatment was studied by Rezaee [13]. Huang investigated the behavior of electroplated hard-chromium on Cr-Mo steel subjected to long term annealing at 250 ^{o}C [63]. El-Hossary investigated the effect of annealing temperature on hardness, thickness and phase structure of carbonitrided stainless steel [14]. Effect of annealing temperature on microstructure, phase composition and mechanical properties of thixo-cast 100Cr6 steel was studied by Rogal and Dutkiewicz [15]. Microstructure and mechanical properties of low nickel maraging steel was studied by Sha [16]. Hosseini investigated the production of the nano/ultrafine grained low carbon steel by martensite process using plane strain compression [17]. High temperature properties and mechanical stability of hot work tool steels were analyzed by Medvedeva [18]. Liu investigated the decrease in hardness during isothermal process at 700 ^{o}C for Fe-24Mn-0.7Si-1.0Al TWIP steel [19]. Forouzan investigated production of nano/submicron grained AISI 304L stainless steel through the martensite reversion process [20]. Chowdhury studied the randomization of texture during recrystallization of austenite in a cold rolled metastable austenitic stainless steel [21]. In all these studies heat treatment performed within different conditions for various purposes. Common part of these studies are measurement of hardness after each heat treatment process. Consequently, hardness test is used to follow annealing stages in this thesis.

2.1.2. Welding and Material Properties

Welding is a joining process that requires high amount of heat. As it is in the heat treatment processes hardness and grain size of materials are shown to be affected by high amounts of heat input. Many authors investigated effect of welding process on hardness of materials. Valesaco studied the effect of welding on local mechanical properties of stainless steels for concrete structures using universal hardness test [22]. Structure and hardness changes in welded joints of Hardox steels were investigated by Frydman [23]. Ziemian studied the effects of flashing and upset sequences on microstructure, hardness, and tensile properties of welded structural steel joints. ASTM-A529 carbon manganese steel was welded by flash butt welding [24]. Ultrafine grained plain low carbon steel formed by the martensite process was welded by friction stir welding technique and hardness was measured [25]. Güral studied heat treatment in two phase region and its effect on microstructure and mechanical strength after welding of low carbon steel [26]. Welding of 1010 steel was performed under controlled argon atmosphere. Acarer and Demir investigated mechanical and metallurgical properties of explosive welded aluminum-dual phase steel [27]. Incorporation of preheating and post heating effect on the mechanical properties of laser welding joints were investigated at mild steel and stainless steel by Abdullah and Siddiqui [28]. Klobcar investigated the aging of maraging steel welds during aluminum alloy die casting [29]. Multi track laser surface melting roller steel is a thermal process. Ratio of overlapping during this process on hardness was studied by Li [30]. Results of these studies shows that hardness decreases around the weld beam and a slight increase in hardness when compared to heat effected zone, occurs in the weld beam.

2.1.3. Ultrasonic Waves and Metallography

Steels are composed of many grains that accommodate crystal structure of the material with different alignment. Heat treatment of steels affects their grain size. Rapid cooling results in small grain sizes while slow cooling rates cause formation of large grains. In order to determine stages of annealing process, determination of grain size has vital importance. Grain size of steels can be determined using a microscope after grinding, polishing and etching processes.

Grain size has an important effect on ultrasonic wave velocity. In order to determine the relationship of ultrasonic waves with residual stresses, it is necessary to eliminate the effect of grain sizes on ultrasonic waves. Different authors studied the effect of grain size on ultrasonic waves. These studies focused on measurement of grain size using a nondestructive method.

Palanichamy presented an ultrasonic velocity measurement method to estimate the grain size in austenitic stainless steel [31]. Sarpun proposed a method for the determination of mean grain size by ultrasonic methods [32]. Hutchinson applied laser ultrasonics to investigate recrystallization and grain growth in metals [33]. Mutlu investigated the effect of grain size on the ultrasonic parameters in stainless steels [34]. Brosey used ultrasonic technique to measure grain size in uranium without metallographic preparation or destructive analysis [35]. Bouda studied the influence of grain size on ultrasonic velocities and attenuation. Ultrasonic parameters were evaluated as a function of grain size [36]. In these studies authors used ultrasonic sound waves as an alternative to exhaustive metallographic procedures for grain size investigation. However, this technique does not visualize grain distribution whether it is fine or not. It can only bring an average value for grain sizes. Accordingly, for detailed investigation of grain distribution, it is required to perform metallographic techniques. Figure 1.1 shows an example grain size distribution data obtained using longitudinal and transversal waves [36].

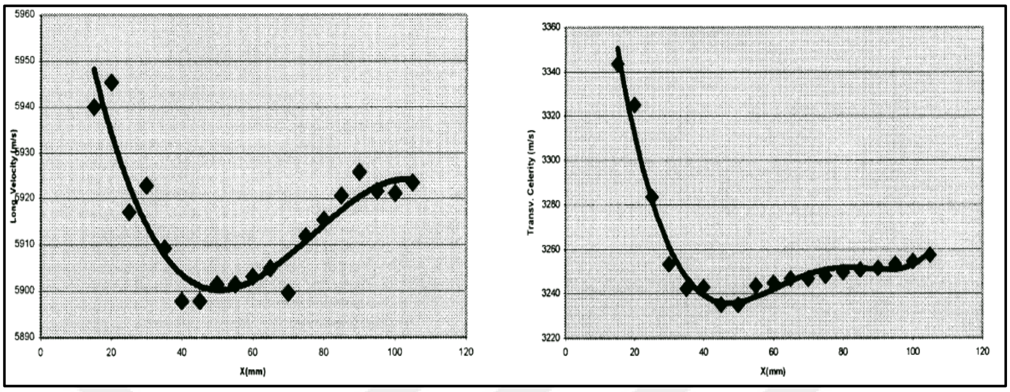

Figure 1.1. Longitudinal and transversal wave velocities along the x axis [36]

2.2. EXPERIMENTAL ANALYSIS OF RESIDUAL STRESS

Residual stress analysis through the thickness of a material are performed using destructive and nondestructive techniques. Hole-drilling is a destructive way of measuring residual stress whereas neutron diffraction is a nondestructive method. Both methods allow the measurement of residual stress in different thickness layers of the material. Another method for measurement of residual stress is ultrasonic technique. However, ultrasonic method is not able to determine residual stresses at different depth layers. This technique allows bulk measurement of residual stress through the thickness.

Neutron diffraction and hole drilling methods are widely used for determination of residual stress. Ability of neutrons that can penetrate many millimeters to centimeters in most of the engineering materials is used in these studies. This property of neutrons allowed measurement of residual stresses through the thickness of the material. Researchers performed many studies on different type of materials under various source of stress. Welding is the most common source of residual stress because of its vital effects on materials. Neutron diffraction technique is used to determine residual stresses through the thickness of welded materials in various studies. Reynolds investigated tensile properties, optical microstructure, and residual stress state of 304L stainless steel friction welds [37]. Dakhalaoui and his colleagues studied the influence of chemical composition and residual stresses on elastoplastic mechanical properties of duplex stainless steels [38]. The depth profile of residual stress was analyzed by neutron diffraction technique comparing inoxidizable martensitic steel samples with and without tungsten carbide coating [39]. Carrado and Palkowski analyzed bulk residual stress in biomedical systems using neutron diffraction technique [40]. Üstündağ studied the determination of residual stresses in a bulk metallic glass-stainless steel composite material [41]. An application of neutron diffraction technique for residual stress measurement on welded specimens was performed by Jang [42]. Wimpory performed statistical analysis of residual stress determinations using neutron diffraction [43]. Through the thickness characterization of the residual strain in iterative laser forming was performed by Moore [44]. Turski measured residual stress in a 316L stainless steel bead on plate weld specimen [45]. Larson measured and modeled residual stress in a welded Haynes 25 cylinder [46]. Edwards measured the residual stresses near a boat shaped repair in a 20 mm thick stainless steel tube butt weld [47]. Neutron diffraction measurement of residual stress in an electron beam welded uranium cylinder was performed by Brown [48]. An measured through thickness distribution of residual stress in two extreme heat input thick weld using neutron diffraction [49]. Figure 1.2 illustrates ability of neutron diffraction technique to measure through thickness residual stress distribution. Effect of stop start features on residual stresses in a multi-pass austenitic stainless steel weld was investigated by Turski [50]. Doyle evaluated through thickness residual stress in martensitic stainless steel as a function of gas quenching pressure using thermal neutrons [51]. Bendeich measured through thickness residual stress in laser clad repaired low pressure turbine blades for the power industry using neutron diffraction [52]. Neutron diffraction technique is capable of obtain data about all principal stresses in a material. However, this technique is too expensive and requires immovable equipment.

In addition to neutron diffraction, hole drilling technique is capable of measuring residual stress within different sections of the material. Truman [53] and Frantini [54] used hole drilling method to predict welding residual stress through the thickness of the materials. However, this technique damages the material and can only be used for research purposes. Materials under operation cannot be tested using hole drilling method.

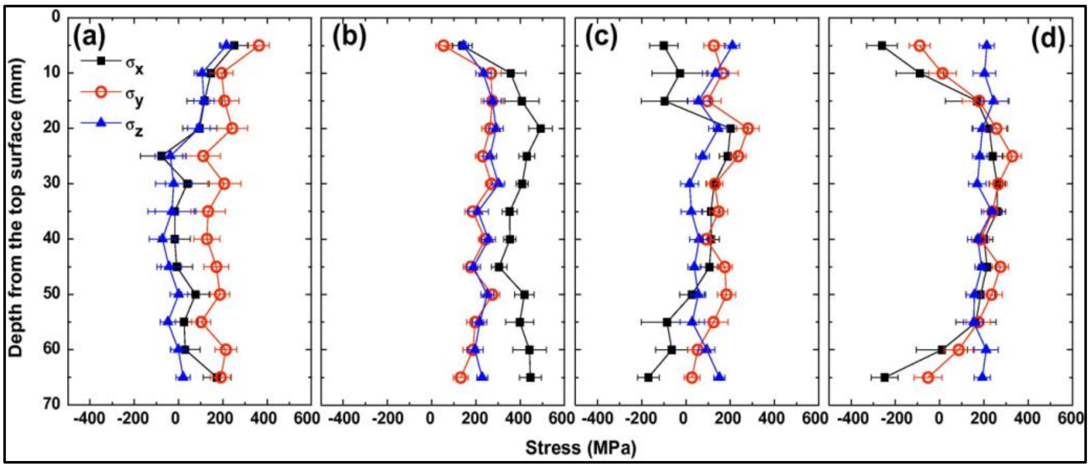

Figure 1.2. Residual stresses through the thickness of the HHI specimen using neutron diffraction along a. 0, b. 30, c. 60 and d. 100 mm locations from the centerline [49]

Influence of stress on elastic wave propagation gained attention for many decades. The influence of initial stress on elastic waves was studied by Biot in 1940 [55]. In this study it was shown that a uniform hydrostatic pressure does not change the laws of propagation. He stated that propagation and reflections of elastic waves in a material under initial stress must follow laws which cannot be explained by elastic anisotropy or a change in elastic constants. It was stated that a discontinuity in a material can cause a reflection. In a novel study proposed by Hughes and Kelly in 1953 [56], second order elastic deformation of solids was investigated. The velocities of elastic waves which are longitudinal and shear waves were measured as a function of applied stress. Effective elastic coefficients for wave propagation in crystals under stress were defined by Thurston in 1964 [57]. In addition to stress, the effect of deformation resulting from the stress and the thermodynamic elastic coefficients were also analyzed. Acoustoelastic and third order elastic constants for rail steel were measured by Eagle and Bray in 1976 [58]. Theory of Hughes and Kelly was used to calculate the third order elastic constants from the acoustoelastic data. Fukuako investigated the acoustoelastic effect of Rayleigh surface wave in homogeneous isotropic material [59]. Experimental study was performed on the mild steel samples. Linear relation between the stress variation and velocity was observed. A perturbation theory for the acoustoelastic effect of surface waves was developed by Husson in 1984 [60]. The author used the calculation of acoustoelastic effect proposed by Fukuoka et. al. [59] to the case of Rayleigh waves and Lamb waves propagating in isotropic media. Angular dependence of ultrasonic wave propagation in a stresses, orthorhombic continuum was investigated in 1986. Thompson and colleagues proposed a theory for the case of a biaxial stresses orthorhombic continuum [61]. The use of acoustoelastic theory for measurement of residual stress was studied by Man and Lu in 1986 [62]. They proposed a new approach for evaluation of stress without need of calibration specimens.

Residual stress measurements were performed using acoustoelastic effect by various authors. During the welding process modifications occur in the microstructure of heat affected zone and melted zone. These modifications induce variations of the velocity of the acoustic waves. Longitudinal, shear, Rayleigh, lamb and love waves were used in many studies to measure residual stress. Ultrasonic methods allow measurement of bulk residual stress through the propagation distance of the wave. Longitudinal and shear waves were used to measure bulk residual stresses through the thickness of the materials. Surface residual stresses were measured using surface waves.

Surface stresses are investigated using Rayleigh waves by many authors. In the pioneering study, Lu et al. used laser ultrasonic to measure acoutoelastic effect of Rayleigh surface waves to study the acoustoelastic behavior of T16061-T6 aluminum alloy [63]. A method to measure variations of ultrasonic Rayleigh wave velocity related to the stress state was presented by Akhshik and Moharrami [64]. Experimental study on the surface stress measurement of 235 steel with Rayleigh wave detection technique was performed by He [65]. Todaro and Capsimalis investigated acoustoelastic effect for Rayleigh surface waves in the presence of a non-uniform stress field [66] for a right circular steel cylinder was investigated. Surface acoustic waves were used to perform ultrasonic measurement of residual deformation stress in thin metal plates by Salama [67]. Residual stress measurements were performed as a function of depth in laminated aluminum alloy sheets by Rayleigh waves [68]. Near surface residual stresses were measured using nonlinear Rayleigh surface waves in shot peened aluminum plates by Jacobs [69]. Duquennoy applied Rayleigh waves to steel rods in order to characterize residual stresses using a laser line source and piezoelectric transducers were used [70]. Stresses in orthotropic materials were evaluated using ultrasonic Rayleigh waves by Duquennoy [71]. Namkung performed residual stress characterization with a magnetic/ultrasonic technique [72].

Critically refracted ultrasonic (*Lcr*) wave was used to perform stress analysis in different studies. Li [73] used this system to measure residual stress. Illustration of *Lcr* system used in that study is given in Figure 1.3. *Lcr* technique was used by various author. Qozam performed ultrasonic stress measurement in welded component by using *Lcr* waves [74]. *Lcr* ultrasonic technique was applied for evaluation of post weld heat treatment in steel plates by Junghans [75]. Through thickness stress evaluation of welded stainless steel pipe was performed by Javadi [76]. Bray performed subsurface stress evaluation in steel plates and bars using the *Lcr* ultrasonic wave [77]. Nondestructive evaluation of welding residual stresses in dissimilar welded pipes was performed by Javadi [78]. Akhlaghi used finite element and ultrasonic method to evaluate welding longitudinal residual stress through the thickness in austenitic stainless steel plates [79]. *Lcr* ultrasonic wave was used with X-ray and hole drilling techniques to investigate potentialities of ultrasonic for evaluating residual stresses with the influence of microstructure by Walaszek [80]. Javadi compared contact and immersion ultrasonic method to evaluate welding residual stress of dissimilar joints [81]. Effect of microstructure on the *Lcr* elastic wave for welding residual stress measurement was investigated by Chaki [82]. Nondestructive monitoring of stress relaxation in welded steel plates was performed by Bray [83].

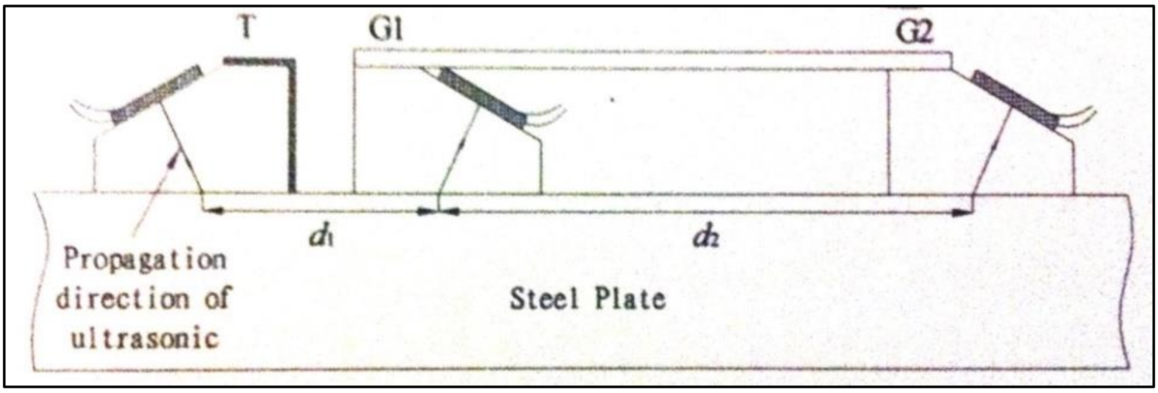

Figure 1.3. Transmitting and receiving set [73]

Shear waves are another type of ultrasonic sound waves which cause particle motion in the direction perpendicular to wave propagation. Many studies performed with shear waves in order to determine residual stress. E. Schneider described a method to determine residual stress by time of flight measurements with linear polarized shear waves [84]. Blessing performed ultrasonic shear wave measurements of known residual stress in aluminum [85].

Yaagishi investigated residual stress behavior of rolled aluminum alloy in a thin plate during cyclic tension fatigue studied using ultrasonic horizontally polarized shear waves [86]. Residual stress in aluminum using electromagnetic acoustic transducers was determined by Clark and Moulder [87]. Hoop residual stresses were determined by measuring ultrasonic wave velocity measurements in the study of Scholz [88].

Many other studies performed using different wave types for measurement of stress and residual stress. Fukuoka performed acoustoelastic stress analysis of residual stress in a patch welded disk [89]. Murayam and Misumi developed a non-contact stress measurement system during tensile testing using the electromagnetic acoustic transducer for a lamb wave [90]. An Ultrasonic Computerized Complex was developed for measurement of residual and applied stress by Kudryavtsev and Kleiman [91]. Aluminum ring plug reference specimens were used in ultrasonic, neutron and strain gauge tests for the determination of residual stress [92]. Results of three different test were good agreement with each other. Gachi performed ultrasonic residual stress measurement in AA7075-T6 friction stir welded plate [93]. Jacquot and his colleagues applied ultrasonic testing to residual stress analysis on heavy plates [94]. Chaki used guided ultrasonic waves for non-destructive monitoring of the stress levels in pre-stressed steel strands [95]. Ultrasound was applied as a tool for studying contact stresses in railway engineering component contacts by Marshall and Lewis [96].

Longitudinal wave travel and propagate in the same direction. This type of waves are mostly used for through the thickness average measurement of residual stress. Scott determined residual stress in extruded billets by using longitudinal acoustic waves [97]. Sanderson used laser generated ultrasound to measure residual stress [98]. Variations in the ultrasound velocity were related to the residual stress state. Doxbeck used laser generated creeping longitudinal waves to determine residual stresses [99].

According to Vangi acoustoelastic effect and its applications are not widely used because of low acoustoelastic response and consequent high sensitivity to errors in measurement, high sensitivity to thermal variations, and nonhomogeneous texture of the materials [100]. Author proposed a method that resolved the problems inherent in the acoustoelastic method to determine stress level in the materials. Longitudinal ultrasonic waves perpendicular to the directions of the stresses were used. Average stresses through the propagation path of the wave were determined. Measurement of ultrasonic wave velocity requires accurate thickness values. Immersion technique was used to propagate ultrasonic waves. This allowed them to propose a new method for determination of ultrasonic wave velocity without information on the thickness of the material.

Salama investigated the possibility of determination of residual stress using the temperature dependence of ultrasonic velocity [101]. Experiments were performed on 6061-T6 aluminum. Stress was applied both in parallel and perpendicular directions to wave propagation. It was calculated that the change in the temperature dependence with applied stress is inversely proportional to the dependence of velocity on stress regardless of the relative direction of stress with respect to wave propagation.

Laser excited ultrasonic transients were used by Karabutov to diagnose residual stress distribution in welded stainless steel samples [102]. They used the advantage of ultrasonic method that allows residual stress measurement of thick materials. The nonlinear theory of acoustoelasticity is used. The sum of longitudinal and transversal stresses was measured by velocity of longitudinal ultrasonic wave. Time of flight measurements were performed both for un-welded and welded samples. Results of the laser ultrasonic method were found to be in good agreement with conventional testing.

2.3. NUMERICAL ANALYSIS OF RESIDUAL STRESS

Engineering problems are modeled mathematically in terms of differential equations with corresponding boundary and initial conditions. Some problems associated with analytical models such as difficult physical geometry, complex differential equations, and boundary and initial conditions requires the use of numeric methods, such as finite element method to model engineering problems. This numerical method divide the medium into small parts with discrete points called nodes and approximate the exact solution on these nodes. The nodes in a system are connected together with elements. Finite element method brings approximate results at any point of a system with complex geometry. Several researchers modeled the welding process using finite element analysis.

Numerical modeling of welding process using finite element method dates back to 1970s [103-106]. Finite element modeling aims prediction of the thermal, material and mechanical effects of welding process. The most common approach on modeling of welding process is to split the process into two steps which are thermal analysis followed by mechanical analysis. In the following decades, many studies have been published in this field. A study of residual stresses in multi pass girth but welded pipes was performed by Teng [107]. Tsirkas studied laser welding process in butt joint specimens in terms of with thermal, metallurgical and mechanical aspects. SYSWELD was used to simulate welding process [108]. Teng performed numerical and experimental investigation on residual stresses of the but-welded joints [109]. Chao studied transient temperature and residual stresses in friction stir welding of 304L stainless steel [110]. Chang investigated the effect of welding sequences on residual stress [111]. Yaghi simulated residual stress in welded sections of P91 pipes [112]. Deng predicted welding residual stress in multi pass butt welded modified 9Cr-1Mo steel pipe considering phase transformation effects [113]. Deng performed numerical simulation of temperature field and residual stress in multi pass welds in stainless steel pipe and compared them with experimental measurements [114]. Finite element prediction of residual stress distributions in multi-pass welded piping branch junction was performed by Jiang [115]. Experimental and numerical analyses of residual stress distributions in TIG welding process for 304L stainless steel was performed by Mousavi [116]. Yaghi *et. al.* simulated residual stress in welded sections of P91 pipes [117]. Murugan simulated residual stresses using finite element simulation and measured them experimentally by contour method [118]. Palazoğlu studied mechanical response of thin SMAW arc welded structures experimentally and numerically [119]. Daneshpour *et. al.* analyzed residual stress in laser spot welded steel sheets [120]. Zhang performed numerical simulation of three dimension stress field in double sided double arc multi-pass welding process [121]. Laser welding of low carbon steel and thermal stress formation was simulated by Yilbas [122]. Xu analyzed heterogenic welding joint residual stress using a commercial finite element software and developed a sequential coupling finite element procedure to calculate the welding residual stress in the welding joints [123]. Kovacevic studied thermally induced residual stress in the hybrid laser GMA welding process using numerical and experimental methods [124]. Smith performed finite element validation of the deep hole drilling method for measuring residual stresses [125]. Jiang investigated influence of residual stress on stress concentration factor for high strength steel welded joints [126]. Joshi investigated residual stresses in flux cored arc welding process in bead on plate specimens [127]. Zhang performed three dimensional finite element analysis of thermal stress in single pass multi-layer weld based rapid prototyping [128]. Fitzpatric and his colleagues performed through thickness residual stress measurement with neutron diffraction method and validated their results with finite element model [129]. Numerical investigation on weld residual stresses in tube to tube sheet joint of a steel heat exchanger with 0.06 wt % C content was performed by Xu [130]. Smith performed accurate prediction of residual stress in stainless steel welds [131]. Xu performed temperature and residual stress simulations of the NeT single bead on plate specimen using SYSWELD [132]. Ohms performed residual stress assessment by neutron diffraction and finite element modeling on a single bead weld on a steel plate [133]. Residual stress measurement by neutron diffraction and theoretical estimation in a single weld bead was performed by Price [134]. Malik analyzed circumferential arc welded thin walled cylinders to investigate the residual stress fields [135]. Deng predicted welding distortion and residual stress in a thin plate butt welded joint [136]. Deng performed finite element prediction of welding residual stress and distortion in carbon steels with 0.15 and 0.44 wt % carbon considering phase transformation effects [137]. A practical approach was developed by Nart for simulating submerged arc welding process to overcome the difficulty caused by diverge of weld pool shape from the shape of simple ellipsoid which was Goldak's double ellipsoid model [138]. Smith performed accurate prediction of residual stress in stainless steel welds [139]. Muransky investigated the effect of plasticity theory on predicted residual stress field in numerical weld analyses [140].

2.4. EFFECT OF CARBON CONTENT IN STEELS

Effect of carbon on different properties of steels was studied by various authors. Murata and Morinaga investigated the effect of carbon content on the mechanical properties of 10 Cr - 5 W ferritic steels [141]. Yang simulated the stress field of carburized specimens with different carbon content during quenching process [142]. Influence of carbon content and microstructure on corrosion behavior of low alloy steels in Cl- containing environment was investigated by Yang [143]. Effect of carbon content during quenching process on the stress field simulation of carburized specimens was investigated by Yang [144]. Influence of prior austenite deformation and nonmetallic inclusions on ferrite formation in two kinds of low carbon steels were studied by Zhang [145]. Effect of carbon content (0.45, 0.79, and 1.26 wt%) in warm deformation behavior of steels with martensite starting structure was investigated by Li *et. al* using Gleeble 3500 thermo mechanical simulator [146]. Esling *et al.* investigated carbon content dependent effect of magnetic field on austenitic decomposition of steels [147]. Influence of carbon content on strain hardening behavior of sintered plain carbon steel preforms was investigated by Narayan and Rajeshkannan [148]. Serajzadeh and Taheri investigated the effect of carbon on kinetics of dynamic restoration and flow behavior of carbon steels [149]. Effect of carbon content on high strain rate tensile properties for carbon steels was investigated by Itabashi and Kawata [150]. Mechanical properties and weather resistance of high performance bridge steels were affected by the carbon content [151]. This effect was analyzed by Guo and his colleagues.

3. METHODOLOGY

Experimental and numerical analysis of residual stress is performed in this study. Finite element technique is used for the numerical analysis. Submerged arc welding of carbon steels is simulated with ANSYS finite element software. APDL code is written to mimic details of submerged arc welding process and movement of heat source. Verification of finite element model is accomplished with experimental residual stress measurements using nondestructive ultrasonic technique.

Source of residual stress in this study is welding heat input. Residual stresses that are formed during rapid heating and cooling period is investigated. In order to observe the effect of welding process on the formation of residual stress, it is required to use steel samples with no initial stress. Steel samples provided from Ereğli Demir ve Çelik Fab. T.A.Ş. contained initial stresses that occurred during the production. It is required to perform heat treatment to remove initial stresses in these plates. However, heat treatment is a process that affects the properties of materials. It is necessary to perform heat treatment process with correct time and temperature parameters. Therefore, it is necessary to optimize this heat treatment in terms of time and temperature parameters.

Tests are performed to determine optimum annealing heat treatment process. Small samples of three type of steel plates are prepared. These steels are annealed at temperatures ranging from 100 ^{o}C to 1100 ^{o}C with 25 and 50 ^{o}C increments. Effect of annealing temperature on grain size and hardness of the material is investigated. Finally, annealing time and temperatures for each type of the material are determined.

In order to investigate the effect of carbon content in steel plates on formation of welding residual stress, it is necessary to perform welding process with constant parameters. Welding process should be accomplished with same speed for each sample. Submerged arc welding process is selected as an appropriate welding technique for this purpose.

Annealed specimens are grinded in order to obtain a smooth surface. Samples with 10 mm of thickness allowed performing a beam on plate welding process. Weld beam on plate should be applied in a weld groove in order to observe the real effect of welding process. Ultrasonic method of residuals stress measurement requires materials with flat surfaces. Accordingly, weld groove shape that will cause low deformation is determined for submerged arc welding process. This weld groove is prepared in the middle of the steel plates with length equal to one third of the length of steel plates.

Various residual stress measurement techniques are investigated. Neutron diffraction and ultrasonic techniques allow measurement of bulk residual stress through the thickness of the material. Ultrasonic technique is a cost effective technique with previously proven precision. There are different types of ultrasonic waves to measure stress. In this study longitudinal ultrasonic waves are used that allow measurement of bulk residual stress through the thickness of the material. Measured stress values are summation of longitudinal and transversal stresses.

Calibrations of ultrasonic waves with steel samples are performed in order to investigate the relation between ultrasonic wave velocity variations and stress. Thermal stress is applied to samples and relation of ultrasonic wave velocity with stress is investigated. Acoustoelastic constants for each sample are determined by this calibration processes.

Ultrasonic wave velocities in each sample are measured after annealing process. After the welding process ultrasonic wave velocity measurements are repeated at the same measurement point. Acoustoelastic constant are used to calculate the residual stress formed in the materials after welding process.

Previous studies dealt with the effect of welding type, material properties, welding sequences or residual stress measurement techniques. This is the first time that effect of carbon content on formation of welding residual stress is investigated. This is also the first time welding residual stress measurements are performed using immersion ultrasonic technique, which is known to be suitable.

3.1. MATERIAL PROPERTIES

The aim of this study is the investigation of carbon content in steels on formation of welding residual stress. Samples with similar composition but different carbon content should be selected. For this purpose three type of steels are selected from the products of Ereğli Demir ve Çelik Fab. T.A.Ş.

Table 3.1. Chemical composition of steel samples

	C	MN	P	S	SI	ALT	CU	CR	NI	MO	V	NB	CA	AS	TI
IF	0.003	0.506	0.036	0.007	0.01	0.043	0.033	0.03	0.079	0.002	0.001	0.001	0	0.007	0.023
5237	0.092	0.679	0.013	0.014	0.185	0.045	0.075	0.052	0.062	0.006	0.001	0.001	0.001	0.005	0.002
5045	0.478	0.757	0.013	0.004	0.2	0.041	0.03	0.022	0.055	0.001	0.004	0	0	0.016	0.001

First steel with lowest carbon content is interstitial free (IF) steel. This type of steel is produced with very low amounts of interstitial elements such as carbon and nitrogen. Small amount of titanium is added to tie up the remaining interstitial atoms. Low carbon steel is with 5237 and medium carbon steel is with 5045 product codes. Low carbon steel have carbon content of 0.092 wt % and medium carbon steel have carbon content of 0.478 wt %. Chemical compositions of selected samples are given in Table 3.1.

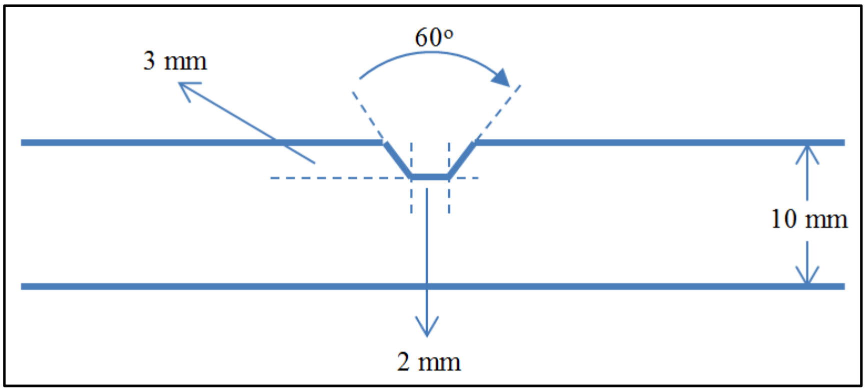

Figure 3.1. Dimensions of weld groove

Cold rolled samples are with dimensions of 280 × 200 × 10 mm as illustrated in Figure 3.1. Three samples are prepared for each type of steel. Samples are annealed in order to remove production residual stress. After the annealing process, samples are grinded and same weld grooves are prepared in each sample. Weld groove is prepared for a beam on plate weld process. Weld grooves lied along the length of the samples in the center of the plate as illustrated in Figure 3.2. Length of the weld groove is 1/3 of the length of the sample. Depth of the weld groove is 3 mm with an angle of 60^o.

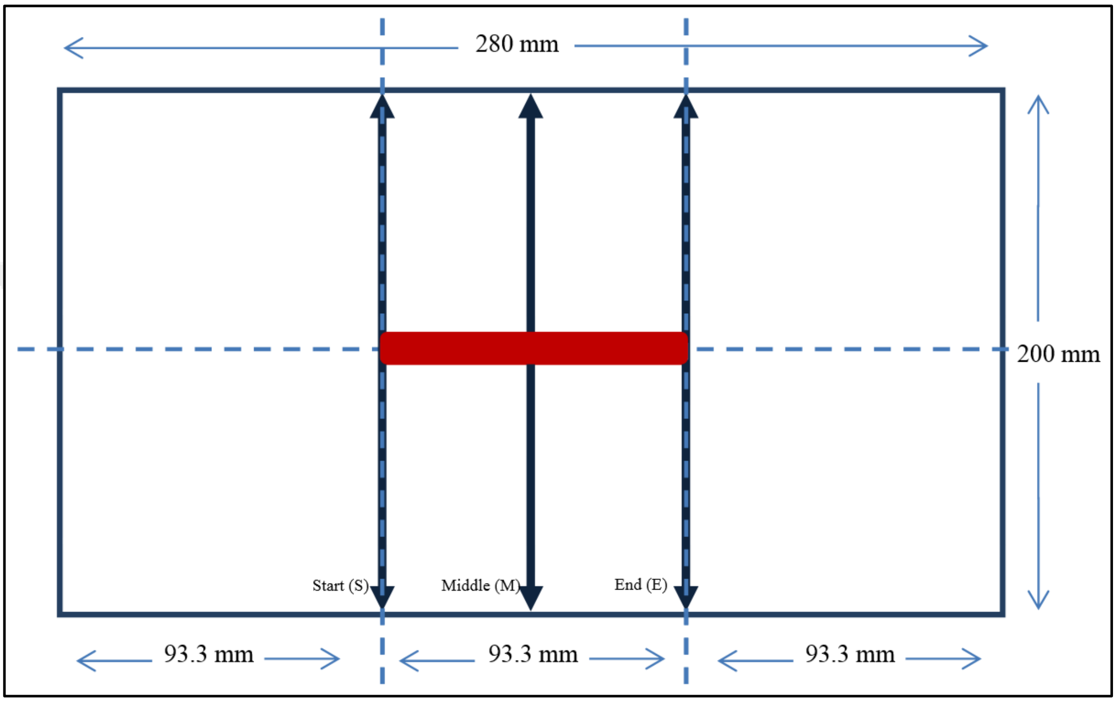

Figure 3.2. Dimensional illustration of plate and weld groove and ultrasonic wave velocity measurement points as start, middle and end sections

3.2. ANNEALING

Annealing is heat treatment process consisting of heating to and holding at a specific temperature which is followed by cooling at an appropriate rate. This process causes softening of metallic materials. Steels are being heat treated to facilitate cold working or machining, to improve mechanical or electrical properties, or to promote dimensional stability [152].

Iron-carbon phase diagram is the guide to determine annealing parameters for steels. Critical temperatures for start and end of austenite transformation are illustrated in Figure

3.3. There are also analytical equations to determine upper and lower critical temperatures using actual composition of the steel.

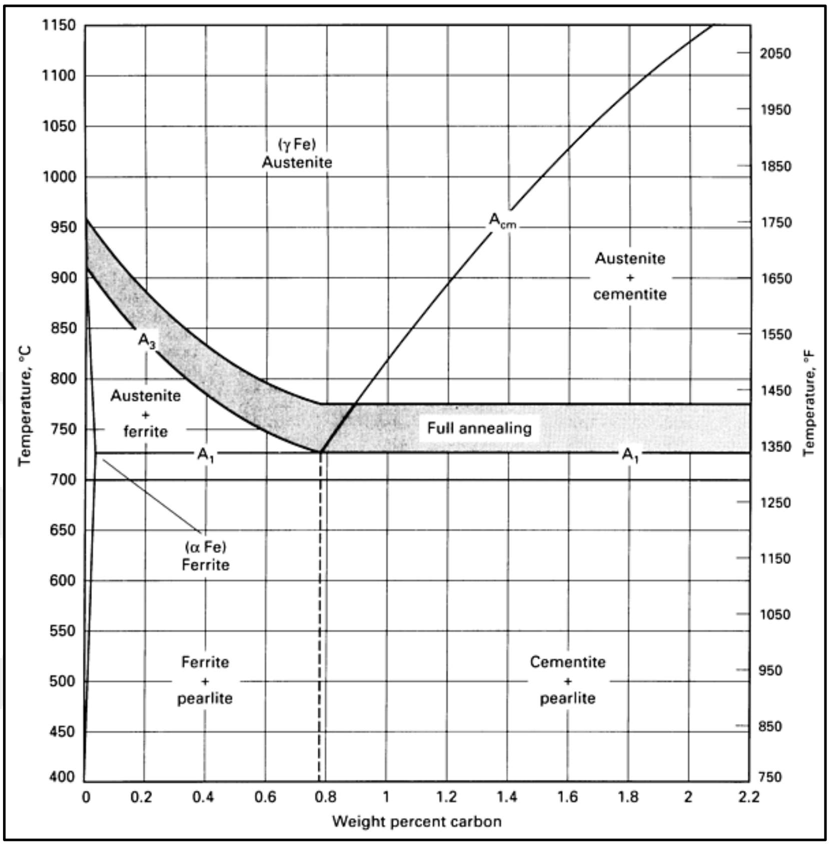

Figure 3.3. The iron-carbon binary phase diagram showing region of temperatures for full annealing [153]

There are various thermal cycles in order to achieve different goals of annealing. Annealing types are classified according to the temperature which the steel is heated and to the method of cooling used. There are three types of annealing process. Subcritical annealing is performed if the maximum temperature is below the lower critical temperature (A1). Intercritical annealing is accomplished if the maximum temperature is above A1 but below the upper critical temperature (A3). Full annealing is performed at the maximum temperature above A3.

Hypotetic steels have carbon content less than 0.77 weight percent. At this practice full austenitization is being attained above the upper critical temperature (A3) in hypotetic steels. Safe region for full annealing process is illustrated in Figure 3.3. This region can be determined as 50 °C above the upper critical temperature.

There are three main stages of annealing. Recovery is the first stage of annealing process. In this stage, material properties do not change. Hardness, ductility, and strength remain constant or very little changes occur. In addition, grain sizes remain unchanged. In the second stage of annealing, new crystals start to form and that stage is called recrystallization stage. Formation of new crystals causes rapid decrease in hardness and strength. Size of old grains reduces and finally disappear. Sizes of new grains increase. At the end of this stage, a homogeneous distribution of new grains is obtained but these grains are smaller that initial grains. Ductility is another important property that is rapidly increased during this period. Final stage is continuation of grain growth. During this stage, decrease in hardness and strength slows down but still continues.

In this study, it is aimed to observe annealing stages of each type of steel used. Samples with dimensions of 20 × 20 × 10 mm are prepared by sectioning. Each sample is annealed for two hours at varying temperatures from 100 °C to 1150 °C at 25 and 50 °C increments.

Samples are heated to the desired temperature. Then each sample is kept at the maximum temperature for 2 hours. After that period of time, oven is shut down and allowed to cool down slowly as shown in Figure 3.5. Cooling took place in the oven and its period depended on the maximum temperature.

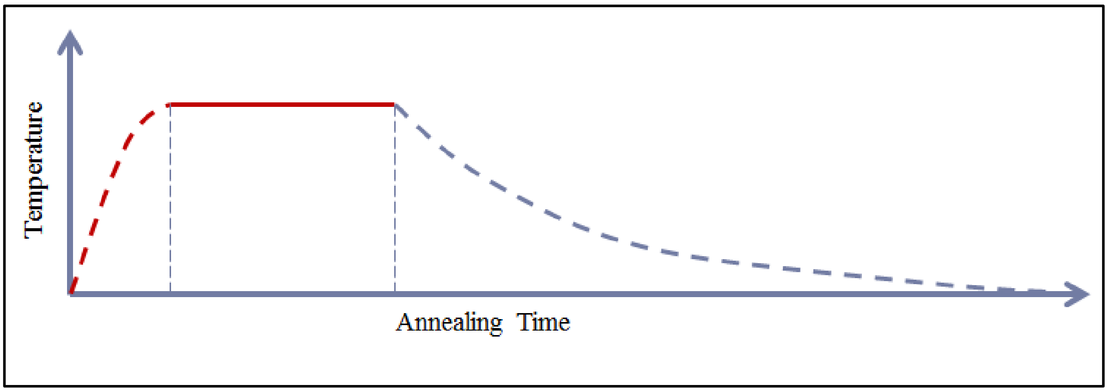

Figure 3.5. Heating and cooling stages of annealing process

In order to observe annealing stages, hardness measurements are performed before and after the annealing process. Another property that is affected by annealing process is grain size of samples. Grain sizes are measured with a metallography study after each annealing process.

3.3. HARDNESS TEST

Rockwell hardness test is an easy method of hardness measurement which can be applied to a wide variety of materials such as low alloy or hardest steels [154]. Short measurement time and digital readers allow gathering large amounts of data easily Mostly readings are provided digitally. These advantages differentiate that method from other hardness test methods such as Brinel or Vickers hardness testing.

The depth of a prescribed load is determined and converted to a hardness number in Rockwell test [155]. The hardness value is inversely related to the depth. Rockwell Hardness test is performed with a conical or a spherical indenter as illustrated in Figure 3.6. Conical indenter is used for hard materials while spherical indenter is used for softer materials. Conical indenter is classified in Rockwell C scale and spherical intender is classified in C scale.

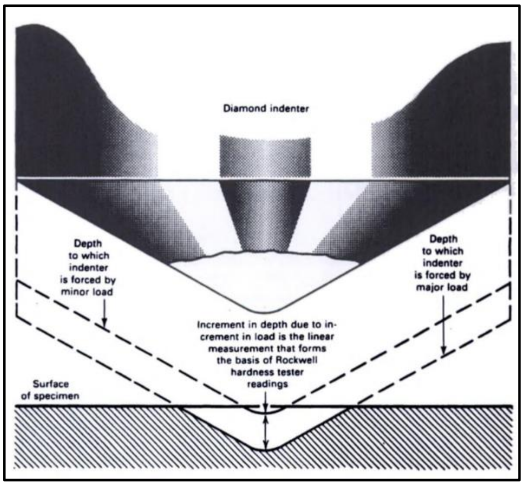

Figure 3.6. Principle of hardness test [155]

The Rockwell hardness is defined with Equation 3.1 [156].

$$HR = N - \frac{h}{S} \tag{3.1}$$

where HR is Rockwell hardness, N is numerical constant, h is remaining depth of penetration in mm, and S is scale division in mm. N, the numerical constant, is defined to facilitate the calculation of the test results. S, the scale division, is defined related to the required resolution. There are various Rockwell scales that are marked by additional capital letter to HR. For instance, HRA is selected for sinter hard metals while HRE is used for cars iron or aluminum.

The Rockwell Hardness scales are selected according to indentation hardness of a material. HRB scale is used for soft and middle hardness steel, aluminum, and brass. Survey parameters of the HRB testing procedure according to Rockwell which are standardized in ISO 6508 and ASTM E 18 are given in Table 3.2.

Table 3.2. HRB testing parameters according to Rockwell

Numerical Constant, N	130
Scale Division, S	0.002
Type of the indenter	Ball 1.5875 mm
Preliminary test force, F_0	98.07
Additional test, F_1	882.6
Scope	20 HRB to 100 HRB

In this study soft and middle hardness steels are used. The most appropriate Rockwell hardness scale is selected to be HRB. The Rockwell hardness test requires samples with smooth surfaces. In order to accomplish this each sample is grinded. Grinding is performed with abrasive grinding papers with grit sizes of 80, 200, 320, 800 and 1200. Hardness tests are repeated 10 times for each sample. Average and standard deviation of these 10 measurements are calculated.

Hardness measurements are performed before and after the annealing of each sample. Materials are grinded before hardness test and after the annealing process. Variation in the hardness of a sample according to annealing temperature is observed.

3.4. METALLOGRAPHY

The structure and properties of materials are correlated through metallography procedures. Widely used metallographic imaging techniques are hot-stage microscopy, transmission electron microscopy, X-ray analysis and scanning electron microscopy [157], covering a wide range of magnification levels. Generally magnification ranges from 50 to 1000x are required in order to observe microstructural features of 0.2 µm or larger [158].

Metallographic stages are composed of sectioning, mounting, grinding with polishing, etching and examination. During the specimen preparation, the sample of interest is sectioned from the specimen. Selected specimens are prepared for grinding by mounting in a polymer. Finally, etching is performed to reveal the specific structure of the microstructure.

Sectioning should be carefully performed without altering or destroying the structure of the material. Abrasive cutting is the most versatile and economical sectioning method [159]. Abrasive wheels are composed of abrasive grains that easily wear out during cutting. In this study cutting wheels with Al_2O_3 grains and bakelite binder is used which is applicable for steels, ferrous materials and hardened steels.

Bulk materials do not require mounting. However, using small or oddly shaped materials makes it necessary to perform mounting [160]. In this study, steel samples are sectioned to have dimensions of 20 × 20 × 10 mm. These bulk samples do not require mounting. They are easily grinded and polished without mounting into polymer.

Surface of the samples should be treated by physical and chemical methods in order to remove various structural constituents. Water lubricant abrasive wheels are generally used for grinding of the specimen surface. This process produces flat surface with minimum depth of deformed metal [161]. In this study, grinding is performed with abrasive grinding papers with grit sizes of 80, 200, 320, 800 and 1200. The surface damage remaining from each grinding stage is removed by performing the next stage in perpendicular direction of the previous one.

Polishing should be performed with a fine abrasive and an appropriate liquid. Diamond, alumina (Al_2O_3) and magnesium oxide (MgO) are the most common abrasives. In this study alumina in water is used and specimen is held against the rotating wheel.

Etching is the vital step of metallography in order to reveal the microstructure of a metal or alloy. Polished specimens are not adequate for investigation of microstructural details such as grain, grain boundaries, twins, slip lines, and phase boundaries. Areas of different crystal orientations, crystalline imperfections, or different compositions are attacked by etchants at different rates. As a result of this process surface irregularities occur which reflect the incident light, producing contrast and allow the visualization of microstructural details. In this study, etching is performed with nital which is composed of 5 % nitric acid and 95 % ethanol. Etching time is varied between 30 to 60 seconds. This time is determined with trial and error that allows visualization of grains without being over etched.

Optical microscopy allows magnification on polished and etched surface in order to characterize grain and phase structures [161]. Reflected light microscopy is preferred in imaging of metallic microstructures [158]. Most of the microstructural characteristics of materials can be detected and identified using light microscope. There are two type of light microscopes; upright and inverted. This classification is related to the orientation of the light path to the polished plane of the specimen as illustrated in Figure 3.7.

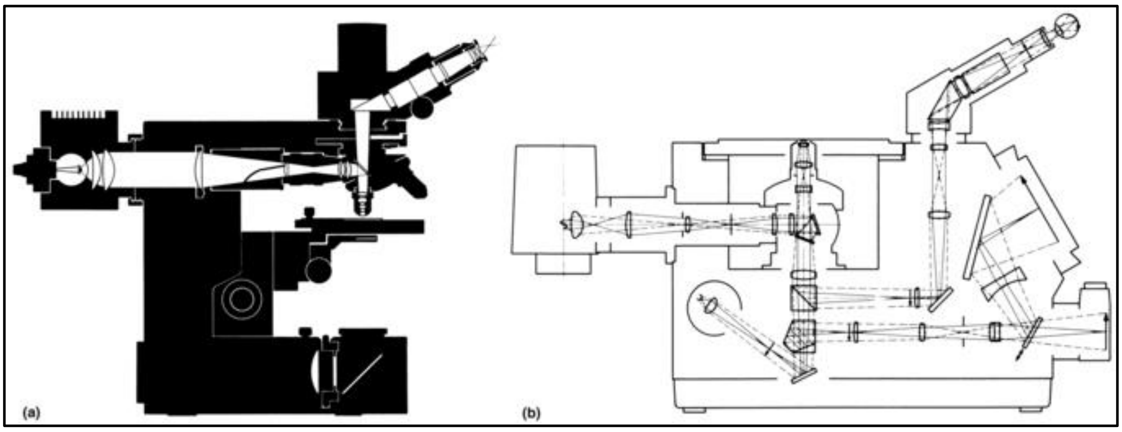

Figure 3.7. Light paths in a. an upright incident-light microscope and b. an inverted incident-light microscope

Scanning electron microscopy (SEM) uses the interaction between electrons and materials to investigate the microstructure of materials. For this purpose secondary and backscattered electrons, electron-beam-induced currents, X-ray and Auger electrons, electron channeling effects and cathode luminescence are used [162]. SEM provides a resolution range that reaches up to a few nanometers using secondary electrons. Higher resolutions can be obtained by backscattered electrons to image the sample topography and the crystal orientation. This technique also provides a greater depth of field compared to optical microscopy. Figure 3.8 illustrates design of a scanning electron microscope for secondary and backscattered electron imaging [158].

In this study inverted optical microscope with digital imaging system is used for grain size investigation of IF and low carbon steels after each annealing stage. Grains of medium carbon steel could not be visualized using optical microscope. Consequently, scanning electron microscopy is used for grain size characterization of medium carbon steels. Flow chart of the whole process is given in Figure 3.9.

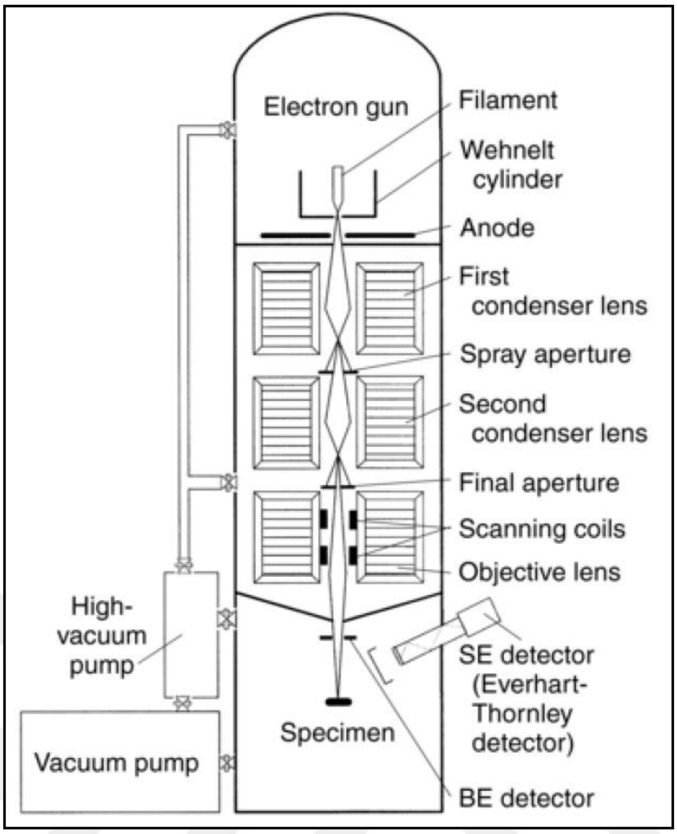

Figure 3.8. Typical design (schematic) of a scanning electron microscope for secondary and backscattered electron imaging. SE, secondary electron; BE, backscattered electron [158]

ImageJ is a Java-based open-source image processing software developed at the National Institutes of Health [163]. It has various applications such as three-dimensional live-cell imaging [164], radiological image processing [165], and multiple imaging system data comparisons [166]. In this study grain size measurement are performed by particle size analysis capability of ImageJ software. The software first determines the grain boundaries and then calculates the area within each bounded zone within the image. Finally grain size for each image is determined by calculating the average area of bounded zones.

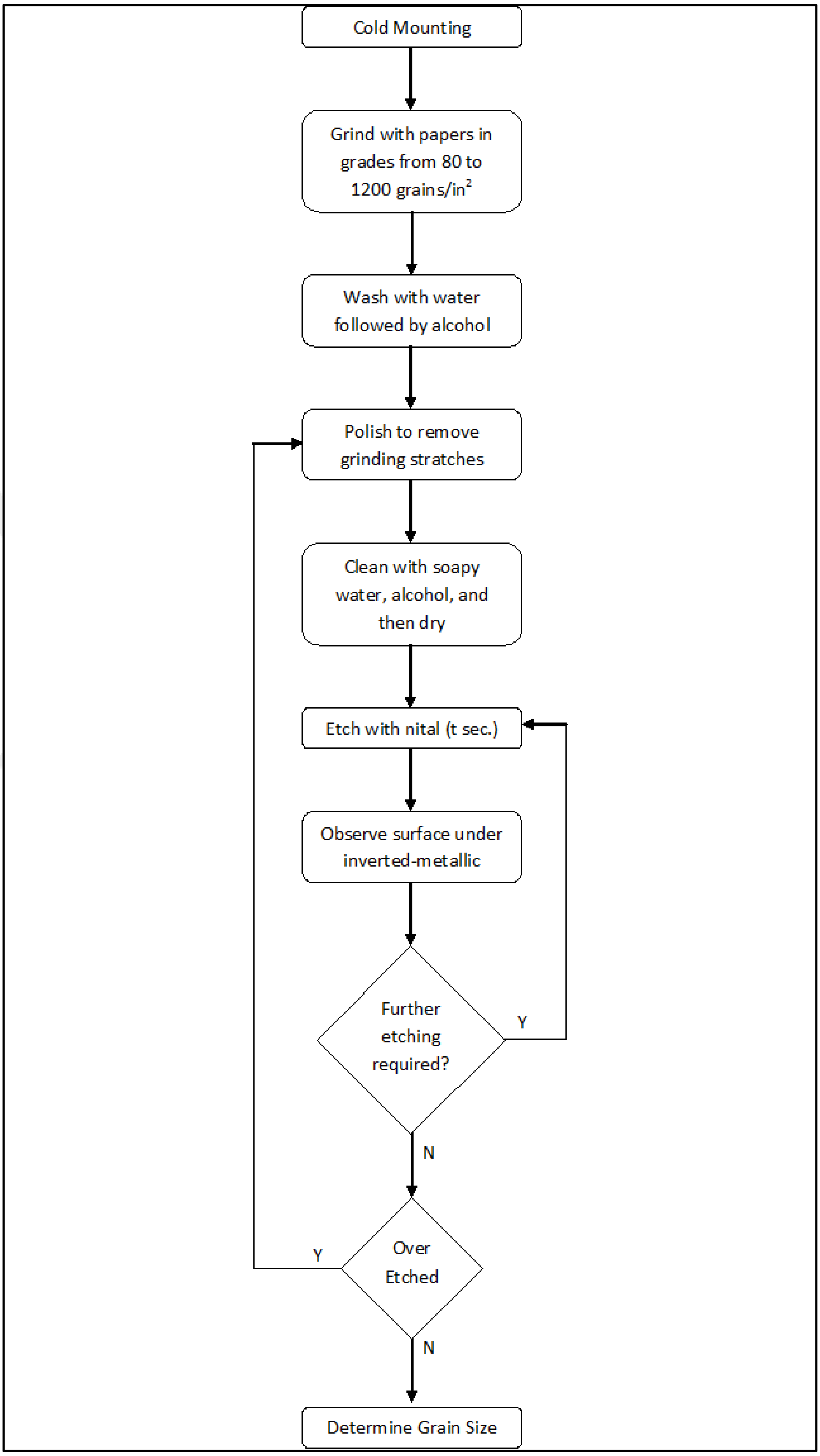

Figure 3.9. Flow chart of metallography process

3.5. WELDING

Welding is a process in which materials of the same fundamental type or class are brought together and caused to join through the formation of primary chemical bonds under the combined action of heat and pressure [167]. It is one of the main production processes, with its ancient origins in the fire of blacksmith by joining two hot metal pieces with hammer blows, including buildings, vehicles, bridges and more. Various weld types are used at sites for welding of sheets, pipes, plates and sections. It is a cost-effective joining method for metals which is suitable for high thickness ranges from millimeters to one third of a meter and is applicable to a wide range of component shapes and sizes. Welding is able to save production cost by weight reduction and simplified logistics during manufacturing. In addition, weld joints are strong, permanent, leak tight, reproducible, and easily investigated by non-destructive test techniques.

Principle of welding is to hold atoms of two pieces of material together after a joining process. When two or more atoms are separated by an infinite distance and do not sense one another's presence, there is no force of attraction or repulsion between them. On the other hand, as they are brought together from this infinite separation, a force of electrostatic (Coulombic) attraction arises between the positively charged nuclei and negatively charged electron clouds and this force increases with decreasing separation. The potential energy of the separated atoms also decreases as the atoms come together. This is shown in Figures 3.10 and 3.11 [168].

As the distance of separation decreases to the order of a few atom diameters the electrons of the approaching atoms begin to feel one another's presence and a repulsion force between the negatively charged electron densities increases more rapidly than the attractive force. The attractive and repulsive forces combine to create a net force, which at some separation distance becomes zero as the two forces exactly offset one another. At this equilibrium spacing, the net potential energy is a minimum, the aggregate of atoms is stable, and the atoms are said to be bonded [168].

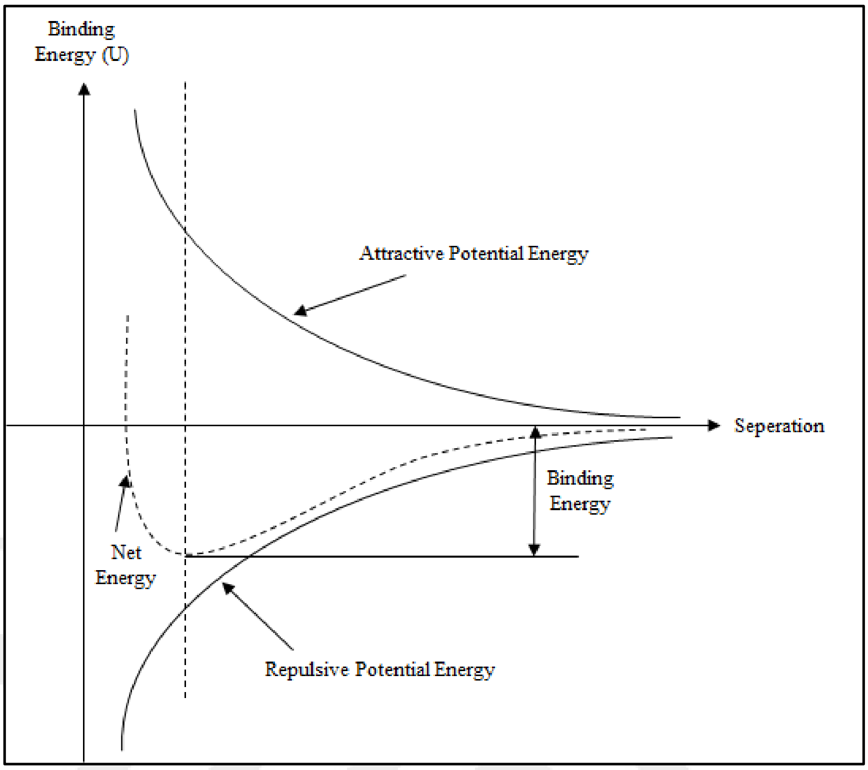

Figure 3.10. The energy curve for bonding [168]

The potential energy and the forces of attraction and repulsion are related by the formula $F = -dU/dx$ where F is the force of attraction or repulsion, U is the potential energy of attraction or repulsion, and x is the distance of separation. Differentiation with this equation gives force-distance curve [168].

The tendency for atoms to bond is the fundamental basis for welding. All that is required to produce a weld is to bring a large number of atoms together to their equilibrium spacing to produce aggregates. Separate aggregates are brought together to do the same for atoms comprising their surfaces at mating interfaces. For metals, all of the atoms comprising the aggregate take up regular positions on a three-dimensional arrangement of points in space called a crystal lattice. The result of bonding is the creation of continuity between aggregates or crystals [168].

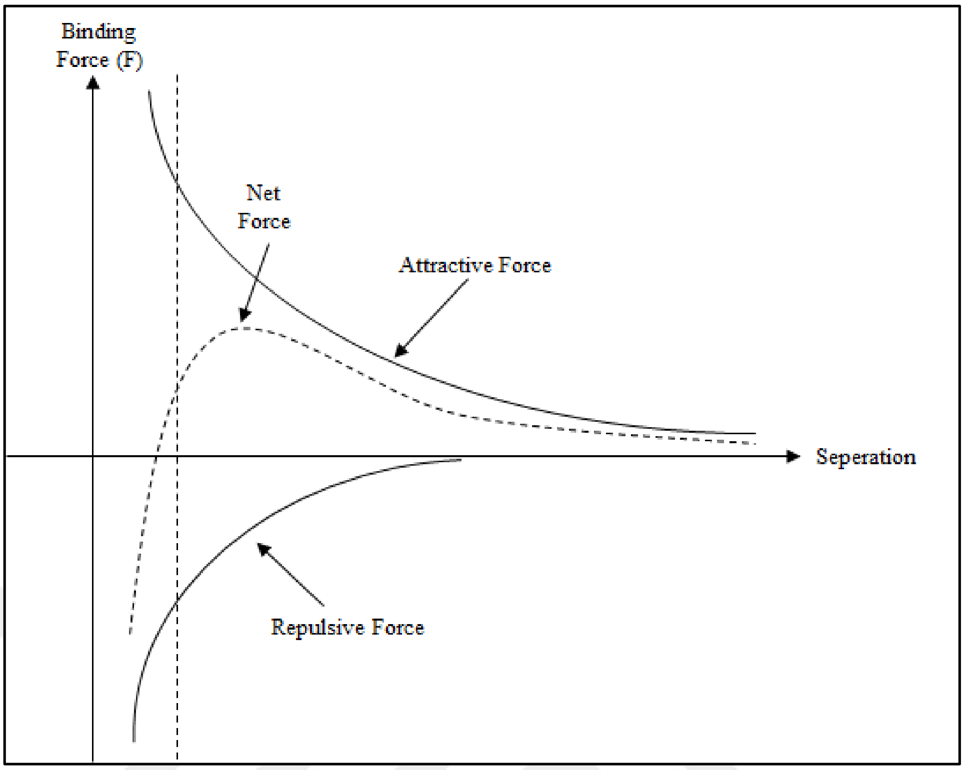

Figure 3.11. Differentiation of the potential energy gives force-distance curve [168]

In submerged arc welding (SAW) metals are melted and joined by heating them with an arc established between the wire electrode and the metal. A molten slag and granular flux shield the arc and the molten weld metal. Because the arc is submerged, it is invisible. A continuous solid wire electrode is supplied that produce filler. SAW process has high energy transfer efficiency from the electrode source to the work piece [169].

The molten slug provides clean welds by protecting and refining. Moreover, submerged arc minimizes spatter and heat losses at high welding currents. Deposition rate can be increased with multiple wires or with two or more electrodes. High deposition rate allows welding of very thick work pieces. On the other hand, SAW process is limited to flat-position welding due to large volume of molten slag and metal pool [169].

Table 3.3. Chemical composition of AWS EM12K submerged arc wire

	Chemical Compositon
C	0.05-0.15
Mn	0.80-1.25
Si	0.10-0.35
S	< 0.030
P	< 0.030
F	Balance

In this study, welding process is performed in TEKFEN Manufacturing and Engineering Co. lnc. Facility. AWS EM12K submerged arc wire is used during the welding process which is used at welding of carbon and low alloy steels. Chemical composition of welding material is given in Table 3.3.

Table 3.4. Parameters of submerged arc welding process

Electric potential energy (Volt)	30
Electric current (Amp)	500
Efficiency (%)	84
Torch travel length (mm)	90
Time (s)	6.75

Welding process is performed on each sample with the same parameters which are given in Table 3.4. In the study, “Thermal Efficiency of Arc Welding Processes”, the effect of welding parameters and process type on arc and melting efficiency is evaluated [170]. Authors compared various arc welding processes and determined the efficiency of submerged arc welding process. Accordingly, this value is accepted as the efficiency of welding process performed in this study.

3.6. ULTRASONIC TEST

Conceptually, variations of the ultrasonic wave speed due to stress can be described by the relation given below [171]

$$V = V_o + L \tag{3.2}$$

where V_0, is the velocity of a wave in an unstressed medium, σ is the stress and L is a material dependent parameter known as the acoustoelastic constant. Three main experimental measurement techniques depending on the placement of transmitting and receiving transducers can be used as illustrated in Figure 3.12.

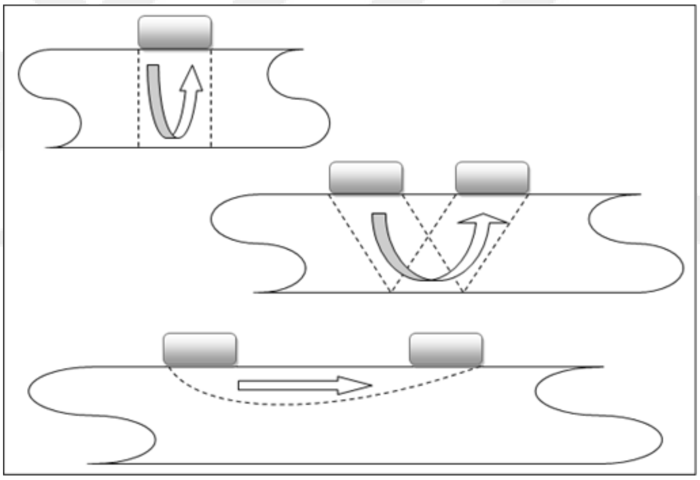

Figure 3.12. Schematic view of three measurement techniques [171]

In the first technique, waves are transmitted and received with the same transducer which is called pulse-echo (monostatic). In the other two techniques, wave are transmitted and received with different transducers which is called pitch-catch (bistatic).

Ultrasonic method gives information about the interior of the material. In the first and second techniques, waves propagate through the material thickness and reflect back. This allows to measure stress in the path of the waves. Other technique is performed using Rayleigh waves. Waves propagate in a limited thickness, a few mm or more, from the surface and make it possible to measure surface stresses. When compared with other surface techniques, this method allows measurement for larger thicknesses.

Other advantages of the ultrasonic technique are the facts that the instrumentation is convenient to use, easy to set up, portable, inexpensive, and free of radiation hazards. Problems include low spatial resolution, susceptibility to competing sources of velocity shifts due to micro structural effects and temperature variations, and the necessity for very precise time measurements [171].

3.6.1. Physical Principles

An understanding of the physical properties of materials such as Young's modulus and shear modulus are based on the interatomic forces that hold atoms together and the ways in which atoms are held together. Atomic bonds holds atoms together which act like a spring as illustrated in Figure 3.13. At large distances, interactions between the atoms are negligible. However, as the atoms get closer, they exert forces on each other and held together which are attractive and repulsive forces.

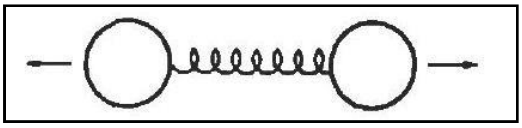

Figure 3.13. The spring like bond between two atoms [168]

Mainly atoms are held together by primary bonds and inter-atomic forces. Strong bonds are ionic, covalent and metallic bonds which are relatively strong and have high melting points. Inter-atomic forces are Van der Waals and hydrogen bond which are relatively weak and have low melting points. Metals are held by metallic and covalent type of primary bonds which are strong bonds and bring high moduli.

When two atoms separated by a distance r and the equilibrium separation r_0 is the position of minimum energy, for small displacements about that equilibrium position, the energy and force may be expanded as a Taylor series in the displacement as given by by Equation 3.3 and 3.4.

$$U = \frac{c(r-r_0)^2}{2} - \frac{c(r-r_0)^3}{3} + \cdots \tag{3.3}$$

$$F = \frac{\partial U}{\partial r} = c(r-r_0) - d(r-r_0) + \cdots \tag{3.4}$$

Where c and d are constants defining the harmonic and the first inharmonic contribution respectively [171].

The interatomic bond of two ions is described by the sum of attractive and repulsive energy terms. The force of attraction which holds ions of an ionic bond together is given by Equation 3.5.

$$F = {q^2}\Big/{4\pi\varepsilon_0 r^2} \tag{3.5}$$

where q is the charge on each ion, ε_0 is the permittivity of vacuum and r is the separation of ions. The attractive energy determined by using the force of attraction given by Equation 3.6.

$$U_a = \int_r^\infty F\partial r \tag{3.6}$$

The repulsive energy caused by the repulsion of two nuclei given by Equation 3.7.

$$U_r = {q^2 r_0^{n-1}}\Big/{4\pi\varepsilon_0 r^n} \tag{3.7}$$

where n is large power and r_0 is the equilibrium atomic bond length.

Covalent bonding is based on sharing of electrons which leads to reduction of energy and a stable bond. The energy of covalent bond is described by the empirical Equation 3.8.

$$U = -\frac{A}{r^m} + \frac{B}{r^n} \tag{3.8}$$

where m, n, A, and B are constants.

R. N. Thurston explained the development of the basic equations needed to describe waves in fluids and solids in terms of continuum mechanics [172]. Averages of interatomic forces can be used to determine the macroscopic elastic response of a solid as summarized by W. Y. Lu *et. al.* [171]. In one dimensional case relation between stress and strain is determined as given in Equation 3.9 where M is the linear modulus and M' is a nonlinear modulus.

$$\sigma = M\varepsilon + M'\varepsilon^2 \tag{3.9}$$

Stress and strain can be defined for a statically loaded material in which the propagation of an ultrasonic wave occurs as given in Equations 3.13.a and 3.13.b. In these equations the subscript “0” and “1” refer to the static and dynamic components of the fields, ω is the angular frequency which is defined as $2\pi f$, k is the wave vector which is defined as $2\pi/\lambda$, and “*” is used to denote complex conjugation.

$$\sigma = \sigma_0 + \left(\frac{\sigma_1}{2}e^{j\omega t} + \frac{\sigma_1^*}{2}e^{-j\omega t}\right) \tag{3.10.a}$$

$$\varepsilon = \varepsilon_0 + \left(\frac{\varepsilon_1}{2}e^{j\omega t} + \frac{\varepsilon_1^*}{2}e^{-j\omega t}\right) \tag{3.10.b}$$

After substitution of Equations 3.13.a and 3.13.b into Equation 3.12, Equation 3.14 is obtained.

$$\sigma_1 = (M + 2M'\varepsilon_0)\varepsilon_1 \tag{3.11}$$

The nonlinear of Hooke’s Law is incorporated into the one dimensional wave equation as given in Equation 3.12 where ρ is the density which is equal to $\rho_0/(1+\varepsilon)$ where ρ_0 is the strain free density, u is the displacement, and $\partial u/\partial x$ is ε.

$$\rho\frac{\partial^2 u}{\partial t^2}=\left(M+\frac{M'}{M}\sigma_0\right)\frac{\partial^2 u}{\partial x^2} \tag{3.12}$$

Finally it is concluded that the lowest order in stress, the velocity of wave propagation is defined with Equation 3.13 which is in the form of Equation 3.16.

$$V=\left(\frac{M}{\rho_0}\right)^{1/2}\left[1+\frac{1}{2}\left(1+2\frac{M'}{M}\right)\frac{\sigma_0}{M}\right] \tag{3.13}$$

3.6.2. Acoustoelastic Effect

The medium in which waves propagate is defined as a continuum. In continuum approach, structural parameters are related to properties of an equivalent continuous medium. By using continuum mechanics it is possible to postulate fields of density, stress, velocity etc., since these fields satisfy the basic conservation laws of equations related with the balance of mass, momentum, angular momentum and energy. In addition, a particular medium can be characterized by constitutive relations which relate the stress to other variables [172]. Acoustoelasticity determines the relation between changes in elastic structure of continuum and velocity of waves in the medium.

Acoustoelasticity is the theory of elastic wave propagation through elastic medium. This theory states that the velocity of elastic wave propagation in solids is dependent on the mechanical stress [171]. Acoustic wave propagation, in solids, is depended on the material’s mass and elastic properties. As an example, for an infinitely large solid medium physical acoustic theory indicates that sound wave velocities are functions of Young’s modulus and shear modulus [172]. Young’s modulus and shear modulus are related to stress, therefore variations on stress affect the velocity of elastic wave propagation. Longitudinal (V_L) and shear (V_S) wave velocities are given in Equations 3.14 and 3.15 respectively.

$$V_L = \sqrt{\frac{E(1-v)}{\rho(1+v)(1-sv)}} \tag{3.14}$$

$$V_S = \sqrt{\frac{G}{\rho}} \tag{3.15}$$

where E is Young's modulus, G is shear modulus, ρ is density and v is Poisson's ratio.

Hughes and Kelly [173] derived expressions for the speeds of elastic waves in stressed solids using Murnaghan's [174] theory of finite deformations and third-order terms for *energy*. The speed of waves propagating in the direction 1 and having particle displacements in the 1,2 and 3 directions in an initially isotropic body subjected to a homogeneous triaxial strain field are given by Equation 3.16 which are illustrated in Figure 3.14.

$$\rho_0 V_{11}^2 = \lambda + 2\mu + (2l + \lambda)\theta + (4m + 4\lambda + 10\mu)\alpha_1 \tag{3.16.a}$$

$$\rho_0 V_{12}^2 = \mu + (\lambda + m)\theta + 4\mu\alpha_1 + 2\mu\alpha_2 - \frac{1}{2}n\alpha_3 \tag{3.16.b}$$

$$\rho_0 V_{13}^2 = \mu + (\lambda + m)\theta + 4\mu\alpha_1 + 2\mu\alpha_3 - \frac{1}{2}n\alpha_2 \tag{3.16.c}$$

where, ρ_0 is initial density, V_{11}, V_{12}, V_{13} are speed of waves propagating in the 1 direction with particle displacements in the 1, 2, 3 directions respectively, λ, μ are Lame or second-order elastic constant, l, m, n are Murnaghan's third-order elastic constant, $\alpha_1, \alpha_2, \alpha_3$ are components of the homogeneous triaxial principal strains in the 1,2,3 directions and θ is $\alpha_1 + \alpha_2 + \alpha_3$.

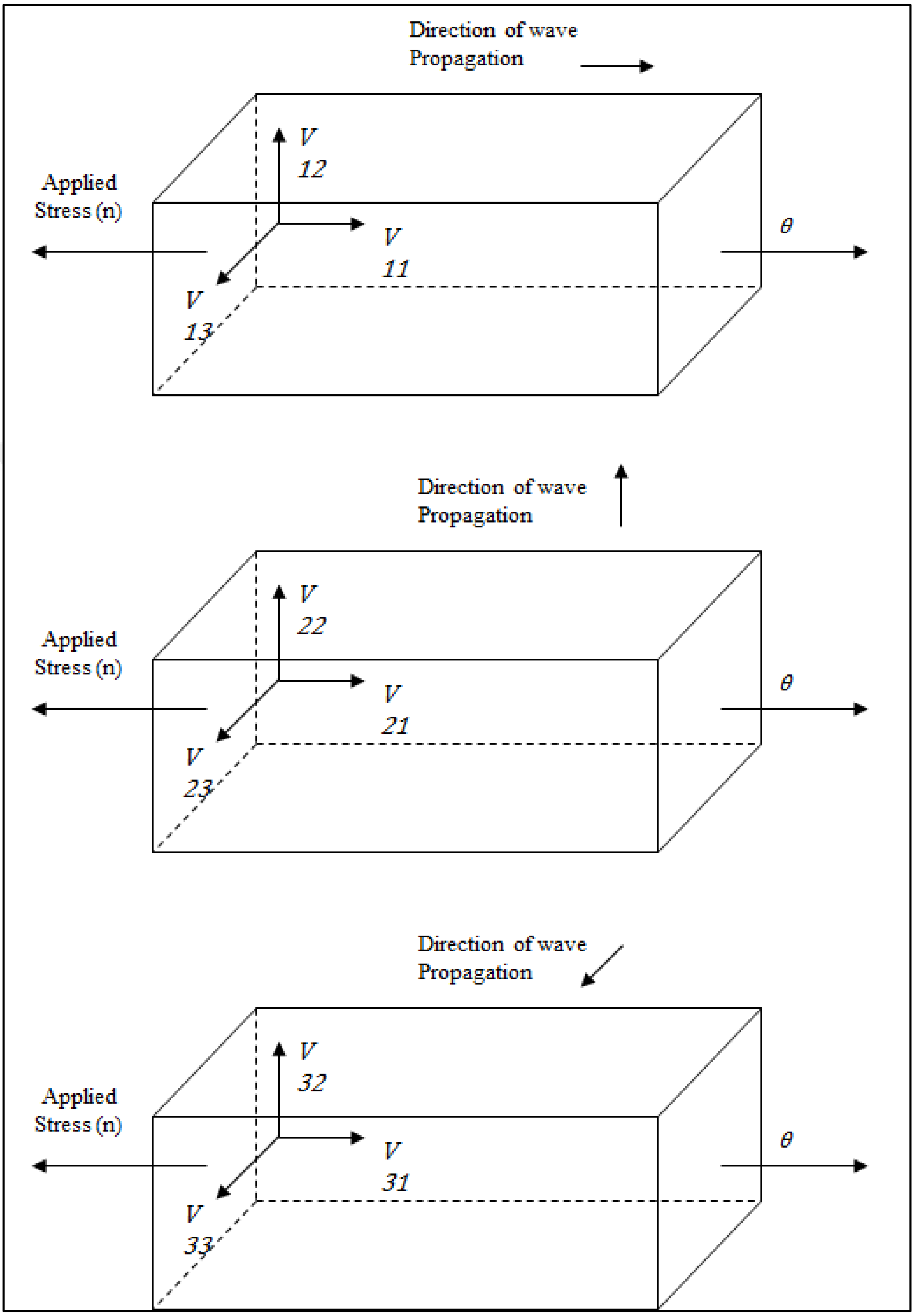

Figure 3.14. Velocity of plane waves and stress field on orthogonal coordinate system [175]

For a state of uniaxial stress, there are five unique wave speeds which may be determined from Equations 3.17. First consider the stress acting in the 1 direction. The strains are $\alpha_1 = \varepsilon$ and $\alpha_2=\alpha_3=-\nu\varepsilon$ where ν is Poisson's ratio. Equation 3.16 [58] reduce to

$$\rho_0 V_{11}^2 = \lambda + 2\mu + [4(\lambda + 2\mu) + 2(\mu + 2m) + \nu\mu(1 + 2l\,/\,\lambda)]\epsilon \qquad (3.17.a)$$

$$\rho_0 V_{12}^2 = \rho_0 V_{13}^2 = \mu + [4\mu + \nu(n/2) + m(1 - 2\nu)]\epsilon \qquad (3.17.b)$$

The speeds of plane waves travelling perpendicular to the uniaxial stress may also be determined from Equation 3.18.

$$\rho_0 V_{22}^2 = \lambda + 2\mu + [2l(1 - 2\nu) - 4\nu(m + \lambda + 2\mu)]\epsilon \qquad (3.18.a)$$

$$\rho_0 V_{21}^2 = \rho_0 V_{31}^2 = \mu + [(m + \lambda + 2\mu)(1 - 2\nu) - \nu n/2]\epsilon \qquad (3.18.b)$$

$$\rho_0 V_{23}^2 = \rho_0 V_{32}^2 = \mu + [(m + \lambda)(1 - 2\nu) - 6\nu\mu - n/2]\epsilon \qquad (3.18.c)$$

The relative changes in wave speed with axial strain may be calculated from Equation 3.17 and 3.18 if it is assumed that the relative changes are small. The resulting equations are

$$\frac{\partial V_{11}/V_{11}^0}{\partial \varepsilon} = 2 + \frac{\mu + 2m + \nu\mu(l + 2l/\lambda)}{\lambda + 2\mu} = L_{11} \qquad (3.19.a)$$

$$\frac{\partial V_{12}/V_{12}^0}{\partial \varepsilon} = 2 + \frac{\nu n}{4\mu} + \frac{m}{2(\lambda + \mu)} = L_{12} \qquad (3.19.b)$$

$$\frac{\partial V_{22}/V_{22}^0}{\partial \varepsilon} = -2\nu\left(1 + \frac{m - \mu l/\lambda}{\lambda + 2\mu}\right) = L_{22} \qquad (3.19.c)$$

$$\frac{\partial V_{21}/V_{21}^0}{\partial \varepsilon} = \frac{\lambda + 2\mu + m}{2(\lambda + \mu)} + \frac{\nu n}{4\mu} = L_{21} \qquad (3.19.d)$$

$$\frac{\partial V_{23}/V_{23}^{0}}{\partial \varepsilon} = \frac{(m-2\lambda)}{2(\lambda+\mu)} - \frac{n}{4\mu} = L_{23} \tag{3.19.e}$$

In Equation 3.19, L_{ij} is the acoustoelastic constant and the superscript 0 indicates the wave speed at zero axial strain.

The third order constants l, m, n may be evaluated in terms of the relative changes in wave speeds by inverting the set of three equations consisting of either Equations 3.20.a or 3.20.c and two of Equations 3.20.b, 3.20.d, and 3.20.e. Using the Equations 3.20.c to 3.20.e one may express the constants as

$$l = \frac{\lambda}{1-2\nu}\left[\frac{1-\nu}{\nu}\frac{\partial V_{22}/V_{22}^{0}}{\partial \varepsilon} + \frac{2}{1+\nu}\left(\frac{\partial V_{21}/V_{21}^{0}}{\partial \varepsilon} + \nu\frac{\partial V_{23}/V_{23}^{0}}{\partial \varepsilon}\right) + 2\nu\right] \tag{3.20.a}$$

$$m = 2(\lambda+\mu)\left(\frac{\nu}{1+\nu}\frac{\partial V_{23}/V_{23}^{0}}{\partial \varepsilon} + \frac{1}{1+\nu}\frac{\partial V_{21}/V_{21}^{0}}{\partial \varepsilon} + 2\nu - 1\right) \tag{3.20.b}$$

$$n = \frac{4\mu}{1+\nu}\left(\frac{\partial V_{21}/V_{21}^{0}}{\partial \varepsilon} - \frac{\partial V_{23}/V_{23}^{0}}{\partial \varepsilon} - 1 - \nu\right) \tag{3.20.c}$$

In the case of longitudinal waves that propagate and oscillate in the same direction, relation between ultrasonic wave velocity and stress can be defined with Equation 3.21 where $\partial\sigma$ is stress change from a reference level, L_{22} is acoustoelastic constant (L_{ij}), V_{22} is longitudinal wave velocity, and V_{22}^{0} is longitudinal wave velocity at axial zero stress.

$$\frac{\partial V_{22}/V_{22}^{0}}{\partial \sigma} = L_{22} \tag{3.21}$$

3.7. FINITE ELEMENT MODELING

Engineering problems are modeled mathematically in terms of differential equations with corresponding boundary and initial conditions. In order to derive these differential equations, fundamental laws are applied to obtain balance of mass, force and energy in a control volume. Analytical solutions are composed of a homogeneous and a particular part. Homogeneous part of the solution contains information about the natural behavior of a given system such as modulus of elasticity, thermal conductivity, and viscosity. The parameters that cause disturbance such as external forces, moments, temperature difference across a medium, and pressure difference appear in the particular part of the solution.

Analytical models cannot be applied to most of the engineering problems. Dealing with exact analytical solutions are prevented by complex differential equations, difficult physical shape, and difficulties caused by the boundary and initial conditions. In order to deal with these problems numerical methods such as finite difference method and finite element method are used. These numerical methods divide the medium into small parts with discrete points called nodes and approximate the exact solution on these nodes. The nodes in a system are connected together with elements. Finite difference method cannot be applied to the problems with complex geometry and complex boundary conditions. On the other hand finite element method brings approximate results at any point of a system with complex geometry.

Integral formulations are used in finite element method and process results in a set of simultaneous algebraic equations. A field quantity is interpolated by using the field quantity values at nodes over an element. Connecting the elements together bring the field quantity over the entire system.

Various types of engineering problems such as solid mechanics, heat transfer, fluid flow, and electrical network can be solved by using finite element method. The modern finite element method is born in early 1900s by modeling elastic continua using discrete equivalent elastic bars [176]. In 1943, the mathematician Courant investigated a torsion problem by describing a piecewise polynomial solution over triangular sub regions and mentioned as the first person developed finite element method [177]. In the 1950s, aircraft industry applied this method to analyses of delta wings. In the 1960, finite element term became popular by Clough. By 1963 the method is applied to other areas in engineering such as heat transfer, groundwater flow, and magnetic fields. The first book about finite element method is published by Zienkiewicz and Cheung in 1967 [178]. The finite element software ANSYS is released in 1971 [179]. In the 1980s by the development of microcomputers the software is available for this platform.

Various commercial finite element software packages are available that operates on microcomputers and workstations. Most of these computer programs have the ability of static stress analysis, structural dynamics, vibration, and heat transfer and are equipped with library of elements. Development in microcomputer technology influenced the finite element software packages. Today most of these computer programs are easy to use and does not require to study the theory of finite element method. One of the most widely used finite element computer software is ANSYS which is comprehensive and contains over 100,000 lines of code. ANSYS have the capability of programming static, dynamic, heat transfer, fluid flow, and electromagnetism analyses. It consists of Graphical User Interface (GUI), pull down menus, dialog boxes, and a tool bar. Analysis of large structural systems can be performed in such engineering fields, including aerospace, automotive, electronics, and nuclear. Examples of other commercial FEM software packages are SDRC/I-DEAS, NASTRAN, ABAQUS, COSMOS, ALGOR, PATRAN, Hyper Mesh, and Dyna-3D.

3.7.1. Finite Element Thermal Analysis

Welding is a process that itself cannot be modeled by a finite element method. However, the main effect of welding on the material can be considered the heat effect. The heat during welding changes the material properties as they are all temperature dependent. In order to model a complicated process such as welding, in this work we modeled this processes solely in terms of temperature dependent material properties upon application of heat and subsequent cooling in a controlled way. The stresses caused by this temperature change is modeled and compared with experimental measured data.

On the basis of stress analysis, thermal analysis is the calculation of temperatures within a solid body and determination of heat flux fields in a system. The three modes of heat transfer are conduction, convection, and radiation. Conduction refers to the heat flow from high temperature region to low temperature region by molecular activities [180]. Two dimensional rate of heat transfer is given by Fourier’s Law:

$$q_x = -kA\frac{\partial T}{\partial x} \tag{3.22.a}$$

$$q_y = -kA\frac{\partial T}{\partial y} \tag{3.22.b}$$

$$q_z = -kA\frac{\partial T}{\partial z} \tag{3.22.c}$$

where q_x, q_y and q_y are x, y, and z are the components of heat transfer rate, k is the thermal conductivity of medium, A is the cross sectional area of medium, and T is the temperature. It should be mentioned that the total heat flow is always perpendicular to the isotherms which are constant temperature lines or surfaces as illustrated in the Figure 3.15.

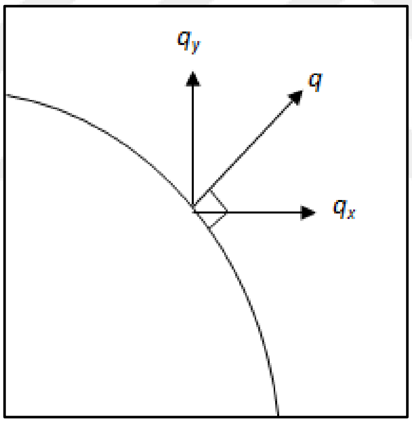

Figure 3.15. Total heat flow perpendicular to the isotherms

According to the Newton’s Law of Cooling, the overall heat transfer rate between a fluid and the surface which is in contact with the fluid is given by the Equation 3.23.

$$q = hA(T_s - T_f) \tag{3.23}$$

where h is the heat transfer coefficient, T_s is the temperature of the surface and T_f is the temperature of the fluid. The amount of energy emitted from the surface by radiation is determined by the Equation 3.24.

$$q'' = \epsilon \delta T_s^4 \tag{3.24}$$

where q'' is the rate of themal energy emitted by the surface, ϵ is the emissivity of the surface, and δ is the Stefan-Boltzman constant.

According to the principle of conservation of energy the rate of energy that enters to the system minus rate of energy that leaves the system plus the rate of energy generated in the system must be equal to the energy stored in the system.

$$U_{in} - U_{out} + U_{generated} = U_{stored} \tag{3.25}$$

where U_{in} is the amount of entered energy, U_{out} is the amount of leaved energy, $U_{generated}$ is the amount of generated energy, and U_{stored} is the amount of energy stored.

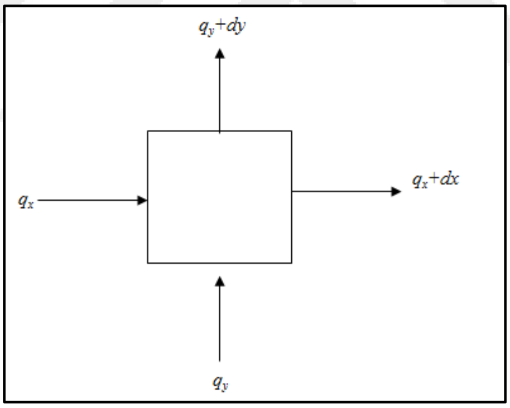

Figure 3.16. Schematic representation of the conversation of energy principle

When the conversation of energy principle is applied a small region illustrated in Figure 3.26 and after a derivation process, the equation of heat conduction with respect to time is obtained.

$$k_x \frac{\partial^2 T}{\partial x^2} + k_y \frac{\partial^2 T}{\partial y^2} + k_z \frac{\partial^2 T}{\partial z^2} + q' = \rho C p \frac{\partial T}{\partial t} \tag{3.26}$$

where q' represents the heat generation per unit volume, ρ is the density, *Cp* is the specific heat, *k* is the thermal conductivity, and *t* is the time.

3.7.2. Finite Element Structural Analysis

Stresses are defined as internal forces created by applying external forces to the boundaries of the material. The equilibrium conditions for three dimensional stresses are determined by the formulas given in Equation 3.27.

$$\frac{\partial\sigma_{xx}}{\partial x}+\frac{\partial\tau_{xy}}{\partial y}+\frac{\partial\tau_{xz}}{\partial z}+f_x=0 \tag{3.27.a}$$

$$\frac{\partial\tau_{xy}}{\partial x}+\frac{\partial\sigma_{yy}}{\partial y}+\frac{\partial\tau_{yz}}{\partial z}+f_y=0 \tag{3.27.b}$$

$$\frac{\partial\tau_{xz}}{\partial x}+\frac{\partial\tau_{yz}}{\partial y}+\frac{\partial\sigma_{zz}}{\partial z}+f_z=0 \tag{3.27.c}$$

where σ is the stress with x, y, and z components, τ is the shear stress with xy, xz, and yz components. $f_{x,y,z}$ are body forces acting in principal directions. Components of principal stress are defined as

$$\sigma_x=\frac{E}{(1+v)(1-2v)}\left[(1-v)\varepsilon_x+v\varepsilon_y+v\varepsilon_z\right] \tag{3.28.a}$$

$$\sigma_x=\frac{E}{(1+v)(1-2v)}\left[v\varepsilon_x+(1-v)\varepsilon_y+v\varepsilon_z\right] \tag{3.28.b}$$

$$\sigma_x=\frac{E}{(1+v)(1-2v)}\left[v\varepsilon_x+v\varepsilon_y+(1-v)\varepsilon_z\right] \tag{3.28.c}$$

where E is the modulus of elasticity, v is Poisson’s ratio for the material. The stress-strain relations can be written in matrix for as given in Equations 3.29 and 3.30 where γ is the shear strain.

$$\begin{Bmatrix} \sigma_{xx} \\ \sigma_{yy} \\ \sigma_{zz} \\ \tau_{xy} \\ \tau_{yz} \\ \tau_{xz} \end{Bmatrix} = \frac{E}{(1+v)(1-2v)} \begin{bmatrix} 1-v & v & v & 0 & 0 & 0 \\ v & 1-v & v & 0 & 0 & 0 \\ v & v & 1-v & 0 & 0 & 0 \\ 0 & 0 & 0 & (1-2v)/2 & 0 & 0 \\ 0 & 0 & 0 & 0 & (1-2v)/2 & 0 \\ 0 & 0 & 0 & 0 & 0 & (1-2v)/2 \end{bmatrix} \begin{Bmatrix} \varepsilon_x \\ \varepsilon_y \\ \varepsilon_y \\ \gamma_{xy} \\ \gamma_{yz} \\ \gamma_{xz} \end{Bmatrix} \tag{3.29}$$

or

$$\{\sigma\} = [D]\{\varepsilon\} \tag{3.30}$$

Finally stresses due to thermal changes in the material can be explained by the formula given in Equations 3.31 and 3.32.

$$\{\sigma\} = [D]\{\varepsilon\} - \{\varepsilon^{th}\} \tag{3.31}$$

and

$$\{\varepsilon^{th}\} = \begin{Bmatrix} \alpha_x \\ \alpha_y \\ \alpha_z \end{Bmatrix} dT \tag{3.32}$$

where ε^{th} is the thermal strain, α is thermal expansion coefficient and dT is the variation of temperature from the reference temeperature.

3.7.3. Heat Source Model

Simulation of submerged arc welding is a complicated process. Dust particles are being injected during the application of weld beam. That dust surrounds the weld arc and the formed weld beam. This mechanism should be considered for accurate prediction of heat flow and residual stress.

Several heat source models are considered to model the welding process. Hibbitt and Marcal used a surface heat model to develop a numerical model for welding process [103]. Andersson applied a surface heat input to investigate thermal stresses in submerged-arc welded joints [104]. Effect of ramped heat model is investigated by Y. Shim *et al* [181]. Gaussian surface heat distribution is used by Nickell [105] and Friedman [106] in their studies. In order to obtain a more detailed model of heat source, studies on Gaussian heat source continued by various authors [182-187]. Goldak et al proposed a double ellipsoidal model that models heat distribution in an ellipsoidal geometry [188] as illustrated in Figure 3.17.

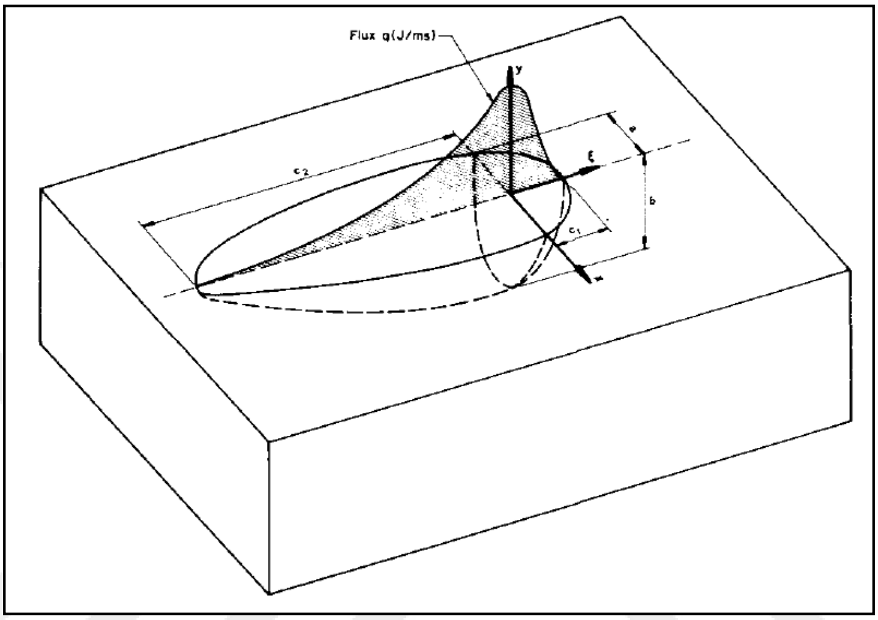

Figure 3.17. Double ellipsoid heat source configuration together with the power distribution function along the z axis [188]

Goldak’s model is capable of modeling heat input of most of the welding types. However, double ellipsoidal shape is impossible to be obtained in submerged arc welding process. Dust around the weld arc prevents the formation of double ellipsoidal shape. Therefore, an ellipsoidal heat source model is used.

Pavelic *et al.* proposed the disc model with thermal flux of a Gaussian or normal distribution as illustrated in Figure 3.18 [189]. In this model $q(r)$ is surface flux at radius r (W/m^2), $q(0)$ is maximum flux at the center of the heat source (W/m^2), C is concentration coefficient (m^{-2}), and r is radial distance from the center of the heat source (m).

$$q(r) = q(0)\, e^{-Cr^2} \tag{3.33}$$

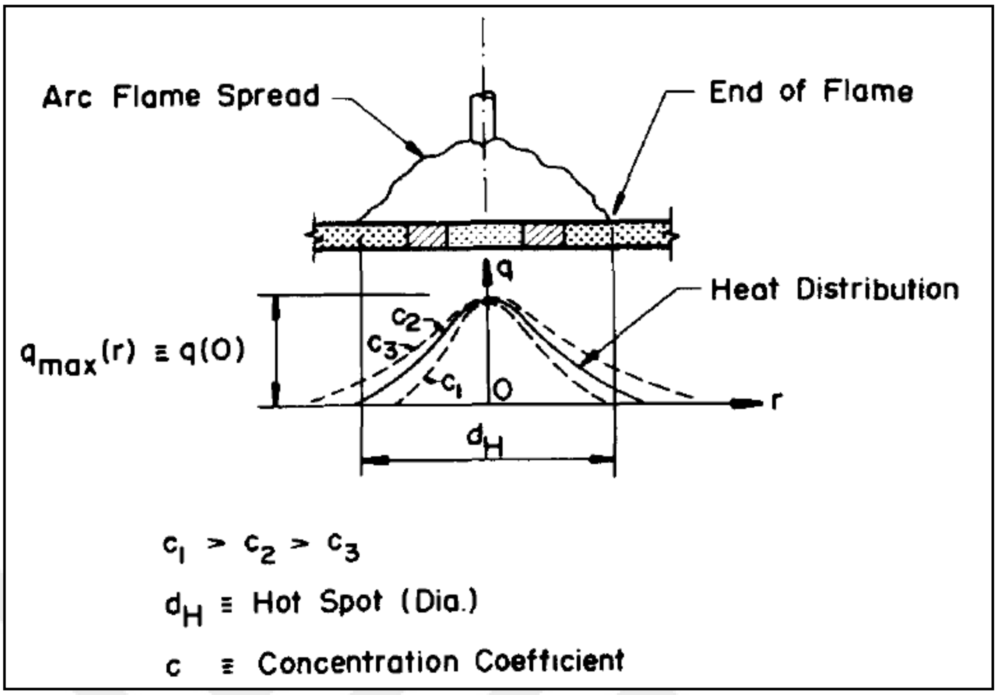

Figure 3.18. Circular disc heat source [189]

Surface heat source model is effective where the depth is small. However, high density power sources transport welding heat below the surface and this effect cannot be modeled by a surface heat source model. Power density distribution for a hemispherical volume source can be modeled as given in Equation 34.

$$q(x,y,z) = \frac{6\sqrt{3}Q}{c^3\pi\sqrt{\pi}} e^{-3\left(\frac{x-x_i}{c}\right)^2} e^{-3\left(\frac{y-y_i}{c}\right)^2} e^{-3\left(\frac{z-z_i}{c}\right)^2} \tag{3.34}$$

In this model $q(x,y,z)$ is the power density (W/m^3), Q is the weld heat input (J/m), x_i, y_i, and z_i are central coordinates of heat source (m), x, y, and z are central coordinates of power density point (m), and c is the radius of the sphere (m).

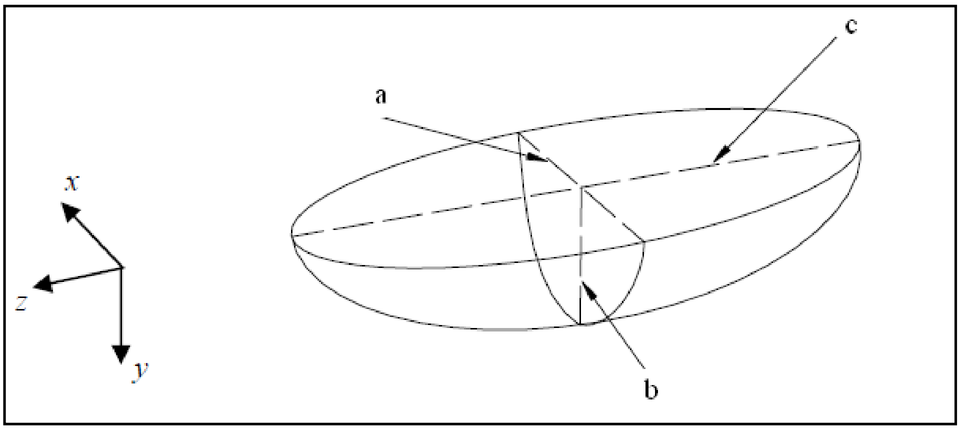

Figure 3.19. Illustration of ellipsoidal heat distribution

In the ellipsoidal power density distribution, axes of the ellipsoidal is determined as a, b, and c in directions of x, y and z as illustrated in Figure 3.19. Heat source moves along z direction, b represents the depth of ellipsoidal heat source and a and c are dimensions along the surface of the source [104].

$$q(x,y,z) = \frac{6\sqrt{3}Q}{(abc)\pi\sqrt{\pi}} e^{-3\left(\frac{x-x_i}{a}\right)^2} e^{-3\left(\frac{y-y_i}{b}\right)^2} e^{-3\left(\frac{z-z_i}{c}\right)^2} \tag{3.35}$$

3.7.4. Thermal Structural Coupled Analysis

Finite element analysis is carried out using ANSYS. Geometry of the sample is sketched by CAD tools of ANSYS software. Because all samples with different carbon content have the same geometry, same sketch is used to analyze all steel types. In this 3 dimensional analysis, a full geometry model of the sample is used in spite of a half symmetric model.

In order to realistically simulate the welding process, weld beam is modeled with overflown melted beam. First part of the sketch is upper part of weld beam which is overflown melted metal from weld groove. It has a curved shape with maximum thickness of 1 mm. Main part of weld beam is sketched under this which is the weld beam that fully filled with weld filler metal. These two parts are modeled with the same material properties of filler metal.

Base metal for three types of steels is modeled with the same geometry. This model is composed of two parts. First part is placed under the weld beam that accommodates weld groove. This small part of base metal is created in order to be meshed with higher element density, because this part accommodates adjacent regions of heat source. Remaining parts of the base metal modeled around the initial geometry. 3-dimensional finite element geometry is illustrated in Figure 3.20.

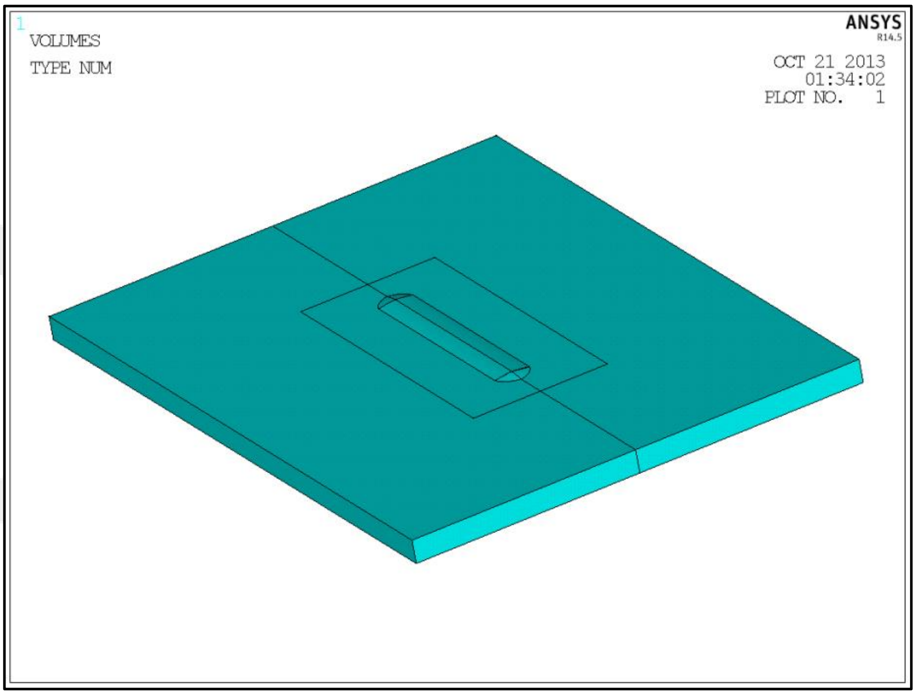

Figure 3.20. 3-dimensional illustration of the finite element model

SOLID 185

Thermal structural coupled analysis is composed of two separate analyses which should be performed consecutively. Accordingly in this study two different elements are used for thermal and structural analyses. SOLID70 is the selected element for thermal analysis. This element is capable of 3-dimensional thermal conduction. It has eight nodes with a single degree of freedom which is temperature. In this study 3-dimensional transient thermal analysis is performed. Geometry of SOLID70 element is illustrated in Figure 3.21.

Structural analysis is performed with SOLID185 element which is structural equivalent of SOLID70 element. This element is able to perform 3-dimensional modeling of solid structures. It has eight nodes with three degree of freedom which are translations in the nodal x, y, and z directions. It has the same geometry with SOLID70 element which is shown in Figure 3.21.

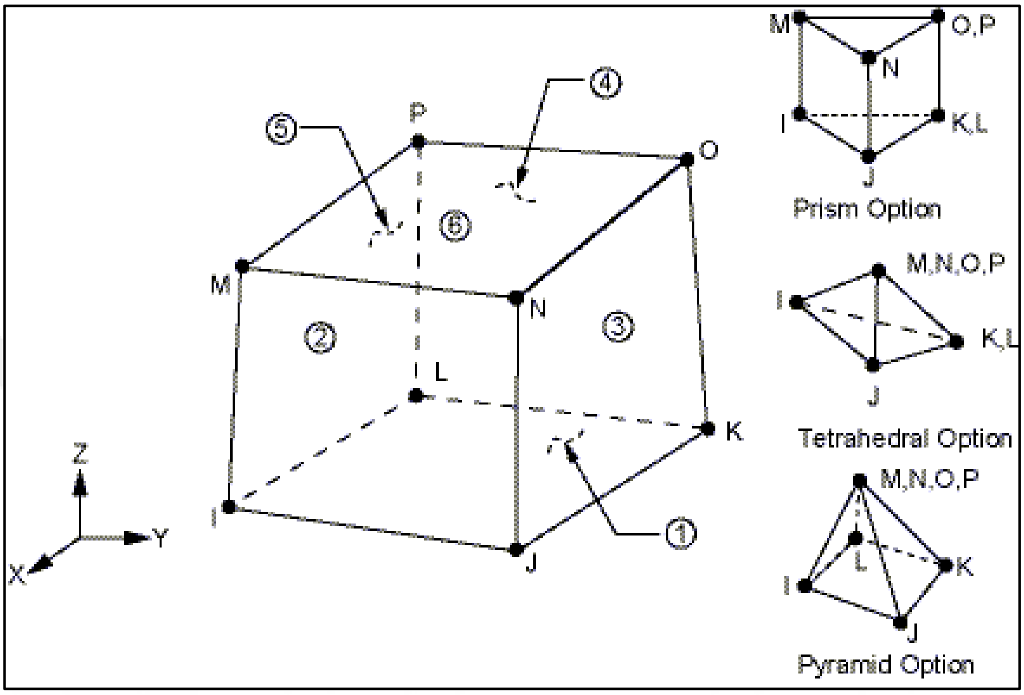

Figure 3.21. Illustration of SOLID70 and SOLID185 elements and its optional geometries [179]

Sketch of the finite element model is meshed with tetrahedral and brick geometries of selected elements. Curved structure of the weld beam prevented using brick geometry of the element, therefore weld beam and base metal around the weld beam is meshed with tetrahedral geometry. Cubic geometry is used to mesh are outer part of the base metal.

Finite element mesh density of the specimen is higher inside and around the weld beam and it is being reduced in the outer parts of the specimen as illustrated in Figure 3.22. Upper and lower parts of weld beam are meshed with 6531 tetrahedral elements. First part of the weld beam which is located under the weld beam and contains weld groove has 31493 tetrahedral elements. Remaining parts of base metal meshed using 3912 cubic elements.

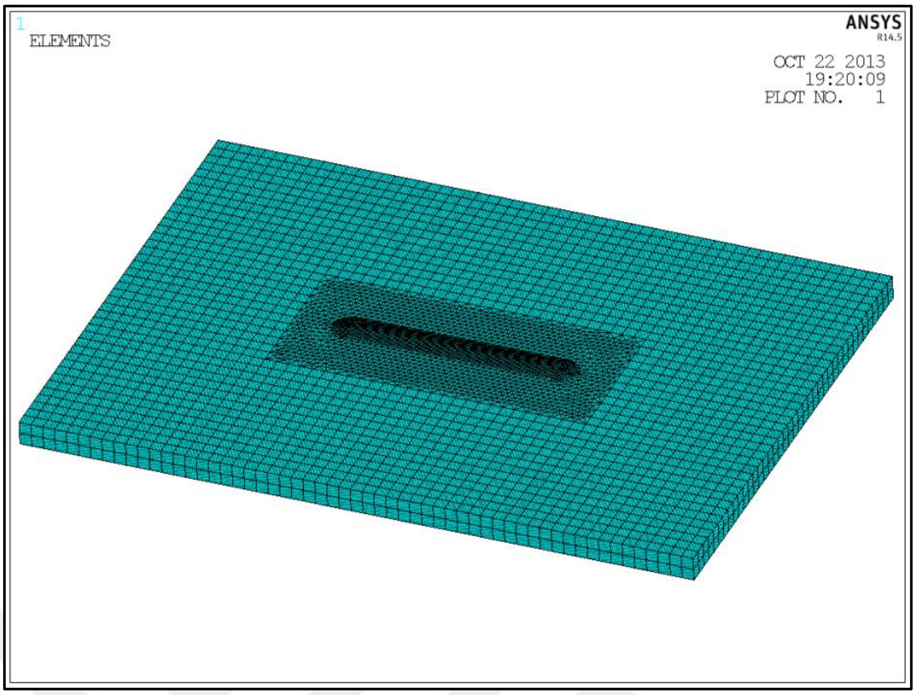

Figure 3.22. Illustration of the finite element mesh

In order to perform an accurate analysis it is required to have a model with high mesh density. However, increasing mesh density, increases computation time. In this study, three types of steel are analyzed using the generated finite element model. In order to obtain optimum mesh density, temperature change with respect to mesh density is recorded. For a given amount of heat input, increasing mesh density increases the total heat input which is correlated to temperature increase. Temperature increase upon mesh density increase levels off at a certain mesh density which is chosen to be the optimum for the analysis.

Submerged arc welding is a high power density process that requires modeling of heat transport below the surface. Accordingly an ellipsoidal model with circular face is generated. According to weld bead profile measurements, semi axes a, b, and c are determined as given in Table 3.5.

Weld arc is the heat source in welding process. Finite element analysis of welding process requires accurate determination of weld heat input which is related to welding parameters. Weld heat input is calculated using Equation 3.36 in terms of joules per millimeter. In this equation Q is the weld heat input (J/m), η is the weld efficiency, V is the voltage (W/A) and I is current (A).

$$Q = \eta \, V \, I \tag{3.36}$$

Table 3.5. Heat source parameters

Semi-axe	**Length (mm)**
Width of heat source (a)	7.7
Height of heat source (b)	3.0
Length of ellipsoidal (c)	7.7

HGEN subroutine in ANSYS is used to apply the body heat. Subroutine initially calculates the position of weld torch according to weld time and then determines coordinate of each node in the selected volume according to the position of weld torch which is located at the central coordinates of power density point. The power density at each node is calculated by using the ellipsoidal power density distribution equation and applied as heat generation.

The thermal properties of the weld metal and parent plates are used with most possible wide temperature range of available data because temperature during the welding may locally reach 3000 ^{o}C or more. In the thermal analysis, required material properties are thermal conductivity and specific heat capacity which are provided from the database of MPDB software [190] and given in Appendix A**.**

Heat is lost during the solidification of weld pool because of radiation and convection. Accordingly, radiation and convection heat losses are modeled in the finite element model. It is assumed that radiation and convection coefficients are independent of temperature. The same value is used in weld metal and parent plates. Most common values of radiation and convection coefficients of steel are taken from the literature. The value of convection coefficient at room temperature is 5.7 W/m^{2}K. Radiation coefficient is determined to be 0.75. These are constant values independent of temperature. The same coefficients are used for weld beam and all of the base plates. Temperature of the surrounding is set to 293 K.

Radiation and convection are allowed in the outer area that cover weld beam and base metal. These areas are determined as radiation and convection boundary conditions in the finite element model.

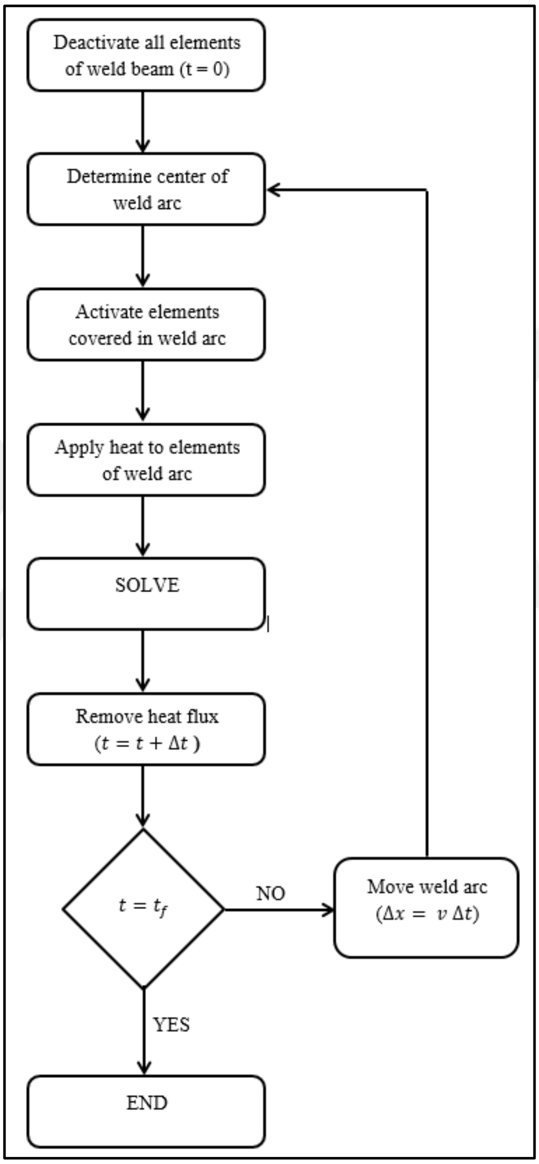

Figure 3.23. Flow chart of moving heat source algorithm (t is time, t_f is final time, Δt is time step)

Thermal analysis is composed of two steps. Application of heat source with moving heat source is modeled in the first stage. Movement of weld arc is simulated by using element death and birth technique. Flow chart of moving heat source algorithm is given in Figure 3.24. Initially all elements in the weld beam is deactivated and coordinates of starting position of weld arc determined. Deactivation is performed by multiplying their stiffness to a sufficiently small factor which is 10^{-6}. Elements in the volume of weld arc are activated and heat is applied to that volume during the determined time interval. The shorter the time interval is, the more accurate are the results. Then, time is stopped, application of heat ended and weld arc is moved to the next position. New position is calculated according to welding speed and time step. The process continues by activating elements until the final position of weld beam. Figure 3.25 illustrates moving heat source. The cooling down of the specimen to steady state is performed in the proceeding second stage of thermal analysis.

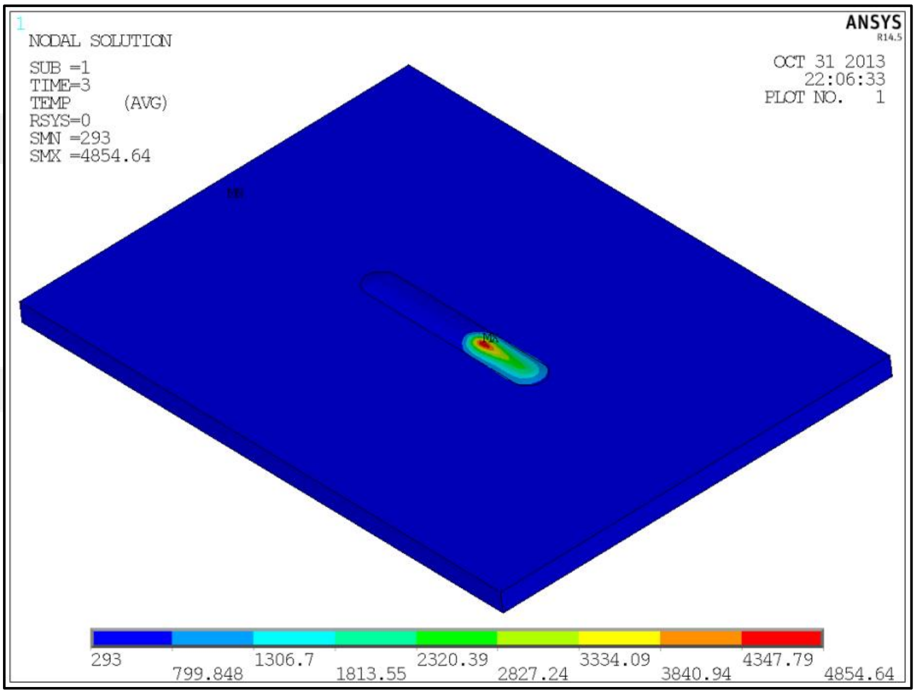

Figure 3.24. Illustration of moving heat source 3 seconds after the start of weld

Temperature dependent mechanical properties of weld metal and parent plates are obtained from the same source as thermal properties. Temperature dependent material properties limited to high temperatures could be obtained from the data sources. During welding materials can reach up to vaporization temperatures. At these high temperatures, material has no resistance to deformation. Therefore, Young's Modulus (E) has no effect on formation of residual stress. In addition, mechanical properties are not reliable at high temperatures. In this study, temperature dependent properties which are Poisson's ratio, density, thermal expansion coefficient, modulus of elasticity and yield strength are provided from the database of MPDB software [190] and given in Appendix A.

Boundary conditions are determined in order to allow a stable solution. Displacements are applied to four key points located at the center of the plate parallel to weld beam. Key points are illustrated in Figure 3.25. UX movement is restricted at all four key points. Key points 3 and 4 prevent the model from moving in Z direction. Displacements in Y direction are applied to key points 1 and 4. These key points prevent movement of the plate without any effect on structural analysis.

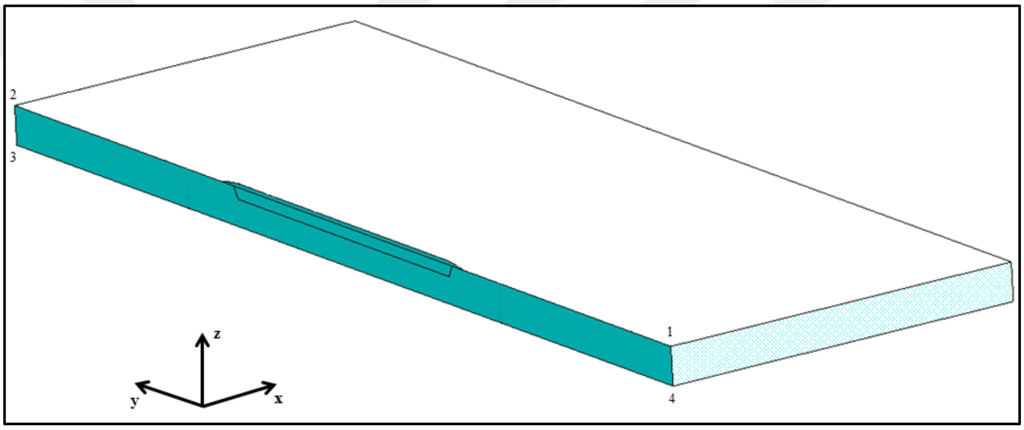

Figure 3.25. Illustration of key points

Same finite element mesh is used with SOLID185 element in the mechanical analysis. Nodal temperatures from thermal analysis are used. Number of steps in mechanical analysis is equal to that of thermal analysis. Temperature history is applied as thermal load during the mechanical analysis. Stresses at each step is calculated and transferred to the next step as initial condition. At the end of cooling period, residual stresses remain in the sample.

The isotropic hardening model is based on the assumption that the yield surface maintains its shape, center, and orientation, but it can expand or contract uniformly about its center in the stress space as yielding occurs while the yield surface does not change its shape, size, or orientation, but rather its center as the yield surface translates in stress space in the kinematic hardening model [189]. In the studies of J. J. Xu *et. al.* [132] and O. Muransky *et. al.* [191], authors discussed the effect of plastic theory. In these studies, results state that kinematic hardening model generally provides more accurate results than isotropic hardening model. According to these results, in this study bilinear kinematic hardening model is used. Types of hardening rules are illustrated in Figure 3.26. In the isotropic model, the yield surface expands with the plastic strain and the yield surface translates with the plastic strain.

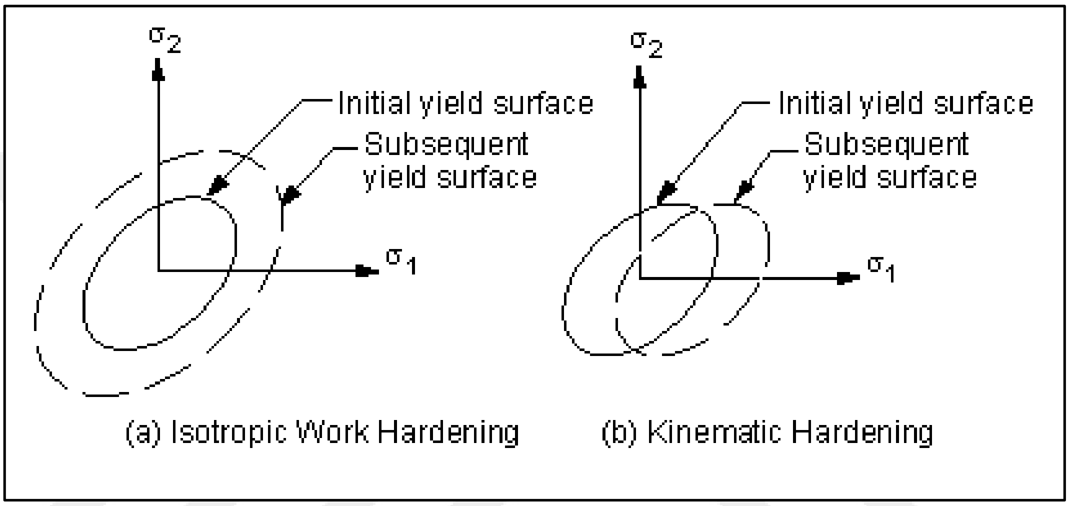

Figure 3.26. Types of hardening rules [179]

Possible extreme values of the normal stresses in a material are defined as principal stresses. There are two types of principal stresses, planer and three dimensional principal stresses. Calculation of first principal stress for two dimensional cases is given in Equation 3.50 where σ_1 and σ_2 are first and second principal stresses, σ_x and σ_y are normal stresses and τ_{xy} is shear stress in xy plane.

$$\sigma_{1,2} = \frac{\sigma_x + \sigma_y}{2} \mp \sqrt{\left(\frac{\sigma_x + \sigma_y}{2}\right) + \tau_{xy}^2} \tag{3.37}$$

In three dimensions, calculation of principal stresses is more complicated. Principal stresses in three dimensions can be calculated using equations given below. In these Equations I_1, I_2 and $I_3$are stress invariants determined in terms of normal and shear stresses.

$$I_1 = \sigma_x + \sigma_y + \sigma_z \tag{3.38.a}$$

$$I_2 = \sigma_x\sigma_y + \sigma_y\sigma_z + \sigma_z\sigma_x - \tau_{xy}^2 - \tau_{yz}^2 - \tau_{zx}^2 \tag{3.38.b}$$

$$I_3 = \sigma_x\sigma_y\sigma_z - \sigma_x\tau_{yz}^2 - \sigma_y\tau_{zx}^2 - \sigma_z\tau_{xy}^2 + 2\tau_{xy}\tau_{yz}\tau_{zx} \tag{3.38.c}$$

$$\emptyset = \frac{1}{3}\cos^{-1}\left(\frac{2I_1^3 - 9I_1I_2 + 27I_3}{2(I_1^2 - 3I_2)^{3/2}}\right) \tag{3.39}$$

$$\sigma_1 = \frac{I_1}{3} + \frac{2}{3}\left(\sqrt{I_1^2 + 3I_2}\right)\cos\emptyset \tag{3.40.a}$$

$$\sigma_2 = \frac{I_1}{3} + \frac{2}{3}\left(\sqrt{I_1^2 + 3I_2}\right)\cos\left(\emptyset + \frac{2\pi}{3}\right) \tag{3.40.b}$$

$$\sigma_3 = \frac{I_1}{3} + \frac{2}{3}\left(\sqrt{I_1^2 + 3I_2}\right)\cos\left(\emptyset + \frac{4\pi}{3}\right) \tag{3.40.c}$$

Equivalent stress is a scalar value that summarizes multidirectional stresses which into an equivalent one. Three dimensional solids have six stress components which are built up in many directions. A single equivalent stress is the combination of the six stress components. Equation 3.54 represents how equivalent stress in terms of principal stresses.

$$\sigma_v = \sqrt{\frac{1}{2}[(\sigma_1 - \sigma_2)^2 + (\sigma_1 - \sigma_3)^2 + (\sigma_2 - \sigma_3)^2]} \tag{3.41}$$

4. RESULTS AND DISCUSSION

4.1. ANNEALING, HARDNESS AND METALLOGRAPHY

During the manufacture and weld chamfer opening processes, residual strains are formed in the steel samples. In order to determine residual stresses formed during the welding process, it is vital to remove remaining stresses from the materials. This is accomplished by full annealing process at a range of temperatures from 150 ^{o}C to 1150 ^{o}C. Small samples of each plate are prepared and full annealed in order to determine the optimum temperature of full annealing.

The aim of annealing process in this study is to obtain stress free materials with minimum loss of strength. Relation between annealing temperature and hardness of the materials allows us to determine stages of annealing process. Theoretically, it is known that annealing process have three stages. In the first stage hardness remain almost constant. This is followed by a sharp decrease in hardness which is the recrystallization stage where all stressed grains are removed and new stress free grains are formed. After this stage, grain growth starts and hardness of the material remains constant during this period. If the temperature of annealing process is further increased, material deteriorates which results in a rapid decrease in hardness. In this study, the region where annealing remains constant is observed and annealing temperature is determined within that range.

Annealing process is performed with a temperature step size of 50 ^{o}C. Step size is decreased to 25 ^{o}C at some critical regions where recrystallization stage is expected to be observed. Hardness of each sample was measured before and after the annealing. This allows the determination of variation in hardness. Before measurement of hardness, each sample is grinded and polished. 10 measurements are performed on polished surfaces to determine hardness of a sample. Average hardness of each sample before annealing process is given in Figure 4.1.

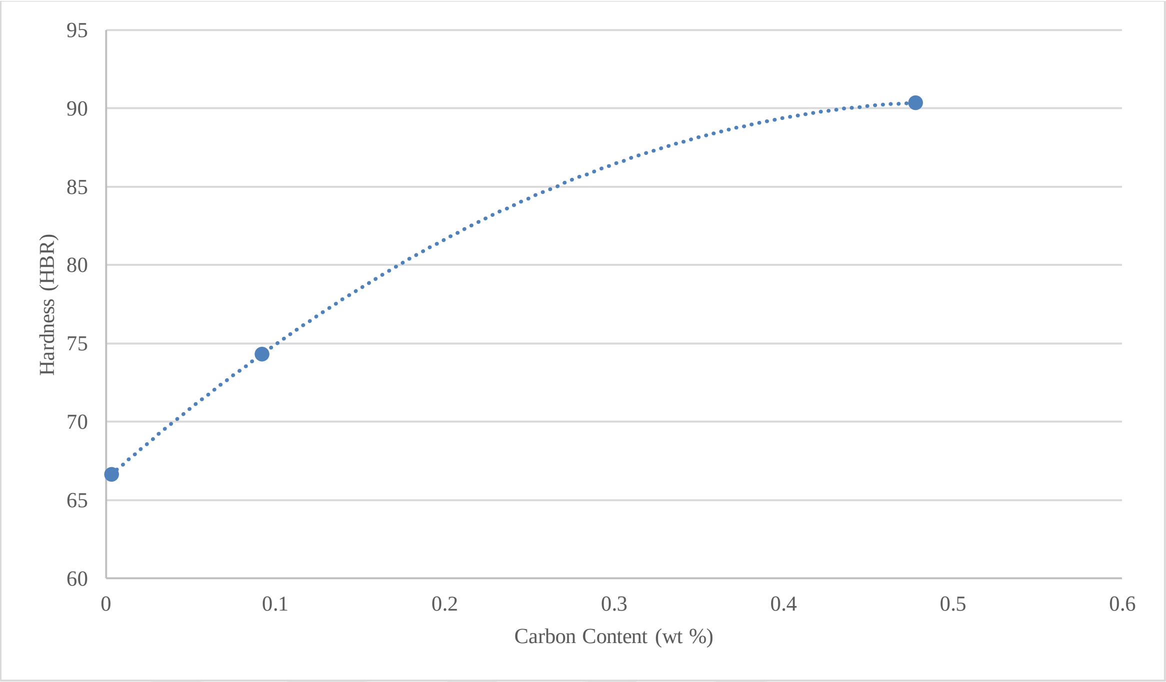

Figure 4.1. Relation between hardness and carbon content of steel samples

Hardness measurements after annealing repeated 10 times for each sample. Ratio of standard deviation to average hardness value ranged between 0.5 to 2 %. Results of hardness measurements after each annealing stage are given in Figure 4.2. Stages of annealing process cannot be clearly seen from this plot. At temperatures lower than 500 °C, hardness slightly increases and after that temperature rapid decrease occurs. After rapid change of hardness at recrystallization stage, decrease levels off at grain growth stage. Further annealing temperatures causes decomposition of material and formation of very large grains which results in rapid decrease in hardness.

Metallographic procedures are applied in order to determine grain size of annealed samples. Optical and scanning electron microscopy is used for imaging of grains. 21 images are obtained for each sample at varying annealing temperatures. Optical microscopy is used for IF steel and low carbon steel while scanning electron microcopy (SEM) is preferred for medium carbon steel. Medium carbon steel have small grains that cannot be imaged by optical microscopy. Accordingly, SEM is used for visualization of grains of medium carbon steel samples.

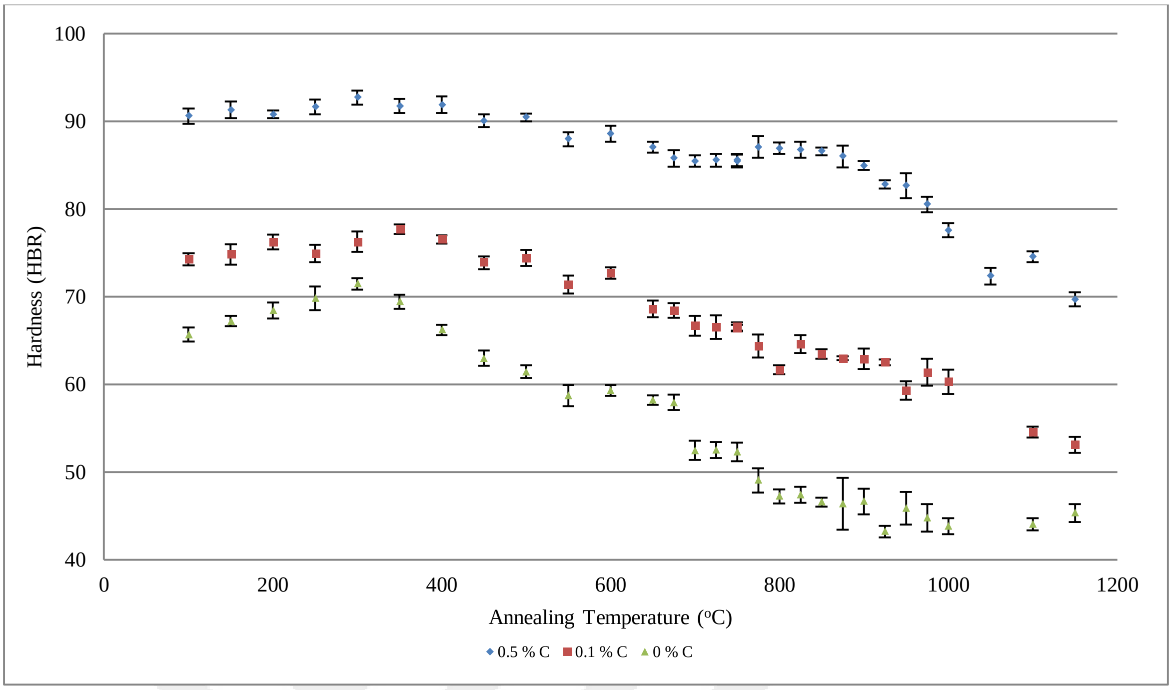

Figure 4.2. Hardness of each sample according to annealing temperature

Metallographic image of each sample have different quality. Different annealing stages brought different image qualities. Some images have homogeneous grain size distribution while others accommodate grains with varying sizes. Metallographic images are used as a complementary data for investigation of annealing stages with hardness test. It is aimed to obtain annealed samples with fine grain distribution.

Initial hardness of each sample can differ from each other. Therefore, variation between initial and final hardness values are used for accurate determination of annealing stages. In this study grain growth stage of annealing process in each material is determined. This stage allowed us to determine safe zone of annealing process. As it is stated before, full annealing should be performed just above the phase boundary of austenite-ferrite and austenite regions. All grains at the end of recrystallization stage are austenitic. This allows us to determine the boundary of two phases. Safe region for grain growth can also be observed from the graphical illustration. Finally, safe annealing temperature between those points is determined using the Equation 4.1. T_a is safe full annealing temperature, T_2 is end temperature of grain growth stage and T_1 is initial temperature of grain growth stage.

$$T_a = T_1 + \frac{2}{3}(T_2 - T_1) \tag{4.1}$$

Figure 4.3 illustrates annealing stages of IF steel as a result of annealing test. Variations between initial and final hardness measurements are used. Images of different annealing stages are also given to illustrate grain sizes. Hardness increases up to 350 ^{o}C and then rapid decrease occurs where recrystallization stage begins. Decrease of hardness continues up to 850 ^{o}C which is the beginning of grain growth stage. This is also the phase boundary of this sample between austenite-ferrite and austenite regions. Observations show that this stage ended at 1000 ^{o}C. After that temperature hardness decrease starts pointing to the decomposition of the material. According to these observations safe annealing temperature for IF-steel is determined as 950 ^{o}C according to Equation 4.1 which is consistent with theoretical phase boundaries for this type of steel. Microscopy imaging after etching also proves the results. At that temperature fine grain distribution with similar size of grains is obtained.

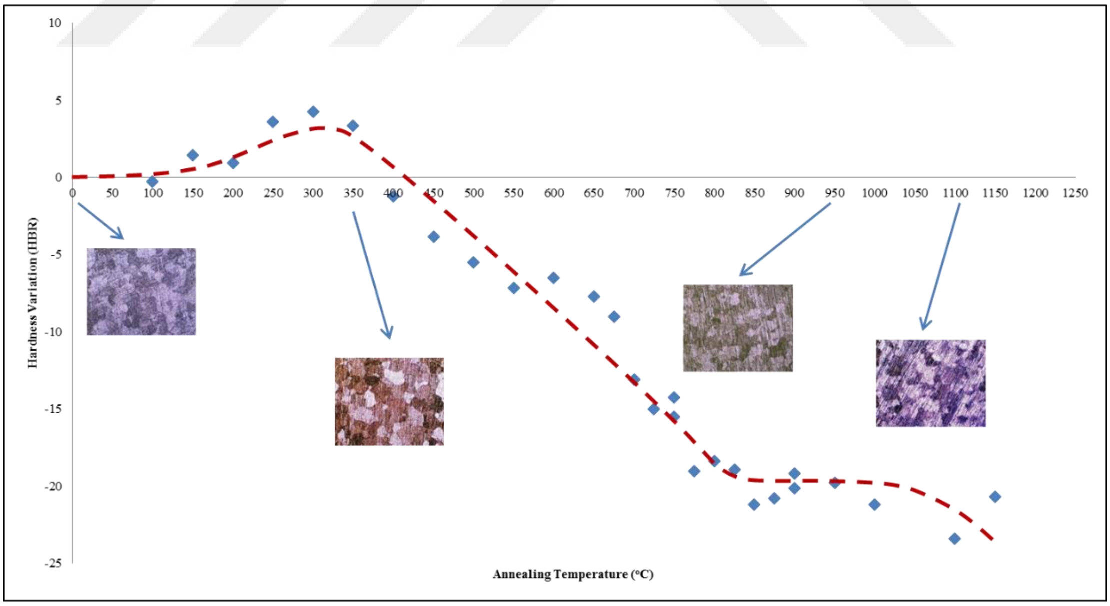

Figure 4.3. Hardness variations and metallographic images of IF steel

Annealing stages of low carbon steel is determined using Figure 4.4. Variations of hardness measurements show that hardness increases up to 400 ^{o}C as a result of annealing process. This increase makes a peak at 300 ^{o}C and reaches to hardness variation of 4.11

HBR. After 500 ^{o}C recrystallization stage starts and hardness decrease ends at 775 ^{o}C. Grain growth stage continues up to 900 ^{o}C and then decomposition of the material starts. According to these observations, safe annealing temperature of low carbon steel is set to 850 ^{o}C. According to metallographic investigations, fine grain distribution with similar grains is obtained at that temperature.

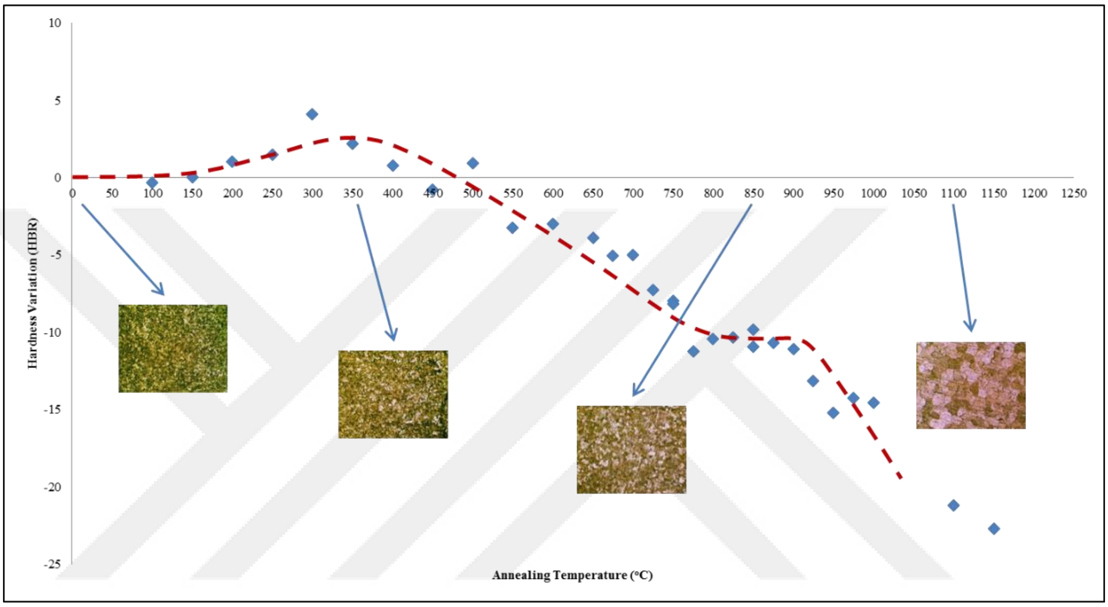

Figure 4.4. Hardness variations and metallographic images of low carbon steel

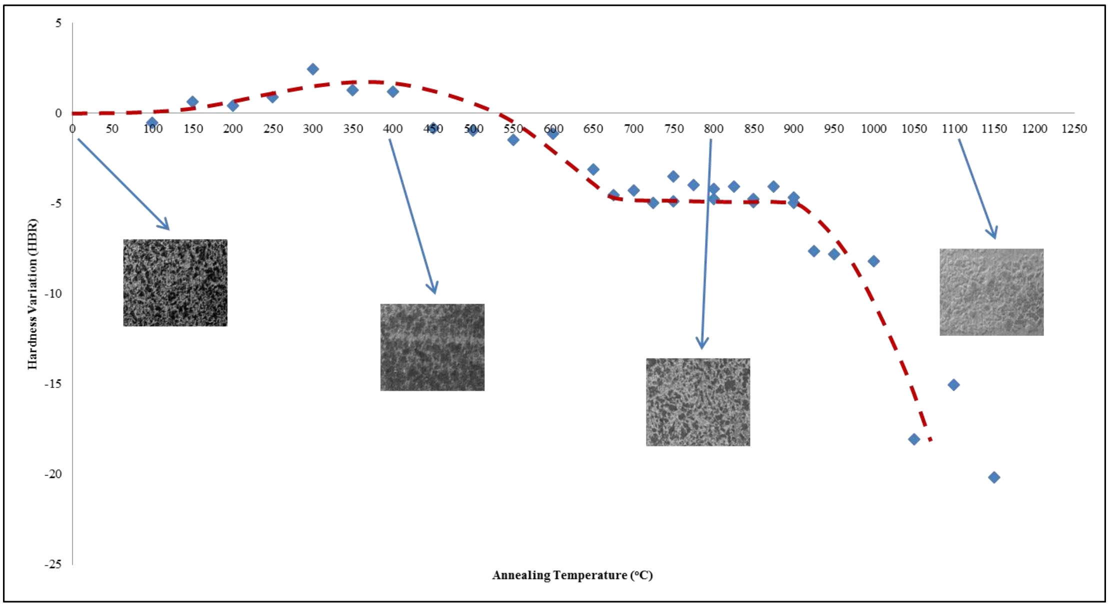

Figure 4.5. Hardness variations and metallographic images of medium carbon steel

Variations of hardness measurements of medium carbon steel are illustrated in Figure 4.5. Similar to low carbon steel hardness increases up to 400 °C as a result of annealing process. In contrast to low carbon steel, increase of hardness does not have a sharp peak and mostly vary about 2 HBR. After 400 °C recrystallization stage starts and hardness decrease ends at 675 °C. Grain growth stage continues up to 900 °C and then decomposition of the material starts. Safe annealing temperature of medium carbon steel is determined as 825 °C. Metallographic investigation results also proved that medium carbon steel which is annealed that temperature have fine grain distribution.

4.2. ACOUSTOELASTIC CONSTANT

Thermal strains are formed as a result of thermal processes. In order to measure residual stress with ultrasonic wave velocities it is necessary to perform a correlation between ultrasonic wave velocity and stress. D. Vang [100] correlated time of flight of ultrasonic waves with mono-axial stress. Accordingly, in this study, relation that expresses thermal stress which is given in Equation 4.3 is used to calculate stress. This equation is originally derived for one dimensional stress and, it is appropriate to be used to correlate our measured stress which is average with ultrasonic sound waves. Relation between ultrasonic wave velocity and average bulk stresses is determined as:

$$\sigma = E \ \alpha_L \ \Delta T \tag{4.2}$$

where σ is the thermal stress, E is the modulus of elasticity, α_L is thermal expansion coefficient, and ΔT is temperature change. By observing the relation between thermal strains and ultrasonic wave velocity, it is possible to determine average residual stresses in materials.

Acoustoelastic constant is determined by using relation between ultrasonic wave velocity variations and stress. Temperature dependent properties, modulus of elasticity and thermal expansion coefficient, of steel plates are used in order to calculate thermal stress. Slope of the plot of velocity variations vs. thermal stress defined the thermally determined acoustoelastic constant as shown in Figures 4.6. Results state that variation in ultrasonic wave velocity is inversely proportional with thermal strain. Thermally determined acoustoelastic constant of IF steel is -0.00017260 MPa^{-1}, low carbon steel is -0.00011164 MPa^{-1}, and medium carbon steel is -0.00007098 MPa^{-1}.

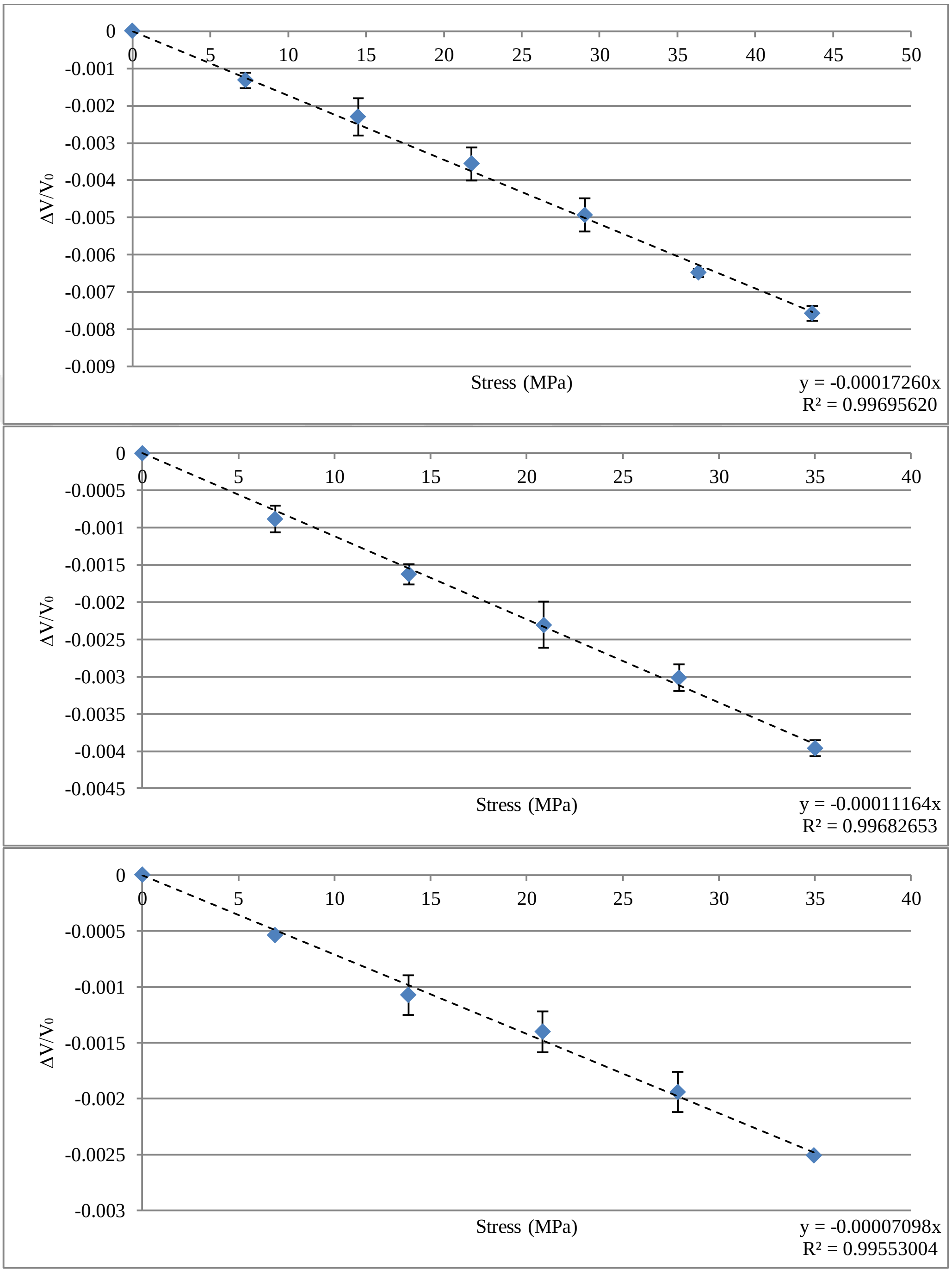

Figure 4.6. Relation between average of ultrasonic wave velocity variations with error bars and stress in three samples of from top to bottom IF, low carbon and medium carbon steels

Thermally determined acoustoelastic constant of IF steel is the lowest value among others. Carbon contents of IF steel, low carbon steel, and medium carbon steel are 0.003 wt %, 0.092 wt %, and 0.478 wt %. Relation between thermally determined acoustoelastic constant and carbon content is illustrated in Figure 4.7. With the increasing carbon content, constant gets a lower value. It can be predicted from this plot that acoustoelastic constant rapidly increases with increase at carbon content up to 0.1 wt %.

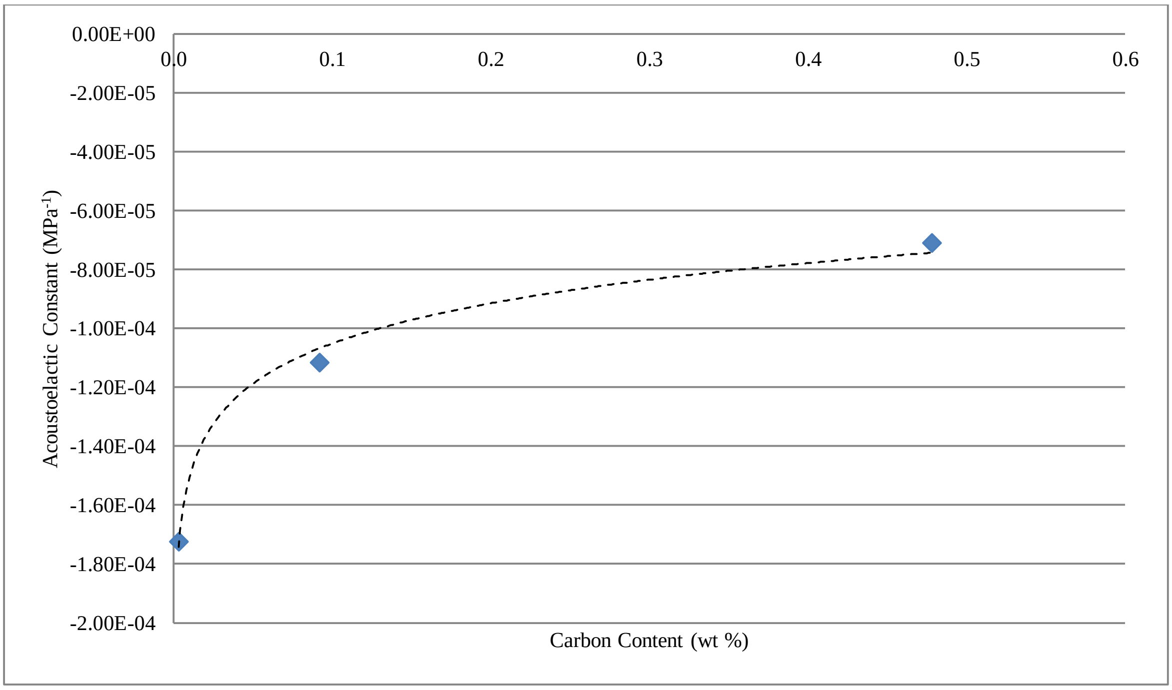

Figure 4.7. Acoustoelastic constant and carbon content

4.3. RESIDUAL STRESS ANALYSIS

Experimental analysis of residual stress with different carbon content is performed using ultrasonic test. Results of experimental analysis are compared with finite element analysis. Experiment results are compared with finite element results in the first part of the analysis. Residual stress variations along the weld beam are compared for each type of steel with experiment and simulation results. The aim of this study is to determine effect of carbon content on formation of residual stress. Accordingly, residual stresses at each measurement line for each type of steel are compared in terms of experiment and finite elements results. Finally, finite element equivalent residual stress distributions at each section of materials are given as contour plots.

Ultrasonic waves travel through the thickness of the material and reflect back to transmitter. Transmitter at that point acts as a receiver and measures the time that passes during the travel of ultrasonic waves. Travel time is directly related to ultrasonic wave speed which can be effected by stresses in the material. During the movement, these waves meet with stressed layers of materials. If the material is thin enough, variation of stress between layers of the material can be neglected. If the material is thick, different stress zones in the material have a complex effect on ultrasonic wave velocity. Moreover, normal stresses and shear stresses have effect on ultrasonic wave velocity through the thickness of the material. Shear stresses and normal stress parallel to wave propagation have a negligible effect on wave velocity in thin materials, but for thick materials they cannot be ignored.

Experimental measurements are performed in immersion ultrasonic system. Ultrasonic wave velocities are measured and residual stresses at each measurement point are calculated. Denser measurements are performed around weld beams along S, M, and E lines. Three welded samples were prepared for each plate and measurements are accomplished in each sample.

It is aimed to perform measurements as close as possible to weld beam center. However, rough shape of weld beam prevents ultrasonic wave velocity measurements inside the weld. Accordingly, distance between measurement points and weld center varies at each measurement line according to weld beam shape. That approach provides a new problem and unexpected results with high deviation of the data trend occurs at points very close to weld beam. In order to prevent this and perform the same experiments, measurements started at 10 mm away from weld center at each measurement line.

Finite element simulation provides normal and shear stresses in the whole of the material. It allows investigation of different sections of the material. Equivalent stresses are determined using that data and average values calculated using 11 data points through the thickness of the material. These average values are compared with the obtained experimental data.

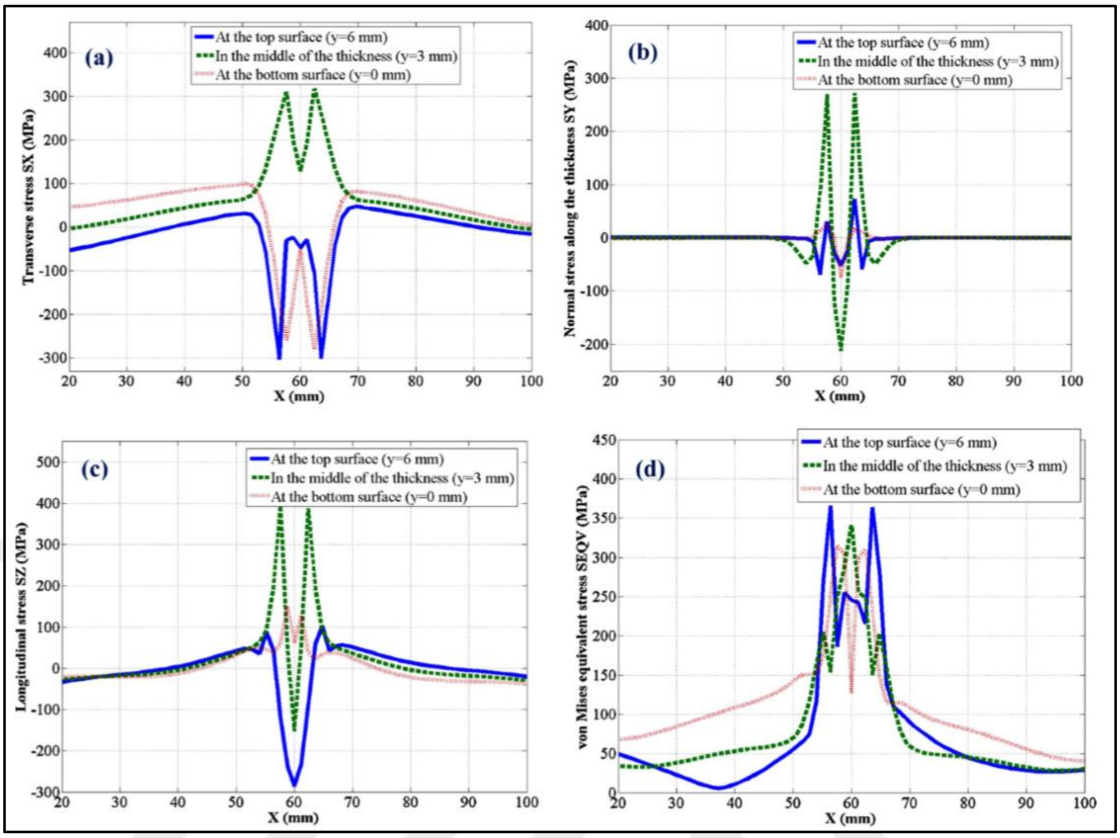

Figure 4.8. Stress distribution transverse across the weld bead at the longitudinally middle section: (a) transverse stress SX, (b) normal stress along the thickness SY, (c) longitudinal stress SZ, and (d) equivalent stress [124]

Kovacevic and his colleagues investigated thermally induced residual stress in hybrid laser welding-GMA welding process [124]. In that study, weld is applied to join two steel plates with 6 mm of thickness in spite of a weld beam on plate as it is in this thesis. More filler metal used in a deeper path. Similar to our study, they used a cylindrical Gaussian profile in order to model the laser beam power. Authors investigated residual stress distributions in terms of principal stresses and equivalent stress within different sections of the material through the thickness of the material. Weld beam distribution is different in both of the studies but results show that in the longitudinally middle section of the weld beam, tensile and compressive principal stresses are formed in different sections through the thickness of the material as illustrated in Figures 4.8 and 4.9. Equivalent stress is positive and starts to increase away from weld center in both of the studies. Stressed regions are narrower in this thesis because ratio of volumes of weld beam and base metal is smaller.

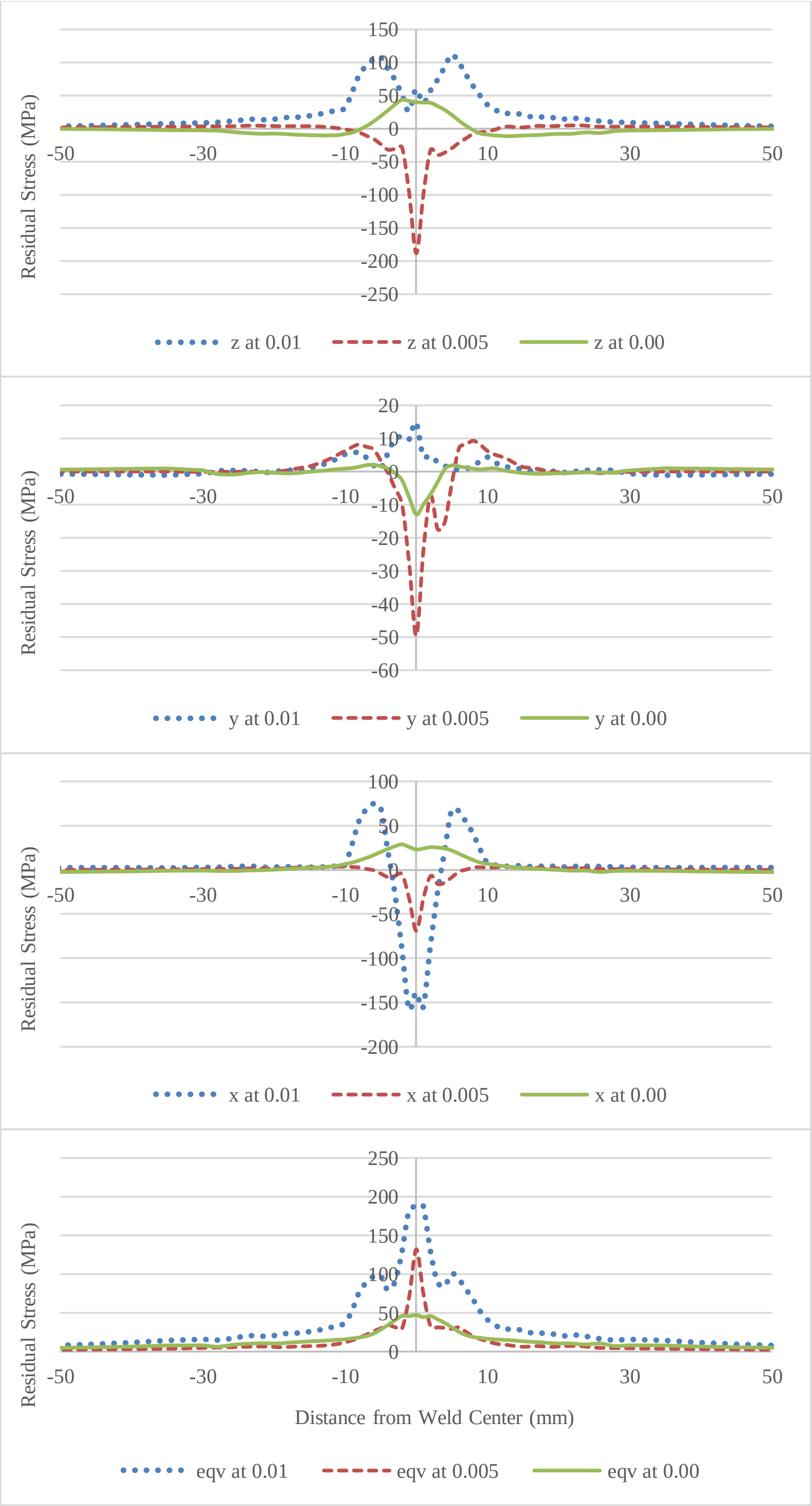

Figure 4.9. Stress distribution transverse across the weld bead at the longitudinally middle section of IF steel: z is transverse stress (σ_z), y is normal stress along the thickness (σ_y), x is longitudinal stress (σ_x), and eqv is equivalent stress

Figures 4.10 to 4.18 illustrate experimental and numerical results of residual stress distribution along S, M, and E lines in IF, low carbon and medium carbon steels. As it is stated before, experiments are performed with three samples for each type of steel. All results along a measurement line are plotted in a single graphical representation. Trend of that data determined as fifth order polynomial and results about 5 mm from weld center are predicted.

R^2 values of each trend line is calculated which determined of degree of fit of data with trend line. This value is differs for each measurement section. According to experimental results, it decreases when the carbon content of the steel increases. Cementite (iron carbide) is compound of iron and carbon. Increase of the carbon content in iron decreases ferrite proportion while amount of pearlite structure which is a combination of ferrite and cementite increases. Carbon never presents in irons as free atoms. It is always dissolved in iron as a part of these structures. Ferrite, pure iron, has a more stable crystal structure than cementite. During the travel of sound waves through the steel, less variation occur in ferrite structure when compared to cementite and pearlite structures. Accordingly, distribution of cementite and pearlite phases is not same for each sample. As a result of these effects, it can be stated that increase of carbon content increases variation of ultrasonic wave velocity at a measurement point among different samples. Results show that R^2 value is highest for steel with minimum carbon content while it decreases with the increase of carbon content.

Theoretical definition of relation between stress and ultrasonic waves fit to thin materials. However, ultrasonic wave velocity travels through the thickness of the material and affected different stress zones in a thick material. Stress can be high at upper sections and lower at bottom part. These sections have an average effect on ultrasonic wave velocity. Therefore, some discrepancy between the experimental data and finite element data is expected.

Through thickness averages of finite element equivalent stresses are calculated and compared with experimental results. Distribution of these results fit with experimental results, but values do not fit perfectly. Because, residual stress values are arithmetic means of 11 data point through the thickness. Effect of residual stress on ultrasonic waves cannot be explained with an arithmetic average. Ultrasonic waves travel through the thickness and residual stresses during this movement effect ultrasonic wave velocity. However, it is not possible to observe effect of residual stress in different sections through the thickness. Time passed during this travel is measured which provide an overall ultrasonic wave velocity and residual stress. Another point is that as mentioned previously, ultrasonic waves affected by iron carbide molecules which cause high standard deviation. As a result of these reasons experimental and numerical analyses results differ at some points.

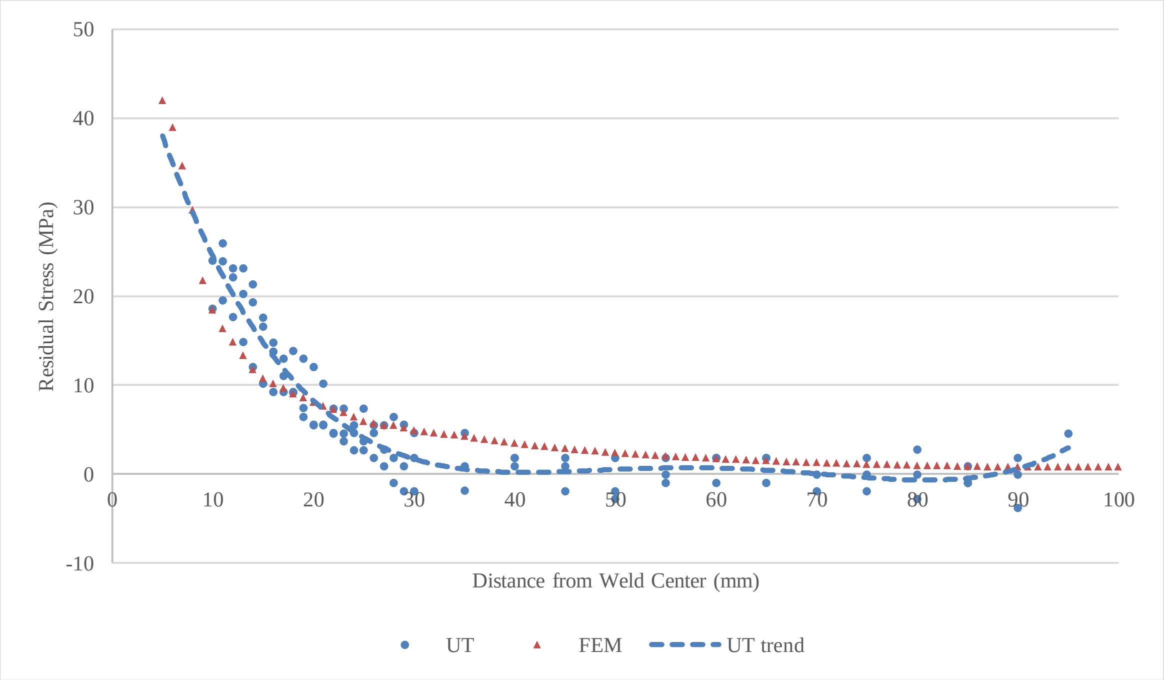

Figure 4.10. Experimental and FEM equivalent residual stress distributions along S line of IF steel

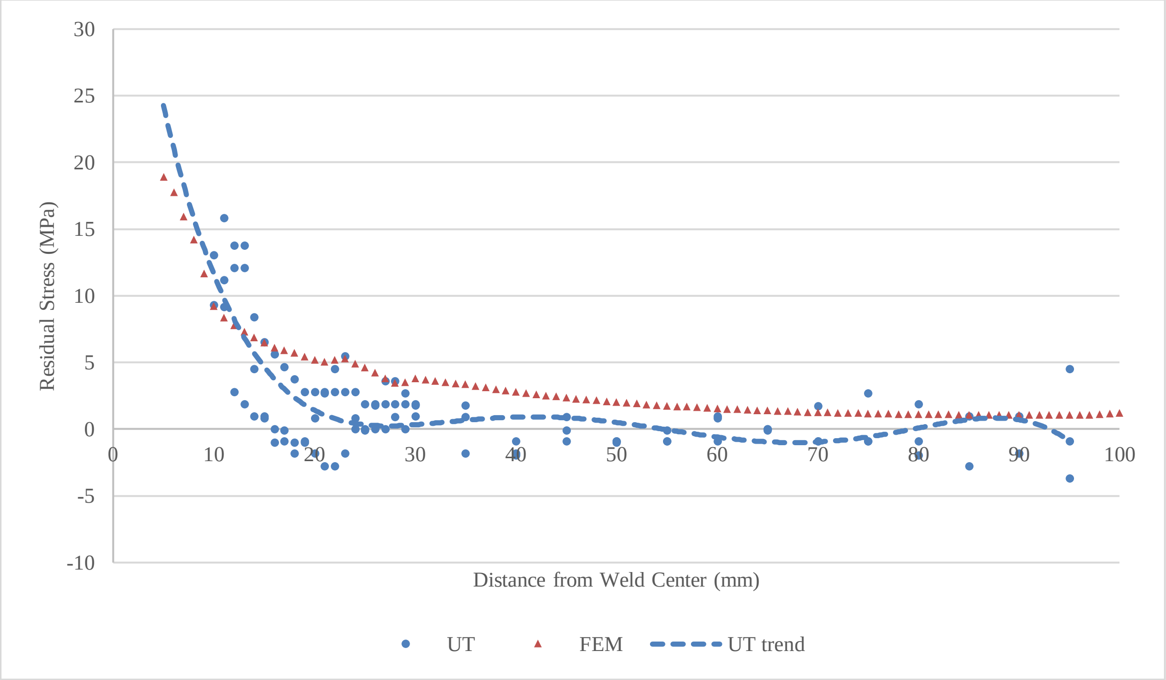

Figure 4.11. Experimental and FEM equivalent residual stress distributions along M line IF steel

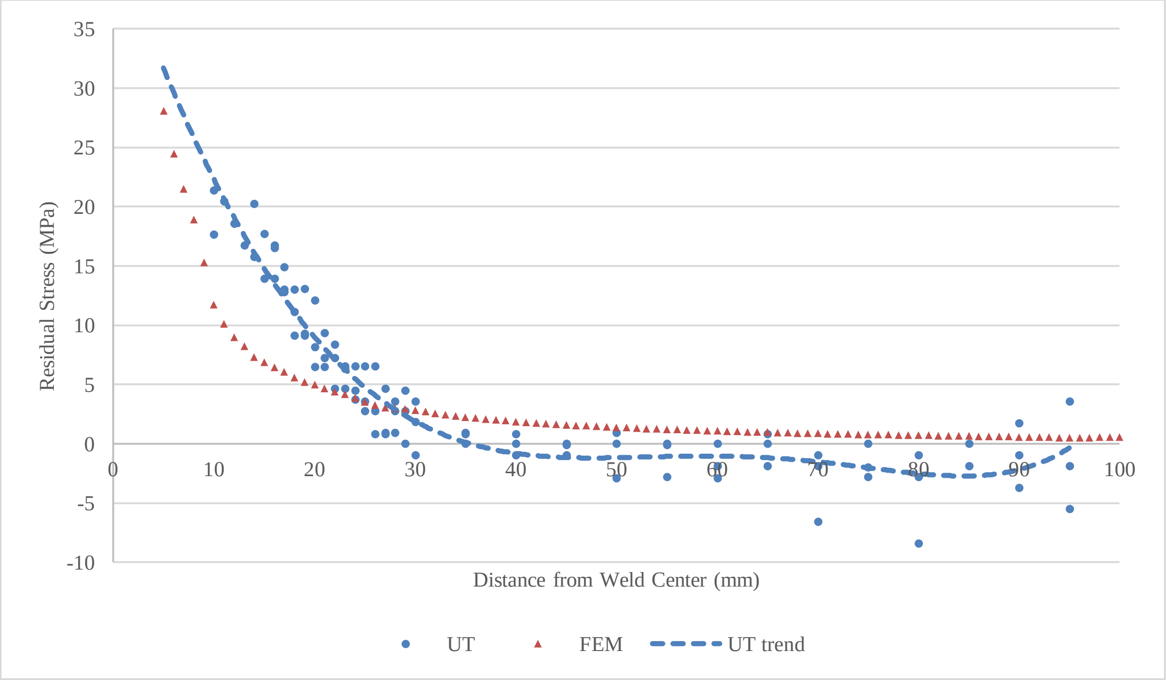

Figure 4.12. Experimental and FEM equivalent residual stress distributions along E line IF steel

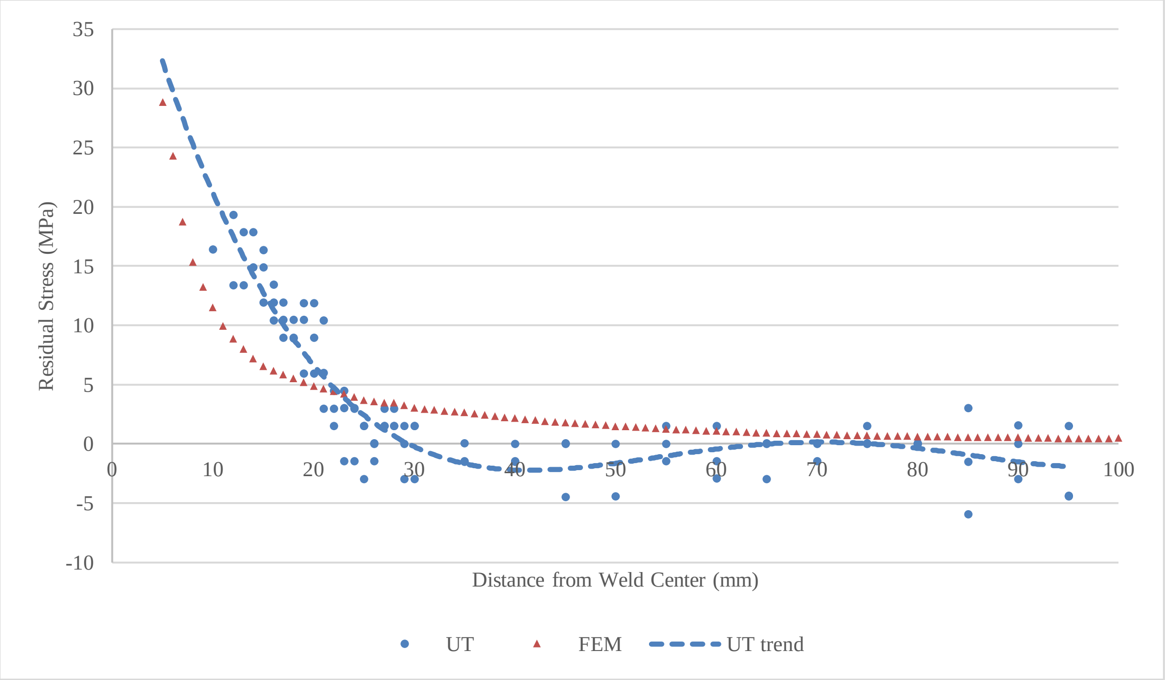

Figure 4.13. Experimental and FEM equivalent residual stress distributions along S line of low carbon steel

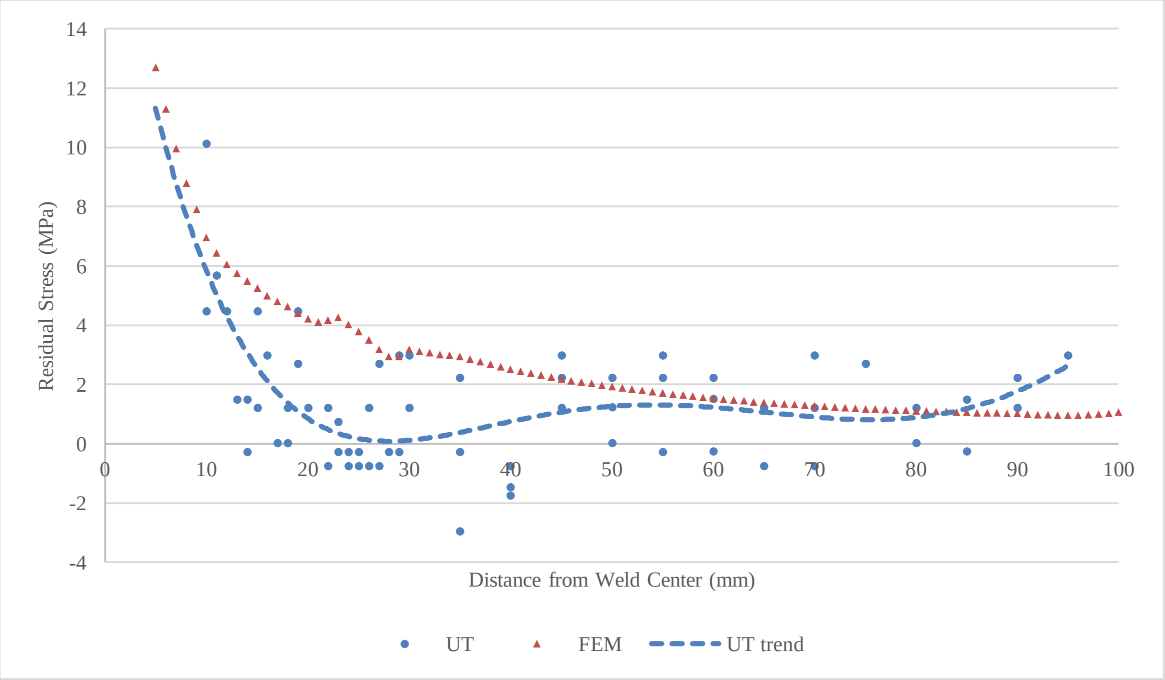

Figure 4.14. Experimental and FEM equivalent residual stress distributions along M line of low carbon steel

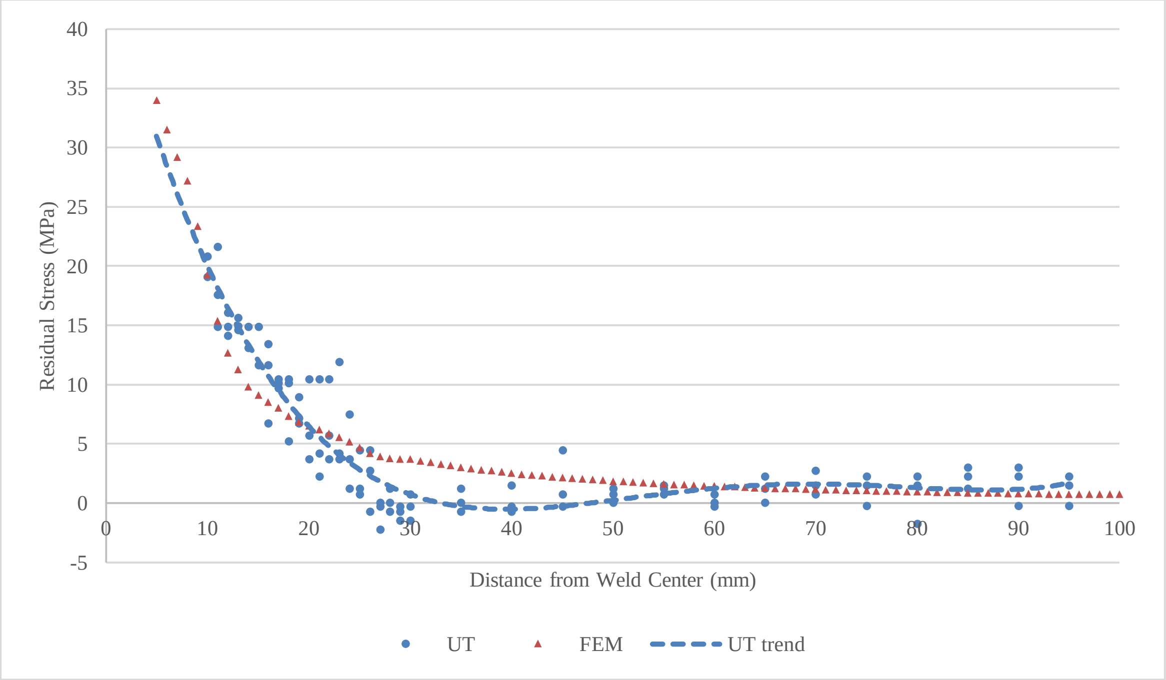

Figure 4.15. Experimental and FEM equivalent residual stress distributions along E line of low carbon steel

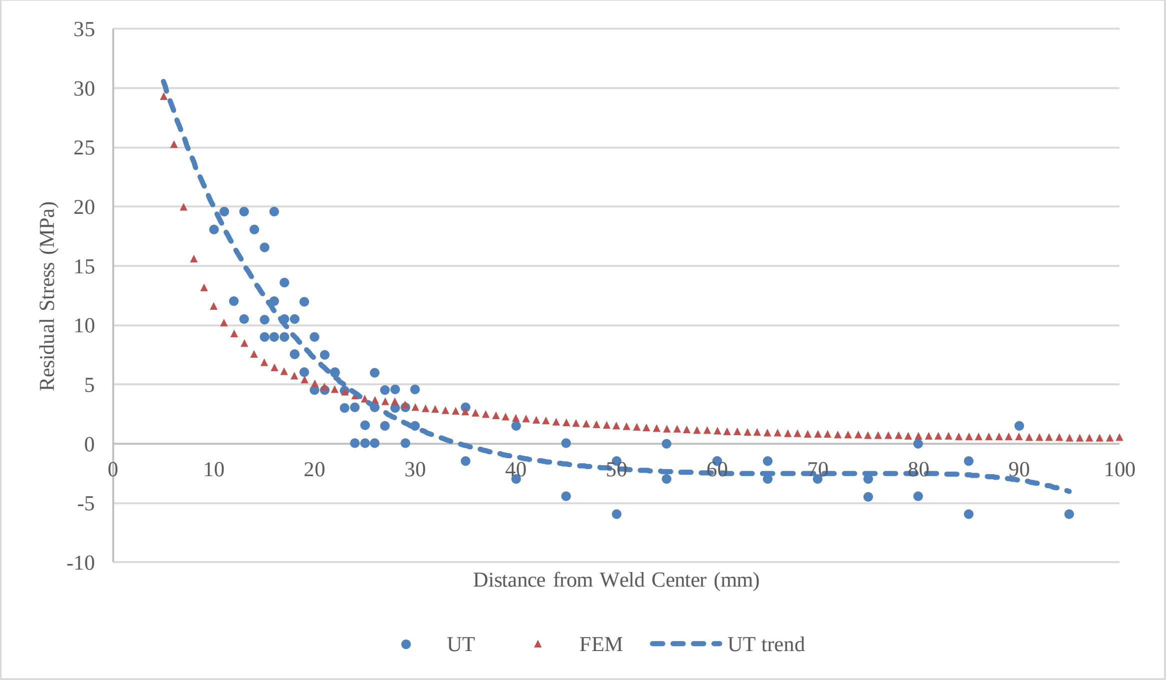

Figure 4.16. Experimental and FEM equivalent residual stress distributions along S line of medium carbon steel

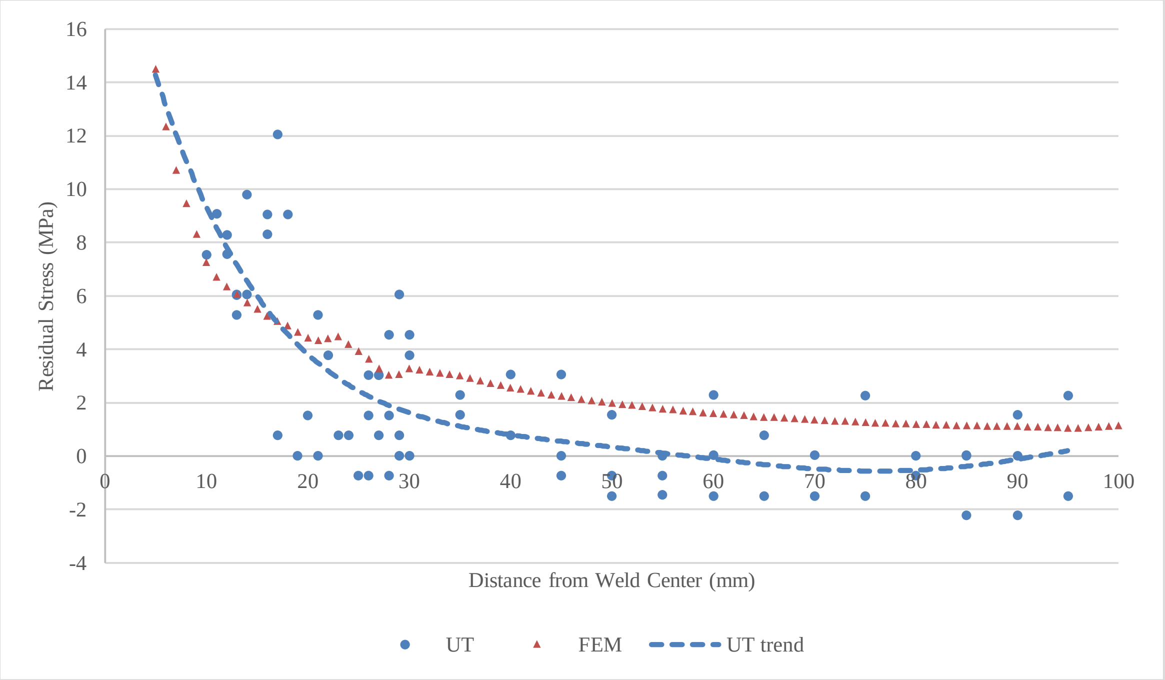

Figure 4.17. Experimental and FEM equivalent residual stress distributions along M line of medium carbon steel

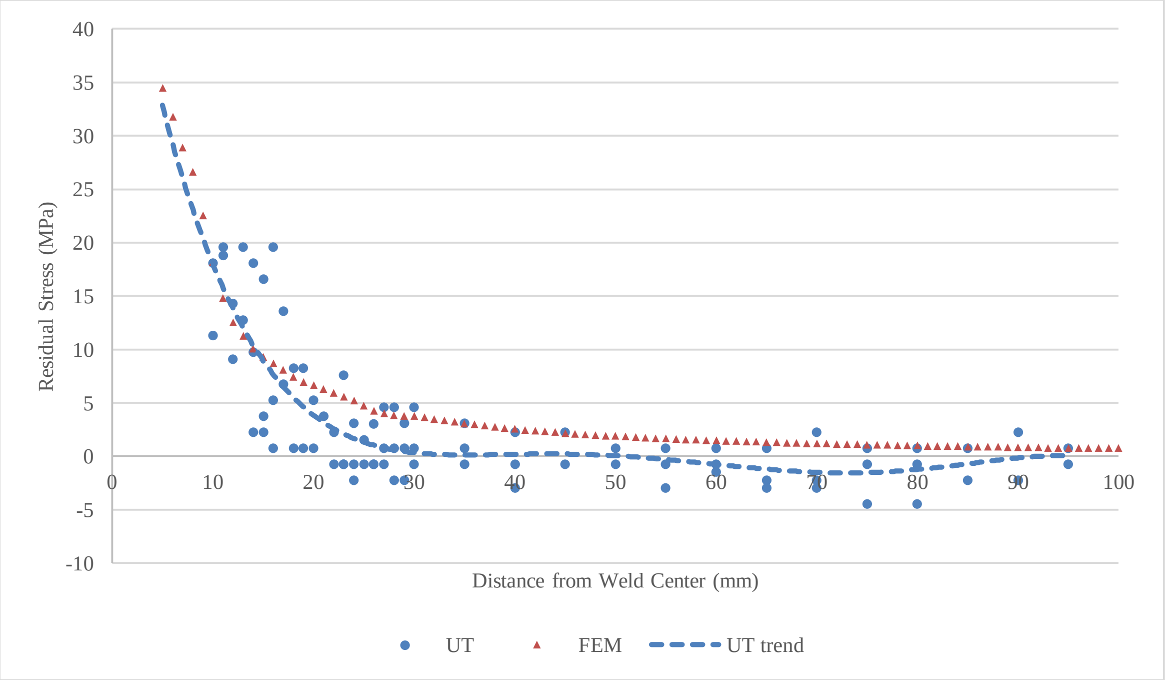

Figure 4.18. Experimental and FEM equivalent residual stress distributions along E line of medium carbon steel

Comparison of experimental results along measurement sections at each sample are given in Figures 4.17-19. Experimental results are given with finite element equivalent residual stress distributions. Residual stress in IF steel is maximum at the start of weld beam. In the middle of weld beam it is minimum and increases at the end of weld beam up to a value around 30 MPa. These results are consistent with finite element simulations.

Low and medium carbon steels show similar behavior on formation of residual stress. Residual stress peaks are similar in the beginning and end of weld beam which are higher than middle section. Finite element results show that at the end of weld beam residual stresses are higher. However, this difference is not observable in the experimental results of low carbon steel where both sections show similar distribution. Medium carbon steel have similar distribution with finite element results.

Residual stress is significantly higher at the start and end regions of weld beam in all type of steels. Similarly, another common observation is that residual stress is lower than these regions at middle part of steels. This is caused by thermal effects and mechanism of welding process. The start and end regions of weld, tips of weld beam is open and contacts directly with cold steel plate. As it is stated before, temperature difference during rapid heating and cooling is main reason of residual stress formation. These effects are higher at these points and as a result of this, residual stress is higher at these regions. Other reason is the time that passes without the movement of weld arc. In the beginning of the welding process arc strike occurs and weld arc does not move until the weld groove is filled with desired amount of filling material. Similarly at the end of weld, time passes between end of movement and termination of weld arc.

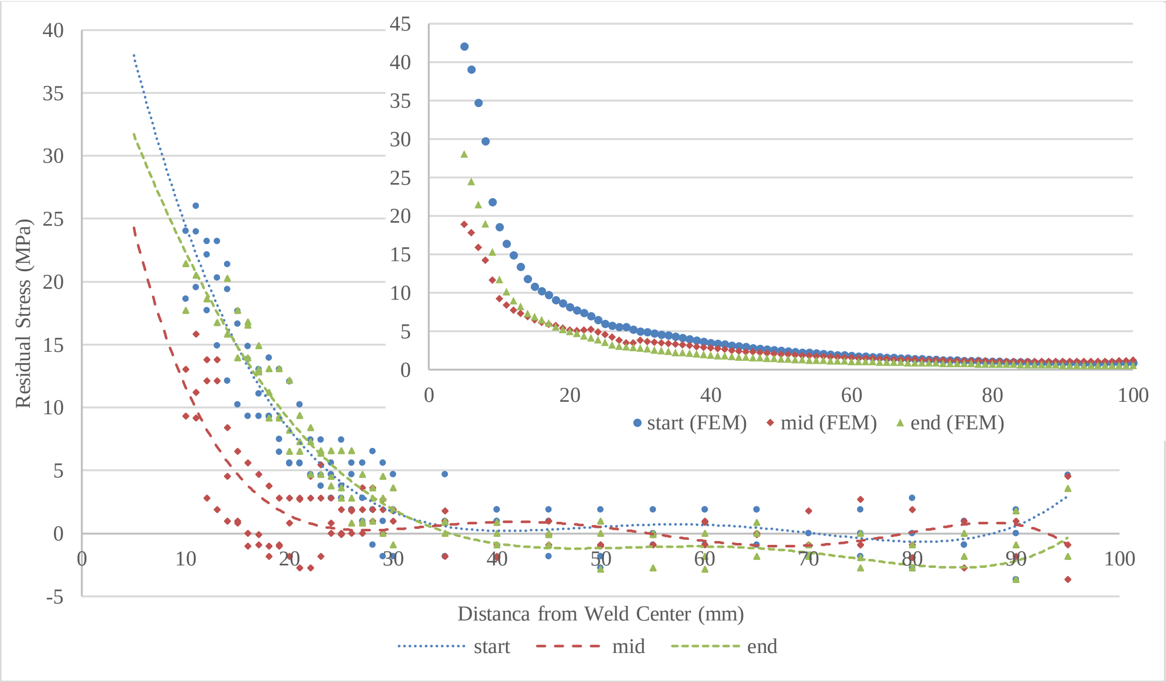

Figure 4.19. Experimental and FEM equivalent residual stress distributions in IF steel

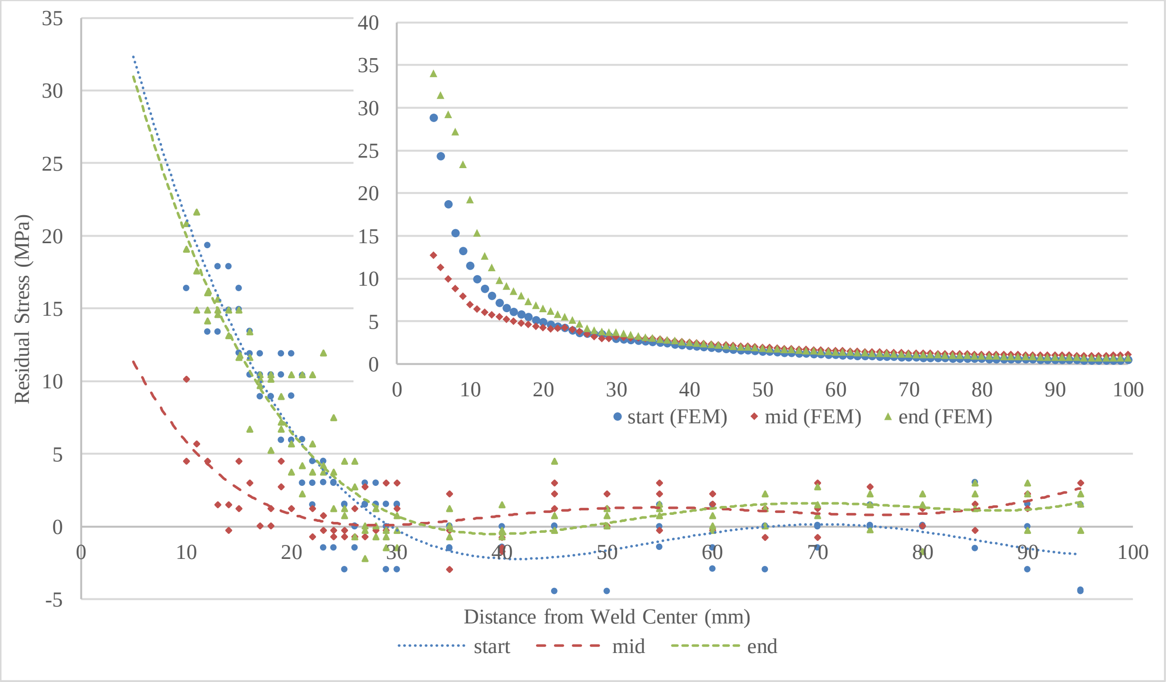

Figure 4.20. Experimental and FEM equivalent residual stress distributions in low carbon steel

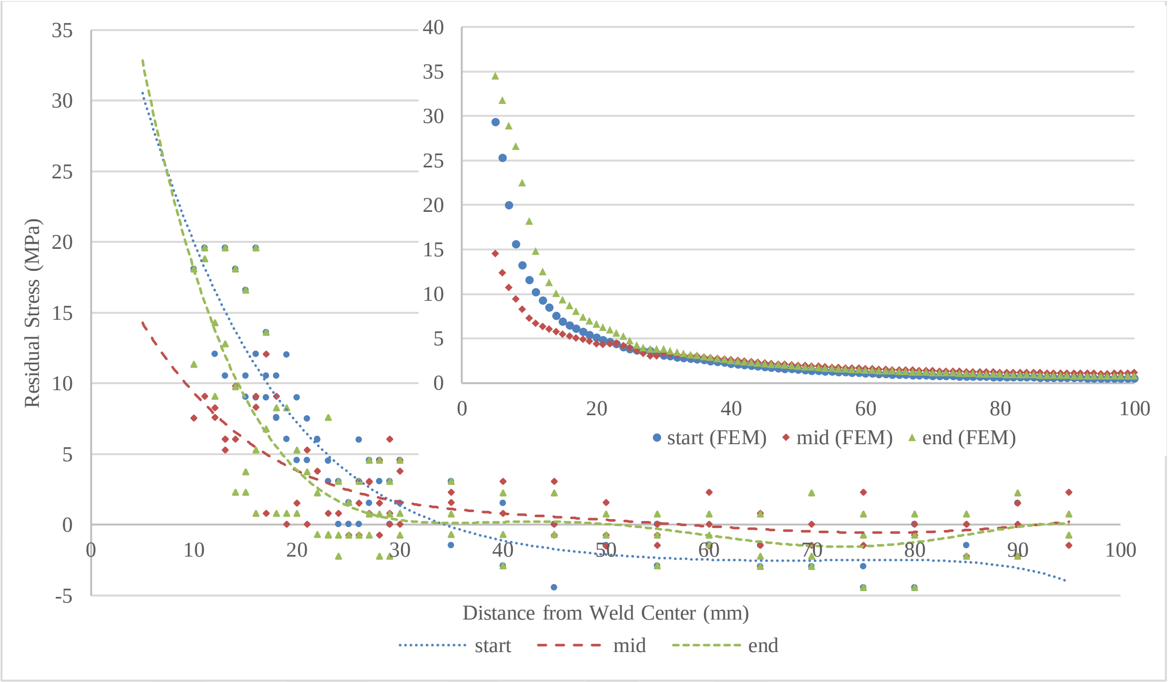

Figure 4.21. Experimental and FEM equivalent residual stress distributions in medium carbon steel

Finite element results of residual stress in terms of carbon content of the material are illustrated in Figures 4.20 to 22. Effect of carbon content on residual stress formation is investigated at each section separately. Experimental and finite element simulation results at each measurement section are compared. As it is discussed before, equivalent stress results fits to experimental results better than other type of stress results. Accordingly, experimental results are compared with equivalent stress results. Experimental and finite element results shows similar variations of residual stress according to carbon content of materials. Magnitudes of finite element results can be different than experimental measurements at a region, but relation between carbon content and residual stress perfectly fits with experimental results.

IF steel has higher peak of residual stress while other two steels with higher carbon content have lower and almost similar magnitude and distributions at the start region of weld beam. Experimental and finite element results are consistent. Medium carbon steel has residual stress peak lower than low carbon steel and IF steel reach a maximum residual stress higher than other two steels along the middle section of weld beam. Experimental results are in complete agreement with finite element results. Residual stress peaks remain same with start region of weld beam at the end of weld beam in low and medium carbon steels while it decreases in IF steel. Experimental results show that residual stress peak values are same in all type of steel at that region. Decrease in IF steel is higher in finite element simulation and IF steel have lowest value while other two steel materials have higher and almost similar residuals stress magnitude around weld beam. Peak residual stresses slightly vary but behavior are consistent in both experimental and finite element results.

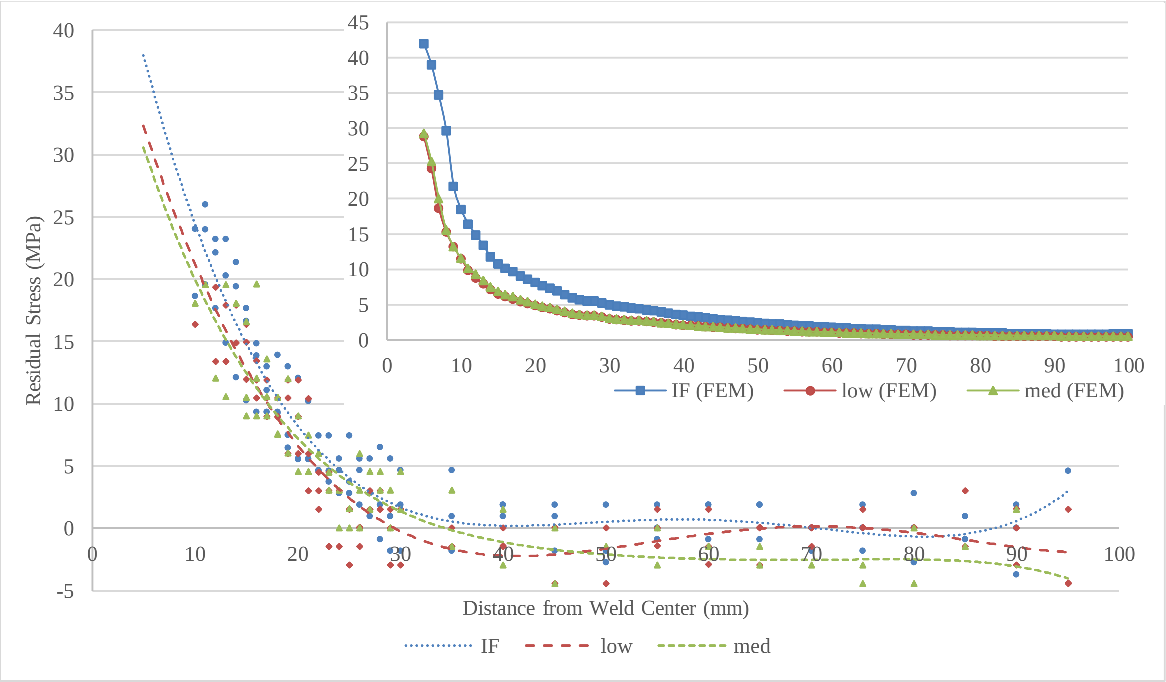

Figure 4.22. Comparison of experimental and FEM equivalent residual stresses in IF, low carbon and medium carbon steels along S line

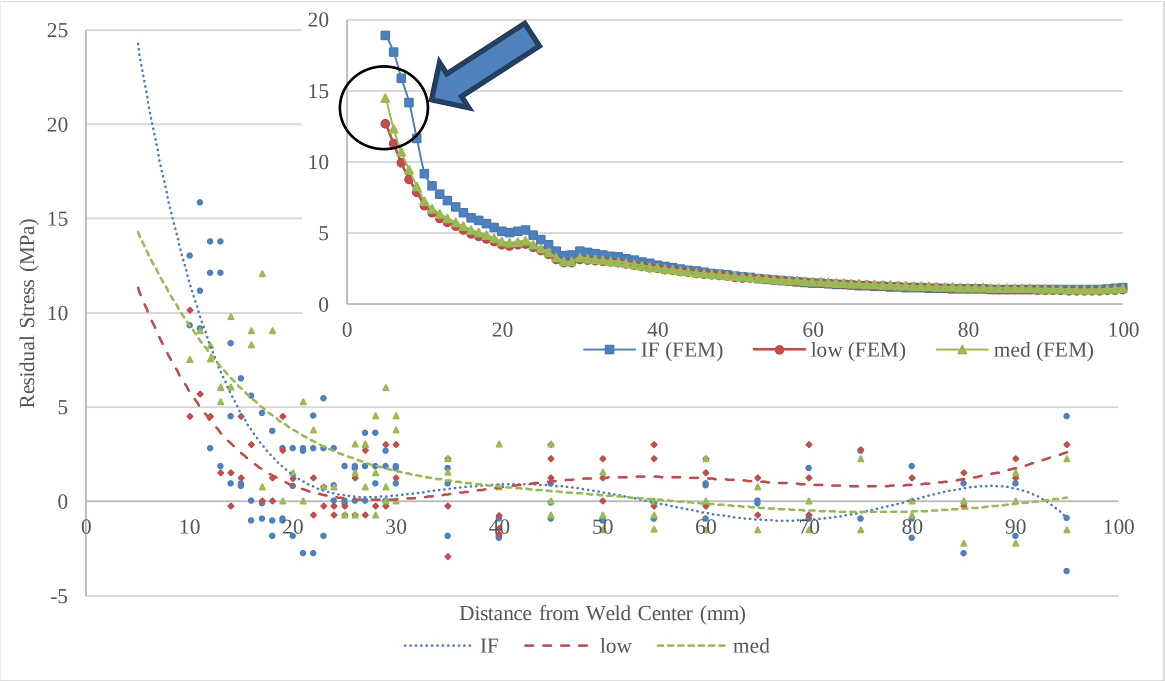

Figure 4.23. Comparison of experimental and FEM equivalent residual stresses in IF, low carbon and medium carbon steels along M line

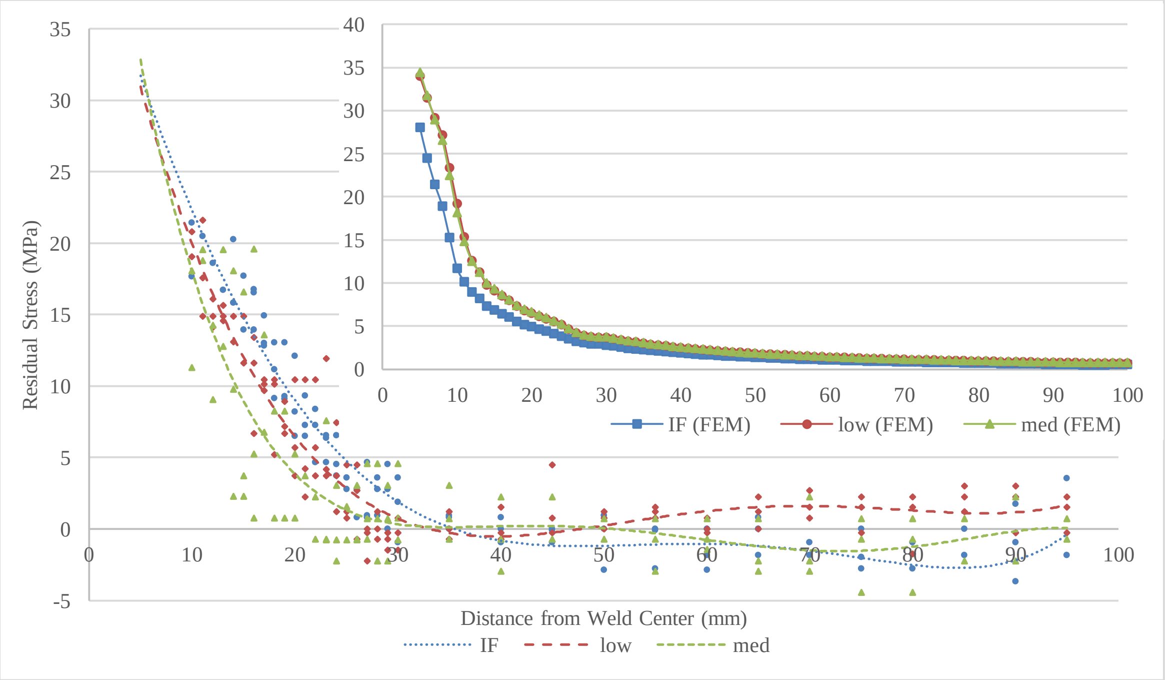

Figure 4.24. Comparison of experimental and FEM equivalent residual stresses in IF, low carbon and medium carbon steels along E line

5. CONCLUSION

During the operation, materials are exposed to loads which cause formation of stress within the material. If the material has initial stressed zones, they become more sensitive to new deformations. In order to prevent harmful effects of these pre-stressed zones, evaluation of residual stress has vital importance.

There are various reasons that cause formation of residual stress. Welding is a widely used joint technique which is used fabrication processes. This high temperature process heats up the material above the melting temperatures which is followed rapid cooling stage. As a result, residual stresses are being formed in and around the weld beam.

Analysis of welding residual stress was performed in many studies. Several destructive and non-destructive methods were investigated. However, these studies mostly dealt with the method of measurement in spite of effect of residual stress on material properties or effect of material composition on formation of residual stress. This study deals with effect of carbon content on formation of welding residual stress. This is performed by non-destructive experiments and finite element simulations.

Experimental residual stress analysis requires stress free samples which can be obtained with annealing process. However, this is a sensitive process that can have harmful effects on the material. It is required to obtain stress free samples with fine grain distribution. In order to do this, hardness tests and metallographic analyses are performed before annealing of samples to be analyzed. These tests and analyses are performed samples with different carbon content. Additionally, effect of carbon content on annealing stages of steel materials is presented.

Ultrasonic through thickness residual stress measurement is an alternative to other non-destructive analysis methods. This cost effective method is easy to be applied on metallic structures. However, this method is sensitive to material surface. Material surface should be flat. Accordingly, measurements on rough weld beam cannot be accomplished. Another point is thickness of the material. It is necessary to measure thickness accurately in order to measure ultrasonic wave velocity. This difficult task can be neglected by performing measurements on before and after stress formation. However, weld beam is produced with formation of stress zones and it is not possible to perform stress free measurements on weld beam. Therefore, it is not possible to perform residual stress measurement on weld beam using ultrasonic technique. In addition, this technique provides average results through the thickness. Different stressed zones through the thickness cannot be determined separately.

Despite the fact that ultrasonic technique has cons, it is an efficient method for analysis of effect of carbon content on formation of residual stress. Because, it is not required to investigate surface of mid plane stresses separately and residual stress formed in base metals with different carbon content are more important that residual stresses formed in weld beam.

Results show that carbon content of steel samples has effect on hardness, acoustoelastic constant and residual stress formation. It is well established that hardness increases with increasing carbon content. Relationship between ultrasonic wave velocity variations and stress is defined as acoustoelastic constant which increases with increasing carbon content in an exponential trend. It should be mentioned that this increase is in variation of ultrasonic wave velocities between two stress points. According to this trend it can be extrapolated that acoustoelastic constant will be constant after a certain percent of carbon content and effect of carbon content is not continuous.

Effect of carbon content on formation of residual stress is investigated in terms of ultrasonic wave velocities. Experimental measurements could only be performed on base metal. Results of finite element simulation are found to be consistent with experimental results. It can be stated that finite element model can be used as a complimentary data for the analysis of experimentally unreached parts of the material. Weld zone and symmetric part of base material can be modeled with finite element results.

Both of experimental and numerical analyses show that carbon content has an effect on carbon content of steels. This effect can be observed on both acoustoelastic constant and welding residual stress distributions. However, welding residual stress has a complicated mechanism. Consequently, an increasing or decreasing order cannot be observed in the whole welded sample as it is in the acoustoelastic constant. In the start, middle and end sections of the material, different distributions according to welding residual stress are observed and the trends are explained by taking into account other mechanisms.

In conclusion, this study consisted of various experimental stages, such as annealing, metallography, and ultrasonic investigation with finite element simulation. Results show that carbon content has an effect on thermal stress and residual stress formation in steel materials. This effect shows a trend for thermal stress related acoustoelastic constant while it differs at various parts of weld beam. Furthermore, ultrasonic technique is an applicable technique for this purpose. It provides sufficient data for investigation of residual stress in base metal plates.

REFERENCES

1. Li, Z., T. S., Wang, X. J., Zhang, and F. C., Zhang, "Annealing softening behaviour of cold-rolled low-carbon steel with a dual-phase structure and the resulting tensile properties", *Materials Science and Engineering A,* Vol. 552, pp. 204-210, 2012.

2. Gazder, A. A., S. S. Hazra, and E. V., Pereloma, "Annealing behaviour and mechanical properties of severely deformed interstitial free steel", *Materials Science and Engineering A,* Vol. 530, pp. 492-503, 2011.

3. Kimura, A., R., Kasada, R. Sugano, A., Hasegawa, and H., Matsui, "Annealing behaviour of irradiation hardening and microstructure in helium-implanted reduced activation martensitic steel", *Journal of Nuclear Materials,* Vol. 283-287, pp. 827-831, 2000.

4. Fargas, G., M., Anglada, and A. Mateo, "Effect of the annealing temperatures on the mechanical properties, formability and corrosion resistance of hot-rolled duplex stainless steel", *Journal of Materials Processing Technology,* Vol. 209, pp. 1770-1782, 2009.

5. Euh, K., Y. C., Kim, K., Shin, S., Lee, and N. J., Kim, "Effect of tempering on hardness improvement in a VC/steel surface-alloyed material fabricated by high energy electron-beam irradiation", *Materials Science and Engineering A,* Vol. 346, pp. 228-236, 2003.

6. Khodabakshi, F., and M., Kazeminezhad, "The annealing phenomena and thermal stability of severely deformed steel sheet", *Materials Science and Engineering A,* Vol. 528, pp. 5212-5218, 2011.

7. Irani, M., and A. K., Taheri, "Effect of forging temperature on homogeneity of microstructure and hardness of precision forged steel spur gear", *Materials Chemistry and Physics,* Vol. 112, pp. 1099-1105, 2008.

8. Sayed, A. A., and S. Kheirandish, “Affect of the tempering temperature on the microstructure and mechanical properties of dual phase steels”, *Materials Science and Engineering A,* Vol. 532, pp. 21-25, 2012.

9. Negm, N. Z., “Effect of annealing temperature on properties of H_2/N_2 rf plasma-treated stainless steel”, *Surface & Coatings Technology*, Vol. 201, pp. 1763-1767, 2006.

10. Liu, Y., J., Fang, D., Liu, Z., Lu, F., Liu, S., Chen, and C. T., Liu, “Formation of oxides particles in ferritic steel by using gas-automized powder”, *Journal of Nuclear Materials*, Vol. 396, pp. 86-93, 2010.

11. Lee, D. G., K., Lee, and S., Lee, “Effects of tempering on microstructure, hardness, and fracture toughness of VC/Steel surface composite fabricated by high energy electron beam irradiation”, *Surface & Coating Technologies*, Vol. 201, pp. 1296-1301, 2006.

12. Kang, S., Y. S., Jung, J. H., Jun, and Y. K., Lee, “Effects of recrystallization annealing temperature on carbide precipitation, microstructure, and mechanical properties in Fe-18Mn-0.6C-1.5Al TWIP steel”, *Materials Science and Engineering A*, Vol. 527, pp. 745-751, 2010.

13. Razaee, A., A., Najafizadeh, A., Kermanpur, and M., Moallemi, “The influence of reversion annealing behaviour on the formation of nanograined structure in AISI 201L austenitic stainless steel through martensite treatment”, *Materials and Design*, Vol. 32, pp. 4437-4442, 2011.

14. Huang, C. A., K. C., Li, W., Lin, and M. C., Liao, “The behaviour of electroplated hard-chromium on Cr-Mo steel subject to long-term annealing at 250 ^{o}C”, *Materials Science and Engineering A*, Vol. 403, pp. 222-226, 2005.

15. Rogal, L., and J., Dutkiewicz, “Effect of annealing on microstructure, phase composition and mechanical properties of thixo-cast 100Cr6 steel”, Materials Characterization, Vol. 68, pp. 123-130, 2012.

16. Yang, K., H., Gou, B., Zhang, R., Huang, H., Li, M., Lu, X., Zhang, and J., Zhang, “Microstructures and fracture features of cold-rolled low carbon steel sheet after annealing and mechanical stress concurrently loaded”, Materials Science and Engineering A, Vol. 502, pp. 126-130, 2009.

17. Hosseini, S. M., A., Najafizadeh, and A., Kernanpur, “Producing the nano/ultrafine grained low carbon steel by martensite process using plane strain compression”, Journal of Material Processing Technology, Vol. 211, pp. 230-236, 2011.

18. Medvedeva, A., J. Bergstorm, S., Gunnarsson, and J., Andersson, “High temperature properties and microstructural stability of how-work tool steels”, Materials Science and Engineering A, Vol. 523, pp. 39-46, 2009.

19. Liu, J. B., X. H., Liu, W., Liu, Y. W., Zeng, and K. Y., Shu, “Microstructure and hardness evolution during isothermal process at 700 ^{o}C for Fe-24Mn-0.7Si-1.0Al TWPI steel”, Materials Characterization, Vol. 61, pp. 1356-1358, 2010.

20. Forouzan, F., A., Najafizadeh, A., Kermanpur, A., Hedayati, and R., Surkialiabad, “Production of nano/submicron grained AISI 304L stainless steel through the martensite reversion process”, Materials Science and Engineering A, Vol. 527, pp. 7334-7339, 2010.

21. Chowdhury, S. G., S., Datta, B. R., Kumar, P. K., De, R. N., Ghosh, “Randomization of texture during recrystallization of austenite in a cold rolled metastable austenitic stainless steel”, Materials Science and Engineering, Vol. 443, pp. 114-119, 2007.

22. Velasco, F., G., Blanco, A., Bautista, and M. A., Martinez, “Effect of welding on local mechanical properties of stainless steels for concrete structures using universal hardness test”, *Construction and Building Materials*, Vol. 23, pp. 1883-1891, 2009.

23. Frydman, S., L., Konat, and G., Pekalski, “Structural and hardness changes in welded joints of Hardox steels”, *Archives of Civil and Mechanical Engineering*, Vol. 8, pp. 15-27, 2008.

24. Ziemian, C. W., M. M., Sharma, and D. E., Whaley, “Effects of flashing and upset sequences on microstructure, hardness, and tensile properties of welded structural steel joints”, *Materials and Design*, Vol. 33, pp. 175-184, 2012.

25. Ueji, R., H., Fujii, L., Cui, A., Nishioka, K., Kunishige, and K., Nogi, “Friction stir welding of ultrafine grained plain low-carbon steel formed by the martensite process”, *Materials Science and Engineering A*, Vol. 423, pp. 324-330, 2006.

26. Güral, A., B., Bostan, and A. T., Özdemir, “Heat treatment in two phase region and its effect on microstructure and mechanical strength after welding of a low carbon steel”, *Materials and Design*, Vol. 28, pp. 897-903, 2007.

27. Acarer, M, and B., Demir, “An investigation of mechanical and metallurgical properties of explosive welded aluminium-dual phase steel”, *Materials Letters*, Vol. 62, pp. 4158-4160, 2008.

28. Abdullah, H. A., and R. A., Siddiqui, “Concurrent laser welding and annealing exploiting robotically manipulated optical fibers”, *Optics and Lasers in Engineering*, Vol. 38, pp. 473-484, 2002.

29. Klobcar, D., J. Tusek, B., Taljat, L., Kosec, and M., Pleterski, “Aging of maraging steel welds during aluminium alloy die casting”, *Computational Materials Science*, Vol. 44, pp. 515-522, 2008.

30. Li, C., Y. Wang, Z. Zhang, B., Han, and T., Han, “Influence of overlapping ratio on hardness and residual stress distributions in multi-track laser surface melting roller steel”, *Optics and Lasers in Engineering*, Vol. 48, pp. 1224-1230, 2010.

31. Palanichamy, P., A., Joseph, T., Jayakumar, and B., Raj, “Ultrasonic velocity measurements for estimation of grain size in austenitic stainless steel”, *NDT&E International*, Vol. 28, pp. 179-185, 1995.

32. Sarpün, İ. H., V., Özkan, S., Tuncel, and R., Ünal, “Determination of mean grain size by ultrasonic methods of tugsten carbide and boron carbide composites sintered at various temperatures”, *4th International Conference on NDT*, 2007.

33. Sarpün, İ. H., S., Tuncel, and R., Ünal, “Mean grain size determination in marbles by ultrasonic techniques”, *ECNDT*, 2006.

34. Mutlu, İ, E., Oktay, and S., Ekinci, “Effect of grain size on the ultrasonic parameters in stainless steel”, International Journal of Microstructure and Materials Properties, Vol. 4, pp. 423-435, 2009.

35. Brosey, W. D., “Ultrasonic determination of grain size in uranium”, *Library of Congress Cataloging in Publication Data*, Vol. 2A, pp. 1399-1409, 1983.

36. Bouda, A. B., S. Lebaili, and A., Benchaala, “Grain size influence on ultrasonic velocities and attenuation”, *NDT&E International*, Vol. 36, pp. 1-5, 2003.

37. Reynolds, A. P., W., Tang, T. G., Herold, and H., Prask, “Structure, properties, and residual stress of 304L stainless steel friction stir welds”, *Scripta Materials*, Vol. 48, pp. 1289-1294, 2003.

38. Dakhlaoui, R., C., Braham, and A., Baczmanski, “Influence of chemical composition and residual stresses on mechanical properties of duplex stainless steel studies by X-ray and neutron diffraction”, *Journal of Neutron Research*, Vol. 15, pp. 131-137, 2007.

39. Rogante, M., P., Mikula, and M., Vrana, “Through the thickness residual stress analysis by neutron diffraction in inoxidizable martensitic steel samples with and

without tungsten carbie coating”, *Surface and Coatings Technology*, Vol. 204, pp. 650-656, 2009.

40. Carrado, A., and H., Palkowski, “Interface and in bulk residual stress analysis in biomedical systems by non-destructive techniques”, *Surface and Coatings Technology*, in Press, 2012.

41. Aydıner, C. C., E., Üstündağ, B., Clausen, J. C., Hanan, R. A., Winholtz, M. A. M., Bourke, and A., Peker, “Residual stresses in a bulk metallic glass stainless steel composite”, *Materials Science and Engineering*, Vol. 399, pp. 107-113, 2005.

42. Park, M. J., H. N., Yang, D. Y. Jang, J. S., Kim, and T. E., Jin, “Residual stress measurement on welded specimen by neutron diffraction”, *Journal of Materials Processing Technology*, Vol 155-156, pp. 1171-1177, 2004.

43. Wimpory, R. C., C., Ohms, M., Hofmann, R., Schneider, A.G., Youtsos, “Statistical analysis of residual stress determinations using neutron diffraction”, International Journal of Pressure Vessels and Piping, Vol. 86, pp. 48-68, 2009.

44. Knupfer, S. M., A. M., Paradowska, O., Kirstein, and A. J., Moore, "Characterization of the residual strains in iterative laser forming", Journal of Materials Processing Tech., Vol. 212, pp. 90-99, 2012.

45. Pratihar, S., M., Turski, L., Edwards, and P. J., Bouchard, "Neutron diffraction residual stress measurements in a 316L stainless steel bead-on-plate weld specimen", Materials Engineering, Vol. 86, pp. 13-19, 2009.

46. Larsson, C., T. M., Holden, M. A. M., Bourke, M., Stout, J., Teauge, and L. E. Lindgren, “Measurement and modeling of residual stress in a welded Haynes® 25 cylinder”, Material Mechanics, Vol. 399, pp. 49-57, 2005.

47. Edwards, L., P. J., Bouchard, M., Dutta, D. Q., Wang, J. R., Santisteban, S., Hiller, M. E., Fitzpatrick, “Direct measurement of the residual stresses near a boat-shaped

repair in a 20 mm thick stainless steel tube butt weld", *International Journal of Pressure Vessels and Piping,* Vol. 82, pp. 288-298, 2005.

48. Brown, D. W., T. M., Holden, B., Clausen, M. B., Prime, T. A., Sisneros, H., Swenson, And J., Vaja, "Critical comparison of two independent measurements of residual stress in an electron-beam welded uranium cylinder: Neutron diffraction and the contour method", *Acta Materialia*, Vol. 59, pp. 864-873, 2011.

49. Woo, W., G. B., An, E. J., Kingston, A. T., DeWald, D. J., Smith, and M. R., Hill, "Through-thickness distributions of residual stresses in two extreme heat-input thick welds: A neutron diffraction, contour method and deep hole drilling study", *Acta Materialia*, Vol. 61, pp. 3564–3574, 2013.

50. Turski, M., J. A., Francisa, P. R., Hurrell, S. K., Bate, S., Hiller, and P. J., Withers, "Effect of stop start features on residual stresses in a multipass austenitic stainless steel weld", *International Journal of Pressure Vessels and Piping*, Vol. 89, pp. 9-18, 2012.

51. Doylea, E. D., Y. C. Wong, and M. I. Ripley, "Residual stress evaluation in martensitic stainless steel as a function of gas quenching pressure using thermal neutrons", *Physica B: Condensed Matter,* Vol. 385–386, pp. 897-899, 2006.

52. Bendeich, P., N., Alam, M., Brandt, D., Carr, K., Short, R., Blevins, C., Curfs, O., Kirstein, G., Atkinson, T., Holden, and R., Rogge, "Residual stress measurements in laser clad repaired low pressure turbine blades for the power industry", *Materials Science and Engineering: A*, Vol. 437, pp. 70-74, 2006.

53. Ficquet, X., D. J., Smith, C.E., Truman, E. J., Kingston, and R.J., Dennis, "Measurement and prediction of residual stress in a bead-on-plate weld benchmark specimen", International Journal of Pressure Vessels and Piping, Vol. 86, pp. 20-30, 2009.

54. Fratini, L., and, B., Zuccarello, “An analysis of through thickness residual stresses in aluminium FSW butt joints”, *International Journal Of Machine Tools & Manufacture*, Vol. 46, pp. 611-619, 2006.

55. Biot, B. A., “The influence of initial steels on elastic waves”, Journal of Applied Physics, Vol. 11, pp. 522-530, 1940.

56. Hughes, D. S., and J. L., Kelly, “Second-order elastic deformation of solids”, Physical Review, Vol. 92, pp. 1145-1149, 1953.

57. Thurston, R. N., “Effective elastic coefficients for wave propagation in crystals under stress”, Vol. 37, pp. 348-356, 1964.

58. Egle, D. M., and D. E., Bray, “Measurement of acoustoelastic and third order elastic constants for rail steel”, Vol. 60, pp. 741-744, 1976.

59. Hirao, M., H., Fukuoka, and K., Hori, “Acoustoelastic effect of Rayleigh surface wave in isotropic material”, Vol. 48, pp. 119-124, 1981.

60. Hussaon, D., “A perturbation theory for the acoustoelastic effect of surface waves”, Vol. 57, pp. 1562-1568, 1985.

61. Thompson, R. B., S. S. Lee, and J. F. Smith, “Angular dependence of ultrasonic wave propagation in a stresses, orthorhombic continuum: Theory and application to the measurement of stress and texture”, Acoustic Society of America, Vol. 80, pp. 921-931, 1986.

62. Man, C., and W. Y., Lu, “Towards an acoustoelastic theory for measurement of residual stress”, Journal of Elasticity, Vol. 17, pp. 159-182, 1987.

63. Lu, W. Y., L. W., Pen, and S., Holland, “Measurement of acoustoelastic effect of Rayleigh surface waves using laser ultrasonics”, *OSTI*, 1997.

64. Akhshik, S., and R., Moharrami, “Improvement in accuracy of the measurements of residual stresses due to circumferential welds in thin-walled pipe using Rayleigh wave method”, *Nuclear Engineering and Design,* Vol. 239, pp. 2201-2208, 2009.

65. Hu, E., T., He, and Y., Chen, “Experimental study on the surface stress measurement with Rayleigh wave detection technique”, *Applied Acoustics,* Vol. 70, pp. 356-360, 2009.

66. Todaro, M. E., and G. P., Capsimalis, “Acoustoelastic effect for Rayleigh surface waves in the presence of a non-uniform stress field”, *Ultrasonics Symposium*, pp. 229-232, 1986.

67. Allison, S. G., J. S., Heyman, and K. Salama, “Ultrasonic measurement of residual deformation stress in thin metal plates using surface acoustic waves”, *Ultrasonic Symposium*, pp. 995-999, 1983.

68. Duqennoy, M., M., Ouaftouh, and M., Ourak, “Determination of stresses in aluminium alloy using optical detection of Rayleigh waves”, Ultrasonics, Vol. 37, pp. 365-372, 1999.

69. Liu, M., J. Y., Kim, L., Jacobs, and J., Qu, “Experimental study of nonlinear Rayleigh wave propagation in shot-peened aluminium plates-Feasiblity of measuring residual stress”, NDT&E International, Vol. 44, pp. 67-74, 2011.

70. Duquennoy, M., M., Ouaftouh, M. L., Qian, F., Jenot, and M., Ourak, “Ultrasonic characterization of residual stresses in steel rods using a laser line source and piezoelectric transducers”, *NDT&E International,* Vol. 34, pp. 355-362, 2001.

71. Duquennoy, M., M., Ouaftouh, and M., Ourak, “Ultrasonic evaluation of stresses in orthotropic materials using Rayleigh waves”, Vol. 32, pp. 189-199, 1999.

72. Namkung, M., and J. S., Heyman, “Residual stress characterization with a magnetic/ultrasonic techniques”, *Ultrasonics Symposium,* pp. 950-954, 1984.

73. Li, L., J., Ding, F., Liu, and J., Zhang, “Study on travel time measurement with Lcr wave in shrear stress evaluation”, *Proceedings of the 2006 IEEE*, pp. 939-944, 2006.

74. Qozam, H., J., Hoblos, G., Bourse, C., Robin, H., Walaszek, P., Bouteille, and M., Cherfaoui, “Ultrasonic stress measurement in welded component by using Lcr waves: Analysis of the microstructure effect”, *Materials Science Forum*, Vols. 524-525, pp. 453-458, 2006.

75. Bray, D. E., and P., Junghans, “Application of the Lcr ultrasonic technique for evaluation of post-weld heat treatment in steel plates”, *NDT&E International*, Vol. 28, pp. 235-242, 1995.

76. Javadi, Y., H. S., Pirzaman, M. H., Raeisi, and M. A., Najafabadi, “Ultrasonic inspection of a welded stainless steel pipe to evaluate residual stresses through thickness”, Materials and Design, Vol. 49, pp. 591-601, 2013.

77. Bray, D. E., and W., Tang, “Subsurface stress evaluation in steel plates and bars using the Lcr ultrasonic wave”, *Nuclear Engineering and Design*, Vol. 207, pp. 231-240, 2001.

78. Javadi, Y., O., Afzali, M. H., Raeisi, and M. A., Najafabadi “Nondestructive evaluation of welding residual stresses in dissimilar welded pipes”, Journal of Nondestructive Evaluation, Vol. 32, pp. 177-187, 2013.

79. Javadi, Y., M., Akhlaghi, and M. A., Najafabadi, “Using finite element and ultrasonic method to evaluate welding longitudinal residual stress through the thickness in austenitic stainless steel plates”, Materials and Design, Vol. 45, pp. 628-642, 2013.

80. Walaszek, H., C., Peyrac, J., Hoblos, and J., Rivenez, “Potentialities of ultrasonics for evaluating residual stresses: Influence of microstructure”, *Journal of Pressure Vessel Technology*, Vol. 124, pp. 348-353, 2002.

81. Javadi, Y., and M. A., Najafabadi, “Comparison between contact and immersion ultrasonic method to evaluate welding residual stresses of dissimilar joints”, Materials and Design, Vol. 47, pp. 473-482, 2011.

82. Qozam, H., S. Chaki, G. Bourse, C. Robin, H. Walaszek, and P. Bouteille, “Microstructure effect on the Lcr elastic waves for welding residual stress measurement”, Experimental Mechanics, Vol. 50, pp. 179-185, 2010.

83. Bray, D. E., and B. H., Chance, “Nondestructive monitoring of stress relaxation in welded steel plates”, Journal of Pressure Vessel Technology, Vol. 124, pp. 343-348, 2002.

84. Schneider, E., K., Goebbels, G. Hübschen, and H. J., Salzburger, “Determination of residual stress by time of flight measurements with linear polarized shear waves”, *Ultrasonics Symposium*, pp. 956-959, 1981.

85. Blessing, G. V., N. N., Hsu, and T. M. Proctor, “Ultrasonic shear wave measurement of known residual stress in aluminium”, Experimental Mechanics, Vol. 24, pp. 218-222, 1984.

86. Yamagishi, H., M., Fukuhara, and A. Chiba, “Residual Stress Behavior of Rolled Aluminum Alloy A2024T3 in a Thin Plate During Cyclic-Tension Fatigue Studied Using Ultrasonic Horizontally Polarized Shear Waves”, Materials Transactions, Vol. 51, pp. 962-968, 2010.

87. Clark, A. V., and J. C. Moulder, “Residual stress determination in aluminium using electromagnetic acoustic transducers”, *Ultrasonics*, Vol. 23, pp. 253-259, 1985.

88. Frankel, J., W., Scholz, G., Capsimalis, and W., Korman, “Residual stress measurement in circular steel cylinders”, *Ultrasonics Symposium*, pp. 1009-1012, 1983.

89. Fukuoka, H., H., Toda, and T., Yamane, “Acoustoelastic stress analysis of residual stress in a patch welded disk”, *Experimental Mechanics*, Vol. 18, pp. 277-280, 1978.

90. Murayan, R., and K. Misumi, “Development of a non-contact stress measurement system during tensile testing using the electromagnetic acoustic transducer for a Lamb wave”, *NDT&E International*, Vol. 39, pp. 299-303, 2006.

91. Kudryavtsev, Y., and J., Kleiman “Measurement of residual stresses in welded elements and structures by ultrasonic method”, International Institute of Welding, IIW Document XIII-2339-10, 2010.

92. T Gnäupel-Herold, T., H. J., Prask, A. V., Clark, C. S., Hehman, and T. N., Nguyen “A comparison of neutron and ultrasonic determination of residual stress”, Measurement Science and Technology, Vol. 11, pp. 436-447, 2000.

93. Gachi, S., F., Boubenider, F., Belahcene, and A., Boucherit, “Ultrasonic residual stress measurement in AA7075-T6 FSW welded plate”, 3rd International Conference on Integrity, Reliability and Failure, 2009.

94. Jacquot, T., Nogues, M., and U., Hofmann, “Residual stress analysis on heavy plates by ultrasonic testing”, Metallurgical Research & Technology, Vol. 100, pp. 1023-1027, 2003.

95. Chaki, S., and G., Bourse, “Guided ultrasonic waves for non-destructive monitoring of the stress levels in prestressed steel strands”, Vol. 49, pp. 162-171, 2009.

96. Mashall, M. B., R. Lewis, and R. S., Dwyer-Joyce, “The application of ultrasound as a tool for studying contact stresses in railway engineering component contacts”, *Proceedings of JRC 2005 Joint Rail Conference*, pp. 83-88, 2005.

97. Scott, M. P., D. M., Barnett, and D. B., Ilic, “The non-destructive determination of residual stress in extruded billets from acoustoelastic measurements”, *Ultrasonics Symposium*, pp. 265-268, 1979.

98. Sanderson, R. M., and Y. C., Shen, “Measurement of residual stress using laser-generated ultrasound”, *International Journal of Pressure Vessels and Piping*, Vol. 87, pp. 762-765, 2010.

99. Doxbeck, M., M. A., Hussain, and J., Frankel, “Use of laser generated creeping longitudinal waves to determine residual stresses”, *2000 IEEE Ultrasonics Symposium*, pp. 725-728.

100. Vangi, D., “Stress evaluation by pulse-echo ultrasonic longitudinal wave”, *Experimental Mechanics*, Vol. 43, pp. 277-281, 2001.

101. Salama, K., G. C., Barber, and N., Chandrasekaran, “Measurement of residual stress using the temperature dependence of ultrasonic velocity”, *Ultrasonics Symposium*, pp. 877-884, 1982.

102. Karabutov, A., A., Devichensky, A., Ivochkin, M., Lyamshev, I., Pelivanov, U., Rohadgi, V. Solomatin, and M., Subudhi, “Laser ultrasonic diagnostics of residual stress”, *Ultrasonics*, Vol. 48, pp. 631-635, 2008.

103. H. D., Hibbitt, and P. V., Marcal, “A numerical thermo-mechanical model for the welding and subsequent loading of a fabricated structure”, *Computers & Structures*, Vol. 3, pp. 1145-1174, 1973.

104. B. A. B. Andersson, “Thermal stresses in a submerged-arc welded joint considering phase transformations”, *ASME Journal of Engineering Materials and Technology*, Vol. 100, pp. 356-362. 1978.

105. R.E. Nickell and H.D. Hibbitt, “Thermal and mechanical analysis of welded structures”, *Nuclear Engineering and Design*, Vol. 32, pp. 110-120, 1975.

106. E. Friedman, “Analysis of weld puddle distortion and its effect on penetration”, *Welding Journal*, Vol. 57, pp. 161-166, 1978.

107. Teng, T., and P., Chang, “A study of residual stresses in multi-pass grith-butt welded pipes”, *International Journal of Pressure Vessels and Piping,* Vol. 74, pp. 59-70, 1997.

108. Tsirkas, S. A., P., Papanikos, and T., Kermanidis, “Numerical simulation of the laser welding process in butt-joint specimens”, *Journal of Materials Processing Technology,* Vol. 134, pp. 59-69, 2003.

109. Teng, T., and P., Chang, “Numerical and experimental investigation on the residual stress of the butt-welded joints”, *Computational Materials Science*, Vol. 29, pp. 511-512, 2004.

110. Zhu, X. K., and Y. J., Chao, “Numerical simulation of transient temperature and residual stress in friction stir welding of 304L stainless steel”, *Journal of Material Processing Technology*, Vol. 146, pp. 263-272, 2004.

111. Teng, T., P., Chang, and W., Tseng, “Effect of welding sequences on residual stresses”, *Computers and Structures,* Vol. 81, pp. 273-286, 2003.

112. Yaghi, A. H., T. H., Hyde, A. A., Becker, J. A., Williams, and W., Sun, “Residual stress simulation in welded sections of P91 pipes”, *Journal of Materials Processing Technology*, Vol. 167, pp. 480-487, 2005.

113. Dean, D., and M., Hidekazu, “Prediction of welding residual stress in multi-pass butt-welded moldified 9Cr-1Mo steel pipe considering phase transformation effects”, *Computational Materials Science,* Vol. 37, pp. 209-219, 2006.

114. Deng, D., and H., Murakawa, “Numerical simulation of temperature field and residual stress in multi-pass welds in stainless steel pipe and comparison with experimental measurements”, *Computational Materials Science,* Vol.37, pp. 269-277, 2006.

115. Jiang, W., and K., Yahiaoui, “Finite element prediction of residual stress distributions in a multipass welded piping branch junction”, *Journal of Pressure Vessel Technology*, Vol. 129, pp. 601-608, 2007.

116. Mousavi, S. A. A. A., and R., Mirasmaeili, “Experimental and numerical analyses of residual stress distributions in TIG welding process for 304L stainless steel”, *Journal of Materials Processing Technology*, Vol. 208, pp. 383-394, 2008.

117. Lee, C., and K., Chang, “Three-dimensional finite element simulation of residual stress in circumferential welds of steel pipe including pipe diameter effects”, *Materials Science and Engineering*, Vol. 487, pp. 210-218, 2008.

118. Murugan, N., and R. Narayan, “Finite element simulation of residual stresses and their measurement by contour method”, *Materials and Design*, Vol. 30, pp. 2067-2071, 2009.

119. Karalis, D. G., V. J., Palazoğlu, and D. J., Pantelis, “Mechanical response of thin SMAW arc welded structures: experimental and numerical investigation”, Theoretical and Numerical Fracture Mechanics, Vol. 51, pp. 87-94, 2009.

120. Martinson, P., S., Daneshpour, M., Koçak, S., Riekerhr, and P., Staron, “Residual stress analysis of laser spot welding of steel sheets”, *Materials and Design*, Vol. 30, pp. 3351-3359, 2009.

121. Zhang, H. J., G. J., Zhang, C. B., Cai, H. M., Gao, and L., Wu, “Numerical simulation of three-dimension stress field in double-sided double arc multipass welding process”, *Materials Science and Engineering*, Vol. 499, pp. 309-314, 2009.

122. Yılbas, B. S., A. F. M., Arif, and B. J. A., Aleem, “Laser welding of low carbon steel and thermal stress analysis”, *Optics & Laser Technology*, Vol. 42, pp. 760-768, 2010.

123. Xu, S., “The numerical analysis of heterogenic welding joint residual stress”, *Procedia Engineering*, Vol. 15, pp. 3870-3874, 2011.

124. Kovacevic, R., F., Kong, and J., Ma, “Numerical and experimental study of thermal induced stress in the hybrid lase-GMA welding process”, Journal of Materials Processing Technology, Vol. 211, pp. 1102-1111, 2011.

125. Hossain, S., C. E., Truman, and D. J., Smith, “Finite element validation of the deep hole drilling method ofr measuring residual stresses”, *International Journal of Pressure Vessels and Piping*, Vol. 93-94, pp. 29-41, 2012.

126. Jiang, J., and M., Zhao, “Influence of residual stress on stress concentration factor for high strength steel welding joints”, *Journal of Constructional Steel Research*, Vol. 72, pp. 20-28, 2012.

127. Aloraier, A. S., and S., Joshi, “Residual stress in flux cored arc welding process in bead on plate specimens”, Materials Science and Engineering A, Vol. 534, pp. 13-21, 2012.

128. Zhao, H., G., Zhang, Z., Yin, and L., Wu, “Three dimensional finite element analysis of thermal stress in single-pass multi-layer weld-based rapid prototyping”, *Journal of Material Processing Technology*, Vol. 212, pp. 276-285, 2012.

129. Haigh, R. D., M. T., Hutchings, J. A., James, S., Ganguly, R., Mizuno, K., Ogawa, S., Okido, A.M. Paradowska, and M. E. Fitzpatrick, “Neutron diffraction residual stress measurements on girth-welded 304 stainless steel pipes with weld metal deposited up to half and full pipe wall thickness”, *Journal of Pressure Vessel Technology*, Vol. 101, pp. 1-11, 2013.

130. Xu, S., and W., Wang, “Numerical investigation on weld residual stresses in tube on tube sheet joint of a heat exchanger”, *International Journal of Pressure Vessels and Piping*, Vol. 101, pp. 37-44, 2013.

131. Smith, M. C., P. J. Bouchard, M., Turski, L., Edvards, and R. J., Dennis, “Accurate prediction of residual stress in stainless steel welds”, *Computational Materials Science,* Vol. 54, pp. 312-328, 2013.

132. J.J. Xu, P., Gilles, Y. G., Duan, and C., Yu, “Temperature and residual stress simulations of the NeT single-bead-on-plate specimen using SYSWELD”, *International Journal of Pressure Vessels and Piping,* Vol. 99-100, pp. 51-60, 2012.

133. Ohms, C., R. C., Wimpory, D. E., Katsareas, and A. G., Youtsos, “NET TG1: Residual stress assessment by neutron diffraction and finite element modeling on a single bead weld on a steel plate”, *International Journal of Pressure Vessels and Piping,* Vol. 86, pp. 63-72, 2009.

134. Price, J. W. H., A., Paradowska, S., Joshi, and T., Finlayson, “Residual stresses measurement by neutron diffraction and theoretical estimation in a single weld bead”, *International Journal of Pressure Vessels and Piping,* Vol. 85, pp. 381-387, 2006.

135. Malik, A. M., E. M. Qureshi, N. U., Dar, and I. Khan, “Analysis of circumferentially arc welded thin walled cylinders to investigate the residual stress fields”, *Thin-Walled Structures,* Vol. 46, pp. 1391-1401, 2008.

136. Deng, D., and H., Murakawa, “Prediction of welding distortion and residual stress in a thin plate butt-welded joint”, *Computational Materials Science,* Vol. 43, pp. 353-365, 2008.

137. Deng, D., “FEM prediction of welding residual stress and distortion in carbon steel considering phase transformation effects”, *Materials and Design,* Vol. 30, pp. 359-366, 2009.

138. Nart, E, and Y., Celik, “A practical approach for simulating submerged arc welding process using FE method”, *Journal of Constructional Steel Research,* Vol. 84, pp. 62-71, 2013.

139. M.R. Forouzan, S. M. M., Nasiri, A., Mokhtari, A., Heidari, and S. J., Golestaneh, “Residual stress prediction in submerged arc welded spiral pipes”, *Materials and Design*, Vol. 33, pp. 384-394, 2012.

140. Muránsky, O., C. J., Hamelin, M. C., Smith, P. J., Bendeich, and L., Edwards, “The effect of plasticity theory on predicted residual stress fields in numerical weld analyses”, *Computational Materials Science,* Vol. 54, pp. 125-134, 2012.

141. Murata, Y., M., Morinaga, R., Hashizume, K., Takami, T., Azuma, Y., Tanaka, and T., Ishiguro, “Effect of carbon content on the mechanical properties of 10Cr-5W ferritic steels”, *Materials Science and Engineering*, Vol. A282, pp. 251-261, 2000.

142. Lui, L., Q., Li, X., Liu, Y., Gao, X., Ren, B., Liao, and Q., Yang, “Stress field simulation of carburized specimens with different carbon content during quenching process”, *Materials Letters*, Vol. 61, pp. 1251-1255, 200.

143. Guo, J., S., Yang, C., Shang, Y., Wang, and X., He, “Influence of carbon content and microstructure on corrosion behaviour of low alloy steels in a Cl^- containing environment”, Corrosion Science, Vol. 51, pp. 242-251, 2008.

144. Lui, L., Q., Li, X., Liu, Y., Gao, X., Ren, B., Liao, and Q., Yang, “Stress field simulation of carburized specimens with different carbon content during quenching process”, Materials Letters, Vol. 61, pp. 1251-1255, 2007.

145. Chi, Z., X., Zhi-xin, Y., Zhi-gang, and L., Zhi-hao, “Influence of prior austenite deformation and non-metallic inclusions on ferrite formation in low-carbon steels”, Journal of Iron and Steel Research, Vol. 17, pp. 36-42, 2010.

146. Qun, L., W., Tian-sheng, L., Hong-biao, G., Yu-wei, L., Ning, and J., Tian-fu, “Warm deformation behaviour of steels containing carbon of 0.45% to 1.26% with martensite startling structure”, Journal of Iron and Steel Research, Vol. 17, pp. 34-37, 2010.

147. Zhang, X., S., Wang, Y., Zhang, C., Esling, X., Zhao, and L., Zuo, “Carbon-content dependent effect of magnetic field on austenitic decomposition of steels”, Journal of Magnetism and Magnetic Materials, Vol. 324, pp. 1385-1390, 2012.

148. Narayan, S., and A., Rajeshkannan, “Influence of carbon content on strain hardening behaviour of sintered plain carbon steel preforms”, Journal of Iron and Steel Research, Vol. 18, pp. 33-40, 2011.

149. Serajzadeh, S., and A. K., Taheri, “An investigation into the effect of carbon on the kinetics of dynamic restoration and flow behaviour of carbon steels”, Mechanics of Materials, Vol. 35, pp. 653-660, 2003.

150. Itabashi, M., and K., Kawata, “Carbon content effect on high-strain-rate tensile properties for carbon steels”, International Journal of Impact Engineering, Vol. 24, pp. 117-131, 2000.

151. Jia, G., S., Cheng-jia, Y., Shan-wu, W., Ying, W., Lian-wei, and H., Xin-lai, “Effect of carbon content on mechanical properties and weather resistance of high performance bridge steels”, Journal of Iron and Steel Research, Vol. 16, pp. 63-69, 2009.

152. ASM, *ASM Handbook Volume 4 Heat Treating*, ASM International, 1991.

153. G. Krauss, *Steels: Heat Treatment and Processing Principles*, ASM International, 1989

154. Chandler, H., *Hardness Testing*, ASM International, 1999.

155. Kuhn H., *ASM Handbook Volume 8 Mechanical Testing and Evaluation*, ASM International, 2000.

156. Herrmann, K., *Hardness Testing Principles and Applications*, ASM International, 2011.

157. Abrams, H., and G. N. Maniar, *Metallography: A Practical Tool for Correlating the Structure and Properties of Materials*, ASM International, 1974.

158. Voort, G. F. V., *ASM Handbook Volume 9 Metallography and Microstructures*, ASM International, 2004.

159. Petzow, G., *Metallographic Etching*, ASM International, 1999.

160. Voort, G. F. V., *Metallography Principles and Practice*, ASM International, 1999.

161. Crankovic, G. M., *ASM Handbook Volume 10 Materials Characterization*, ASM International, 1986.

162. Reimer, L., *Scanning Electron Microscopy: Physics of Image Formation and Micronanalysis*, Springer London, 2010.
163. Collins, T.J., “ImageJ for microscopy”, *BioTechniques*, Vol. 43, pp. 25–30, 2007.

164. Eliceiri, K., and C., Rueden, “Tools for visualizing multidimensional images from living specimens”, *Photochem Photobiol*, Vol 81, pp. 1116-1138, 2005.

165. Barboriak, D., A., Padua, G., York, J., Macfall, “Creation of DICOM-Aware Applications Using ImageJ”, *Journal of Digit Imaging*, Vol. 18, pp. 91-100, 2005.

166. Rajwa B., H., McNally, P., Varadharajan, J., Sturgis, and J., Robinson, “AFM/CLSM data visualization and comparison using an open-source toolkit”. *Microstracture Res. Tech.*, Vol. 64, pp. 180-260, 2004.

167. Messler, R. W., *Principles of Welding*, John Wiley, Weinheim, 1999.

168. Callister, W. D., *Fundamentals of Materials Science and Engineering*, John Wiley, USA, 2005.

169. Kou, S., Welding Metallurgy, John Wiley, New Jersey, 2003.

170. Dupont, J. N., and A. R., Marder, “Thermal efficiency of arc welding processes”, *Welding Research Supplement*, Vol. 74, pp. 406-511, 1995.

171. Cetim, J. L., *Handbook of Measurement of Residual Stress*, The Fairmont Press, Lilburn, 1996.

172. Thurston, R. N., “Wave Propagation in Fluids and Normal Solids”, in W. P. Mason (edt), *Physical Acoustics*, pp. 2-109, Academic Press, 1964.

173. Hughes, D. S., and J. L., Kelly, “Second-order elastic deformation of solids”, Phys*ical Review*, Vol. 92, pp. 1145-1149, 1953.

174. Murnaghan, F. D., “Finite deformation of an elastic solid”, *American Journal of Mathematics*, Vol. 59, pp. 235-260, 1937.

175. Bray, D. E., and R. K. Stanley, *Nondestructive Evaluation*, CRC Press, 1996.

176. Hrennikoff A., “Solution of Problems of Elasticity by the Frame-Work Method”, *ASME Journal of Applied Mechanics,* Vol. 8, pp. 619-715, 1941.

177. Courant, R. L., “Variational Methods for the Solution of Problems of Equilibrium and Vibration”, *Bulletin of the American Mathematical Society*, Vol. 49, pp. 1-23, 1943.

178. Zienkiewicz, O. C. and Y. K. Cheung, *Finite Element Method in Structural & Continuum Mechanics*, McGraw Hill, 1967.

179. ANSYS, *Finite Element Analysis Software Help Document*, Release 13.

180. Moaveni S., *Theory and Application with Ansys*, Prentice Hall, New Jersey, 1999.

181. Shim, Y., Z., Feng, S., Lee, D., Kim, J., Jaeger, J. C., Papritan. and C. L., Tsai, “Determination of residual stresses in thick-section weldments”, *Welding Journal,* Vol. 71, pp. 305-312, 1992.

182. Mahin, K. W., S., Mac-Ewen, W., Winters, W., Mason, M., Kanouff, and E. A., Fuchs, “Evaluation of residual stress distributions in a traveling GTA weld using finite element and experimental techniques”, *Process Modelling of Casting and Welding Processes IV: The Minerals*, Metals & Materials Society, pp. 339, 1988.

183. Mahin, K. W., W., Winters, T. M., Holden, R. R., Hosbons, and S. R., MacEwen, “Prediction and measurements of residual elastic strain distributions in gas tungsten arc welds”, *Welding Journal*, Vol. 70, pp. 245-260, 1991.

184. Friedman, E., “Thermomechanical analysis of the welding process using the finite element method”, *ASME J. Pressure Vessel Technology,* Vol. 97, pp. 206-213, 1975.

185. Tekriwal, P., and J., Mazumder, “Thermo-mechanical analysis of residual strains and stress in a GMA weld”, *Proceedings of the 2nd Int. Conf. on Trends in Welding Research,* pp. 91, 1989.

186. Bae, K. Y., S. J., Na and D. H., Park, “A study of mechanical stress relief (MSR) treatment of residual stresses for one-pass submerged arc welding of V-grooved mild steel plate”, *Journal of Engineering Manufacture*, Vol. 208, pp. 217, 1994.

187. Y., Chenand, and I. C., Sheng, “Residual stress in weldment”, *Journal of Thermal Stresses,* Vol. 15, pp. 53-69, 1992.

188. Goldak, J., A., Chakravarti, and M., Bibby, “A new enite element model for welding heat sources”, *Metallurgical Trans B,* Vol. 15B, pp. 299-305, 1984.

189. Pavelic, V., R., Tanbakuchi, O. A., Uyehara, and P. S., Myers, “Welding of Thin Plates”, *Welding Journal Research Supplement*, Vol. 48, pp. 295-305, 1969.

190. The MPDB software, "Temperature Dependent Elastic & Thermal Properties Database", http://www.jahm.com/, [retrieved 10 May 2013]

191. Muránsky, O., C. J., Hamelin, M. C., Smith, P. J., Bendeich, and L., Edwards, “The effect of plasticity theory on predicted residual stress fields in numerical weld analyses”, *Computational Materials Science,* Vol. 54, pp. 125-134, 2012.

APPENDIX A: TEMPERATURE DEPENDENT THERMAL AND STUCTURAL PROPERTIES

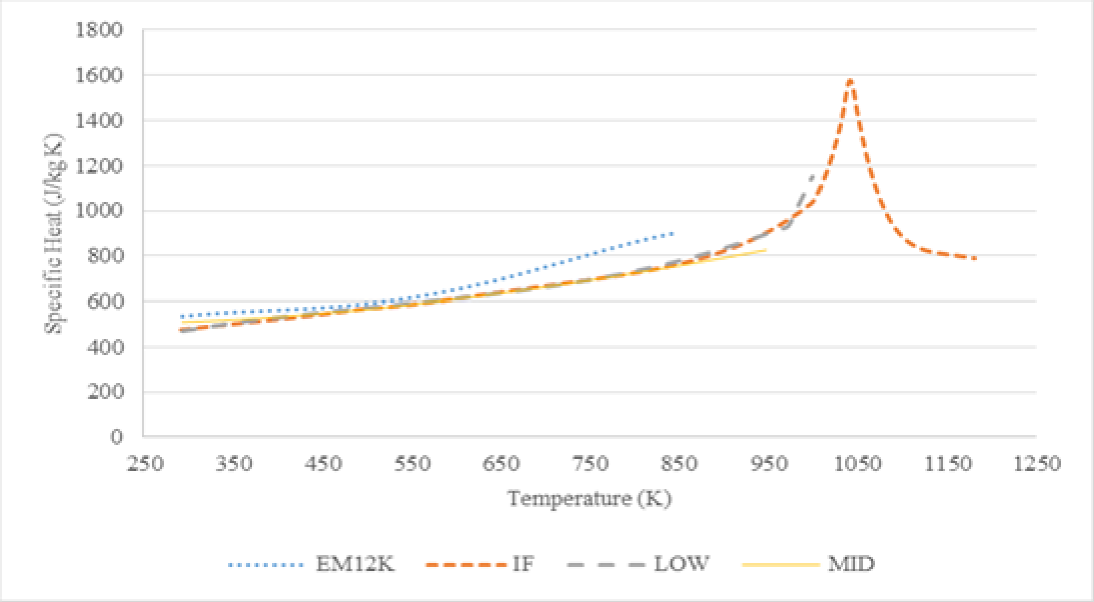

Figure A.1. Temperature dependent specific heat values of weld wire and samples

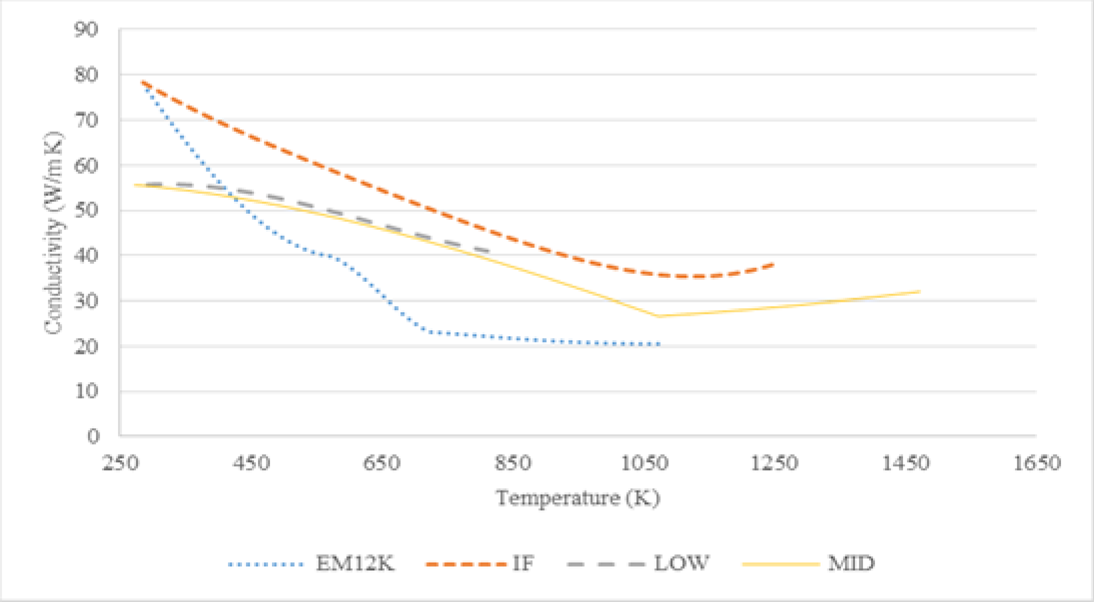

Figure A.2. Temperature dependent thermal conductivity values of weld wire and samples

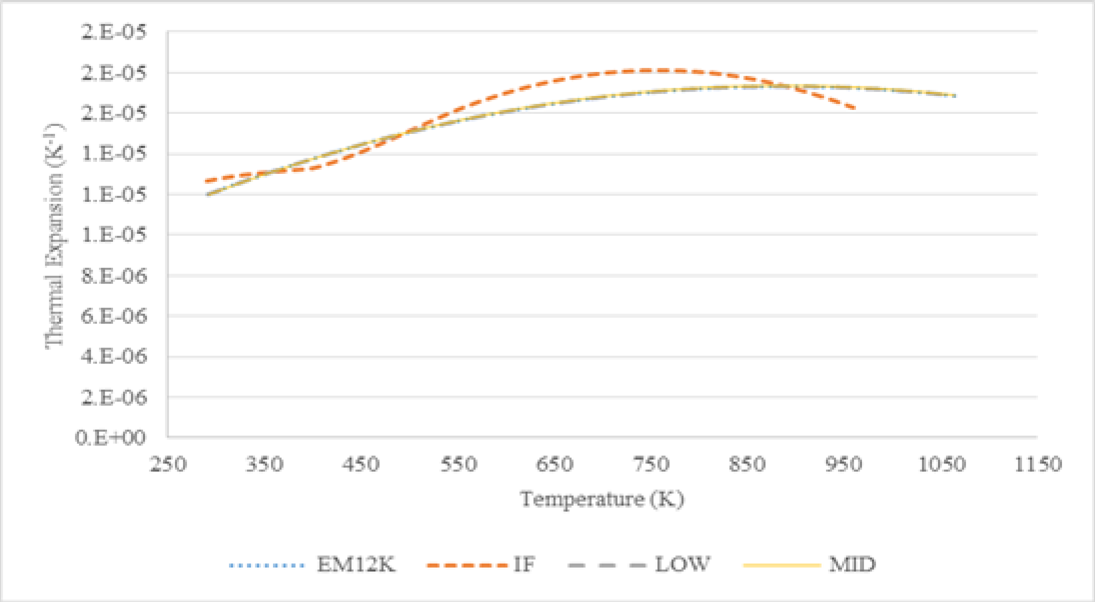

Figure A.3. Temperature dependent thermal expansion values of weld wire and samples

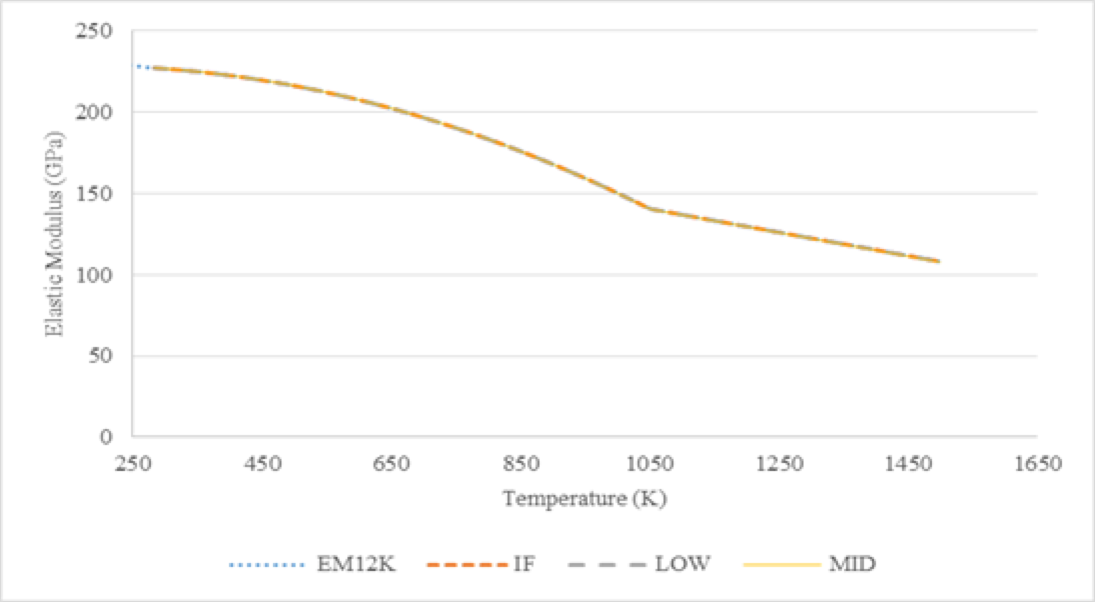

Figure A.4. Temperature dependent elastic modulus values of weld wire and samples

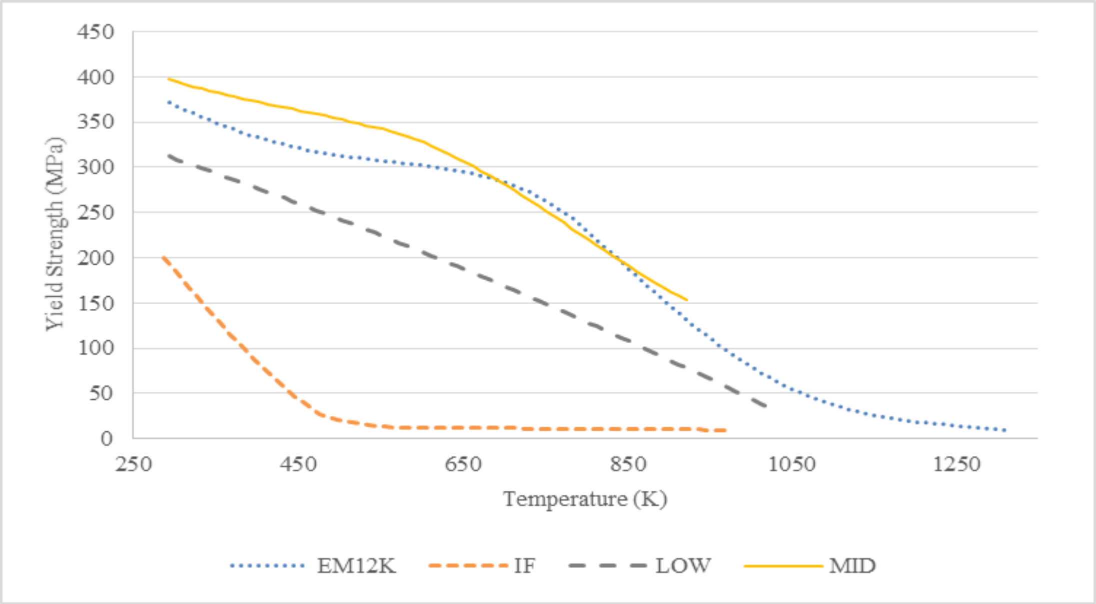

Figure A.5. Temperature dependent yield strength values of weld wire and samples

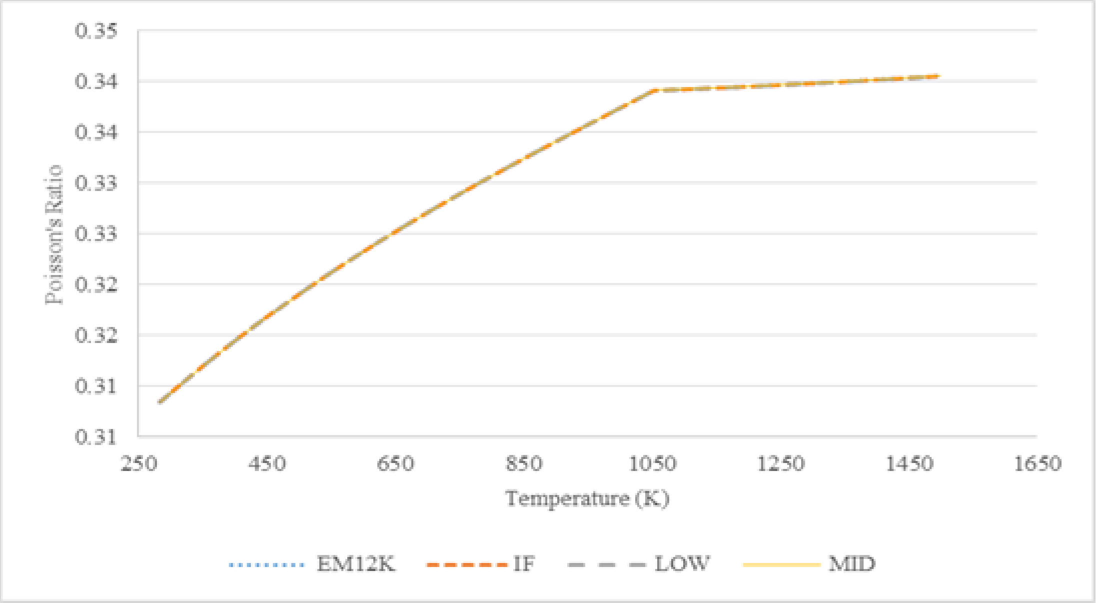

Figure A.6. Temperature dependent poisson’s ratio values of weld wire and samples